INTEGRATED MICRO DEVICES FOR SMALL SCALE GASEOUS FLOW STUDY

Thesis by

Jianqiang Liu, M.S. EE

Dissertation

In Partial Fulfillment of the Requirements

for the Degree of

Doctor of Philosophy

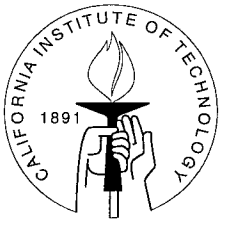

California Institute of Technology

Pasadena, California

1995

Submitted December, 1994

INTEGRATED MICRO DEVICES FOR SMALL SCALE GASEOUS FLOW STUDY

Approved by
Dissertation Committee:

_____

_____

_____

_____

_____

To my wife, and family

Acknowledgements

In 1990, I made one of the most important decision in my life: I switched my major from astronomy to electrical engineering. To make such a move successful is very difficult usually. Fortunately, I chosed Dr. Yu-Chong Tai as my advisor. Over the four years, I never suspect my choice: Dr. Tai is one of the best advisor I have ever met. Without his advise and support, my study and research can never be successful. I also get tremendous help and advise from Prof. Chih-Ming Ho at UCLA. The financial support for my research project is provided by Air Force Office of Scientific Research.

My research involves a full spectrum of work for example, device fabrication, measurements and theoretical modeling. It is very difficult usually for one to carry out such a task. With help from Trevor Roper, I learn a lot about semiconductor equipments. My partner Xing Yang, Kin-Choek Pong at UCLA also gives me tremendous help on experiments. I also want to acknowledge following people: Dr. Denny Miu, Fukang Jiang, Janice Tucker, Charles Grosjean, Thoma Rocco Tsao, Wen Hsuan Hsieh, C. S. Chang, D. J. Cheng, Rannan Miller, Chang Liu, Ren Wu, Shuyun Wu, John Wright, Frank Perez, Svetlana Tatic-Lucic, Viki Vickenbacker Temesvary, Tseng Yang Hsu, Nancy Winfree, Adrian Ionescu for their generous help whenever I need.

Abstract

Integrated Micro Devices for Small Scale Gaseous Flow Study

Jianqiang Liu

Doctor of Philosophy in Electrical Engineering

California Institute of Technology

Microfluidics has been an active research field for several years. Numerous micro devices such as pumps, valves, flow sensors and integrated systems for chemical analysis and medical applications have been developed. However, experimental studies of fluid flow in those micro devices are rare to find. As a result, design and analysis of microfluidic devices are mostly based upon continuous flow theory which is subjected to serious suspection as dimensions of the device become smaller and smaller. Several experimental studies have actually shown their results can not be explained with continuous flow model.

So far, almost all the experimental studies of microflow are limited to the two-point pressure (inlet and outlet) and flow rate measurements using either conventional capillaries or micromachined channels. In order to measure the microflow with more details, several integrated microflow systems are presented in the thesis. These systems include microchannels (with either uniform or non-uniform cross-sections) and pressure sensors (which are distributed along the channels). Using the integrated microflow systems, some preliminary gas flow experiments have been conducted. For the first time, the gaseous pressure distribution inside microchannels are measured experimentally. The pressure distribution inside a microchannel with uniform cross-sectional area is found to be nonlinear. The experimental results can be explained with an isothermal viscous flow model with slip-flow boundary conditions. Furthermore, it is found that a channel with non-uniform cross-sections can

cause a non-trivial pressure change.

During the developments of the integrated microflow systems, several related problems has been studied and solved, for example, a universal model has been found which can be used to simulate PSG or oxide sacrificial layer etching process in HF based solutions, a surface micromachined pressure sensor has been designed and modeled. Many technical difficulties such as, thin film stress, etching and sealing of the microchannels and chambers, process integration for microchannels and pressure sensors, etc., have been overcome. All the details related to the design and fabrication have been discussed in the thesis.

Contents

List of Tables

List of Figures

Chapter 1

Introduction of Microflow

1.1 Introduction

Studying and developing of the microfluidic devices were originated about twenty years ago[1, 2, 3, 4, 5, 6]. These early efforts toward making miniature fluid devices have only modest follow up. Within the last couple of years, however, there is a dramatic increase in research activities in the microfluidics field. The developments are mainly propelled by the advancement of the microfabrication technology- micromachining. Numerous microfluidic devices ranging from simple single element devices such as flow sensors and valves to complex micro fluid handling systems for chemical analyses, consisting of pumps, valves, flow sensors, separation capillaries, chemical detectors, etc., have been developed. Now, microfluidics is developing into a 'hot' research field[7].

Design and fabrication of microfluidic devices involve combining the micromachining technology with fluid mechanics to make miniature devices for a very wide range of applications. People from areas such as fluid mechanics, electrical engineering, chemistry and medication, etc., are attracted into this multidisciplinary research field. To people with engineering background, microfluidics represents one of the major application of microfabrication technology. To people with fluid mechanics background, microfluidics represents a new direction for studying fluid mechanics and gas dynamics.

Study of fluid flow in small channels can be traced back to the beginning of the this

century[8]. However, almost all of research activities, since then, are focused on rarefied gas flow on macroscopic scale such as high altitude flight and vacuum process[9]. Only in the past several years, when microfluidics became an important research subject due the advancement of micromachining technology, enough interests of studying microflow have been risen as it provides the most important knowledge for understanding and designing microfluidic devices. Since the fundamental theories have long existed, the most needed for studying microflow is experimental measurements of physical parameters such as, pressure, temperature, velocity and flow rate, etc. However, so far, most microfluidic devices are developed with product orientated for example, flow sensors, micro valves, micro pumps. etc. There is a sever lack of micro devices designed specifically for studying fluid flow on microscopic scale.

Some initial efforts have been made in the past several years. These initial experimental studies are mostly carried out with very simple microfluidic devices, namely microchannels[10, 11, 12]. Some interesting phenomenons related with microflow have been found. Recently, some more complicated microsystem with integrated microchannels and sensors for microflow experiments have also been designed and fabricated[13]. It is expected that, with the advancement of micromachining technology, more in-depth microflow study with various microflow systems will come out in the next several years.

Microflow research involves studying fluid flow related phenomena in devices with characteristic dimension, L, ranging from submicrons to several hundreds micrometers. Over this broad range of the dimension, characteristics of the fluid flow can change dramatically. Hence, it is convenient to divide the flow into several characteristic flow regimes such that theoretical models can be developed for each flow regime. As an example, based upon Knudsen number, K_n, the fluid flow can be divided into continuous flow ($K_n \ll 1$), slip flow ($K_n \sim 1$) and free-molecule flow ($K_n \gg 1$). Although the theoretical models for flows at different flow regimes are different, they all can be deducted from the kinetic theory, i.e, Boltzmann equation[14, 15]. Because of the small size of the object, microflow, even at atmosphere pressure, can span from free-molecule flow regime to continuous flow regime. This nature of the microflow makes it a very intriguing and exciting research topic which is rarely explored.

Another research field which is more general and very closely related to the microflow is called the rarefied gas flow. However, since the studies of the rarefied gas flow are mostly motivated by the interests such as high altitudes and high speed flight, vacuum process, etc., the dimensions of the objects are usually still in macroscopic scale. Some specific phenomenons related with the microscopic scale flow might be ignored during the study. These microscopic scale related phenomenons can be very important to the function of the microfluidic devices. Therefore, it is absolutely necessary to study the microflow on a microscopic scale, both experimentally and theoretically.

It is expected that the microflow will become a very active research field for the future. Realizing the importance of the microflow study, in this thesis I will present an integrated microflow measurement system designed for pressure distribution measurement in a microchannel. This work represents another critical step in advancing the experimental study of microflow since the two-point pressure and flow rate measurements with bulk micromachined channels. In this chapter a brief review of some basic microflow related fluid concepts and theories will be given followed by a brief review of microflow study and applications.

1.2 Several Basic Concepts

1.2.1 Mean Free Path

The concept of *m*ean free path is fundamentally important in understanding the role of Kundsen number and division of flow regimes. The mean free path is defined as the average distance that a molecule travels between successive collisions. If the molecule in a fluid is modeled as a rigid-sphere with radius, d, the mean free path of the molecule, λ, can be calculated with the following expression,

$$\lambda = \frac{1}{\sqrt{2}\pi d^2 n} \tag{1.1}$$

where n is the number density (number of the molecules per unit volume) of the gas. This is called rigid-sphere model. As noticed from Eq. (1.1), the mean free path is independent of the temperature, T, and depend only on the density and the radius of the molecules.

1.2.2 The Reynolds Number

A dimensionless combination of several important quantities gives the Reynold number[16]

$$R_e = \frac{\rho u L}{\nu} \tag{1.2}$$

where u is the velocity, ν is the viscosity of the fluid, and L is some characteristic length of the flow field. One expects that the flow pattern will be the same when R_e is the same. For example, $R_e = 10^{-1}$ corresponds in air to a diameter of 10 μm with a speed of 0.15 m/sec or in glycerine to a diameter of 0.3 m with a speed of 50 m/sec. As a characteristic number, Reynold number has important meaning in continuous flow regime; for example, if Reynold number is above 2300, fluid flow will in general be turbulent, otherwise, the flow is laminar. If Reynold is less than one, the viscous force will dominate the flow; otherwise, inertial force will dominate the flow.

1.2.3 The Knudsen Number

The Knudsen number is another dimensionless quantity which is defined as

$$K_n = \frac{\lambda}{L} \tag{1.3}$$

where L is the significant dimension of the flow field. For some considerations, for example, L may be a characteristic dimension of the body itself in a flow field or the diameter of an internal flow conduit. For other considerations, L may be the boundary layer thickness, the diameter of a wind tunnel probe, or the thickness of the shock transition zone. In the case of surface micromachined channels, the L is the height of the microchannels.

The Knudsen number, K_n, is related to the more familiar parameters of fluid mechanics, the Mach number, M, and the Reynolds number, R_e, i.e,

$$K_n = 1.26\sqrt{\gamma}\frac{M}{R_e} \tag{1.4}$$

where γ is the isentropic exponent and K_n, R_e are both based on the same characteristic length L.

1.2.4 Flow Regimes

The division of gas dynamics into various regimes, based on characteristic ranges of values of an appropriate Knudsen number, has been proposed by Tsien, Roberts, Donaldson[17] and Samuel[9], among others. The various criteria which have been suggested are in some disagreement. One of the these[18], as an example, which is termed as 'continuum flow' for $K_n \leq 10^{-3}$, 'slip flow' for $10^{-3} < K_n < 0.1$, 'transition flow' for $0.1 < K_n < 10$ and 'free-molecule flow' for $K_n \geq 10$ is roughly based on what the density levels are, respectively, ordinary, slightly rarefied, moderately rarefied, and highly rarefied.

Microflow does not belong to any specific flow regime. It is based on the scale of the flow fields, i.e., channel flow with size ranging from submicron to hundreds microns, fluid flow in micro valves or pumps, etc. Depending upon the density of the fluid, microflow can be in any one of above flow regimes. For example, even at atmosphere, by no means rarefied, a flow in a submicron pipe or channel can be in transition flow regime, or even free-molecule flow regimes since the mean-free-path of the fluid is comparable with the size of the pipe (channel).

1.2.5 Fundamental Theory

Fluid in different flow regimes are modeled very differently. Theoretically, all models can be derived from 'kinetic theory' which is based on the Boltzmann equation,

$$\frac{\partial f}{\partial t} + \sum_{i=1}^{3} \left(v_i \frac{\partial f}{\partial x_i} + X_i \frac{\partial f}{\partial v_i} \right) = \Delta_c f \tag{1.5}$$

where gas distribution function, $f = f(x_i, v_i, t)$, is the number of molecules in a unit volume centered at the point (x_1, x_2, x_3) with velocity (v_1, v_2, v_3) at time t, or in other words, within the volume element of the phase space,

$$d\mathbf{x}d\mathbf{v} = dx_1 dx_2 dx_3 dv_1 dv_2 dv_3 \tag{1.6}$$

X_i is an external force field and $\Delta_c f$ is the time rate of change of f due to intermolecular collisions. The term $\Delta_c f$ is given by

$$\Delta_c f = \iiint d\mathbf{v}_1 \iint d\Omega \left[gI(g, \theta)(f' f_1' - f f_1) \right] \tag{1.7}$$

where $g = |\mathbf{v_i} - \mathbf{v}|$ is the relative velocity of the given molecule and a colliding molecule whose velocity is $\mathbf{v}_1$, the quantity $gI\,(g, \theta)\,d\Omega$ is the probability that the colliding molecule will be scattered into $d\Omega$ at θ, and f' and f_1' denote the distribution functions for molecules after collision, with velocities $\mathbf{v}_1'$ and $\mathbf{v}'$.

To solve the Boltzmann equation is very difficult. It involves an unknown collision function $\Delta_c f$. Traditionally, people have taken different approaches in order to solve fluid related problems: In continuum flow regime, macroscopic physical quantities such as velocity, pressure and temperature, etc., are used which represent mean values of a large number of molecules. A set of equations including mass conservation, momentum conservation (also called *Navier-Stokes* equation), and energy conservation equation, are derived from the Boltzmann equation. This approach, so called fluid mechanics, has achieved huge success in the past hundred years. In the slip flow regime, one convenient approach is to use the *Navier-Stokes* equation and disceret boundary conditions-slip boundary conditions. The other approaches include the thirteen moment equations and Burnett equations derived from the Boltzmann equation with some specific approximations or assumptions. In transition and free-molecule flow regimes, one has to solve the Boltzmann equation for each specific boundary conditions.

Discussion of these theoretical techniques for solving Boltzmann equation is out of the scope of this thesis. One thing worth mentioning so far is most of the work (both theoretical and experimental) is emphasized with applications in a specific flow regime; it is still unclear if any of the classical theory is accurate in describing flow in micron scales. As understandable, the microflow has some fundamentally different properties from flow on macro scale. One example is microflow has a much shorter time scale; for example, comparing two molecules at the same "temperature," one is in a microflow environment and the other is in a rarefied flow environment. The free-fly time between two consecutive collisions is very different for these two molecules. Thus, justification of using any one of the models for describing microflow is necessary. This and other fundamental problems related with microflow can only be answered by extensive experimental studies.

1.3 Microfluidics

1.3.1 Microflow Studies

For studying fluid flow on micron scale, the devices most popularly used are straight channels or pipes with uniform cross-sectional area. People have used the small channels for studying slip flow[8, 19], viscosity of fluids[20] and heat dissipation, etc.[2]. Most of the channels are glass capillary tubes. Recently, due to the development of micromachining technology, channels with size ranging from submicrons to hundreds micron can be easily made. Interests of studying microflow is revived since its wide applications in microfluidics. Fig. 1.1 shows a typical bulk micromachined channel used for microflow study by J. Pfahler et. al.[10, 21].

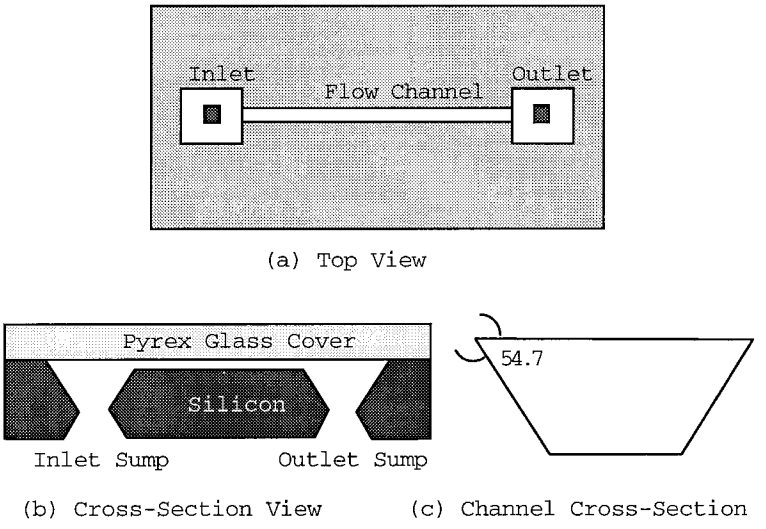

Figure 1.1: Schematics of the bulk micromachined channel for microflow studies.

Two major steps in its fabrication are first etching a groove on silicon substrate and inlet/outlet holes and second, bonding another substrate (either glass or silicon substrate) to cover the groove. Two advantages of the bulk-micromachined channels are simple fabrication and high pressure compatibility. However, since the fabrication involves bonding two substrates which requires high quality surface (clean and flat), integration of channels with other electrical devices are very difficult. So far, there are only very simple devices

other than channels which have been fabricated with bulk micromachining technology for microflow studies[22].

By attaching two pressure sensors at the inlet and outlet of the microchannel, Pfahler et. al. measured the flow rate and the pressure drops over the length of the channel with size ranging from 0.5 μm to 50 μm . From these results, he then calculated the Darcy friction factor, f, which is defined as

$$f = \frac{8\tau_w}{\rho U^2} = \frac{2D_h \Delta p}{\rho U^2 L} \tag{1.8}$$

where $D_h = 4\times$cross-sectional area/wetted perimeter is the hydraulic diameter, U is the averaged fluid velocity in the channel, L is the channel length, τ_w is the average shear stress on the wall, and Δp is the pressure drop across the channel. It is found that the friction or the apparent viscosity is consistently smaller than that predicted by conventional, incompressible theory. And more interestingly, the apparent viscosity decreases with decreasing channel depth.

Another study of fluid flow and heat transfer in microchannels was conducted by S. B. Choi et al.[11]. His microchannels with sizes ranging from 3 μm to 81 μm are made of silica glass. Four thermalcouples are attached to the microchannel to measure the temperature distribution. By applying a very high pressure at the inlet of the channel ($>$ 1000 psig), he achieved a much higher Reynold number flow ($R_e > 10^4$) than Pfahler does ($10^{-2} \sim 10^2$). Again it is found that the results deviate significantly from what it should be for conventional-sized tubes; the measured friction factors in laminar flow are less then those predicted from the macro tube, and the friction factors in turbulent flow are also smaller than those predicted by conventional correlations.

Recently, Arkilic et al.[12] report that the failure of using *Navier-Stokes* equation to model flows in microchannel is because of a non-continuum effect, namely a non-zero slip velocity at the fluid and solid interface. He repeated the pressure drop-flow rate measurement with a more delicate setup. The microchannel he used is also fabricated with the bulk micromachining technology which is similar to the one shown in Fig. 1.1. The experimental results can be accurately modeled by *Navier-Stokes* equation solved with slip-flow boundary

conditions. Arkilic's solutions of the Navier-Stokes are

$$P(x) = -K_c + \left[K_c^2 + (P_i^2 + 2K_cP_i)(1-x) + (1+2K_c)x\right]^{1/2} \tag{1.9}$$

and

$$\dot{m} = \frac{H^3 w P_0^2}{24\mu LRT}\left[P_i^2 - 1 + 2K_c(P_i - 1)\right] \tag{1.10}$$

where $K_c = 6(2-F)K_{no}/F$, K_{no} is the Knudsen number at the outlet of the microchannel, F is the specular reflection coefficient which depends upon the surface finish of the microchannel wall, P_i is the inlet to outlet pressure ratio, $P(x)$ is the normalized pressure distribution along the microchannel $(p(x)/p_{outlet})$ – assumed to be solely a function of x (the flow direction), and $\dot{m}$ is the mass flow rate of the channel. Using this model, he predicted that the pressure gradient for a given inlet and outlet pressure at the channel inlet is actually larger for the slip-flow than the no-slip continuum flow. However, toward the channel exit, the no-slip flow has larger pressure gradient. In general, the pressure inside a microchannel for a slip-flow boundary condition is lower than that for a non-slip flow boundary condition.

Following these experimental studies, Beskok et al. uses numerical simulation methods based on spectral element technique to study the momentum and heat transfer in complex micro geometries including microchannels[18]. The model he used is based on the *Navier-Stokes* equation and energy conservation equation with slip boundary conditions. The model can be stated as

$$\frac{D\mathbf{v}}{Dt} = -\frac{\nabla p}{\rho} + R_e^{-1}\nabla^2\mathbf{v} \tag{1.11}$$

$$\frac{DT}{Dt} = P_r^{-1}R_e^{-1}\nabla^2 T + E_cR_e^{-1}\frac{1}{2}\left(\frac{\partial u_i}{\partial x_j} + \frac{\partial u_j}{\partial x_i}\right)^2 \tag{1.12}$$

and

$$\nabla \cdot \mathbf{v} = 0 \tag{1.13}$$

where $\mathbf{v}$ is the velocity field $\mathbf{v}(\mathbf{x}, t)$, $T(\mathbf{x}, t)$ is the temperature, and ρ is the density, P_r and E_c are Prandtl and Eckert numbers, respectively; D denotes total derivative. The slip-velocity and temperature jump boundary conditions for mono-atomic gas near an isothermal surface in a nondimensional form are

$$u_{gas} - u_{wall} = \frac{2-\sigma_\nu}{\sigma_\nu}K_n\frac{\partial u_s}{\partial n} \tag{1.14}$$

$$T_{gas} - T_{wall} = \frac{2 - \sigma_T}{\sigma_T} \left(\frac{2\gamma}{\gamma + 1} \right) \frac{K_n}{P_r} \frac{\partial T}{\partial n} \tag{1.15}$$

Beskok's model includes high order Knudsen number effects as well as the coupling of momentum and heat transfer through thermal creep and viscous heating effects. One important conclusion from his simulation is the compressibility effects can dominate the flow, thus the influence of rarefied gases on the flow is only a secondary effect. The compressibility effects in a microchannel has also been studied by Harley[21].

The mentioned research activities represents some of the most important ones. These studies are all backed up by the two-point pressure drop with flow rate measurements. However, these experiments are far from enough to justify which model developed before is more close to the truth. To advance the microflow research, experiments which can give more detail about gas or liquid flow on micron-scale are absolutely necessary.

1.3.2 Microflow Applications

So far, one of the most exciting application of the microfabrication technology is microfluidic devices[7]. For example, valves, pumps, fluid dispensers, flow sensors, heat exchangers, microfluidic system for chemical analysis and other purposes have been developed using a broad range of micromachining technology. Performance of these devices are improving.

Valves

As basic elements in a fluid control system, valves have received considerable interest in the application of micromachining technology to fluid related microsystems. Different actuating principles have been applied to the micro-valves, for example, thermo-pneumatic[23], electrostatic[24], piezoelectric[25] and electromagnetic[26, 27], etc. The majority of micromechanical valves have been designed for gas flow control. Only a limited number are for liquid applications such as check valves integrated with pumps, or connected with a chemical analysis systems. The flow rate requirements in these applications can be satisfied by micromechanical valves, despite the reduced dimensions and flow conductance. Due to the nature of microfabrication technology (either bulk or surface micromachining), using a diaphragm as the moving part in a valve has become a favorite design[28, 29]. Valves with

cantilevers as moving parts are also realized[30, 31, 32].

One important trend in microvalve applications is in the microsystem domain, where valves are integrated with other elements. Examples of these applications are given below.

Pumps

Initial study of micropumps based on microvalves were started at Standford University in 1980[33]. Further development was carried out at the University of Twente by Van der Schoot et al.[34]. So far, a number of different membrane micropumps have been developed using different actuation principles. The highest yields achieved using a piezoelectrically actuated membrane micropump is 550 μl/min of water at 40 Hz pump frequency[35].

Flow Sensors

Flow sensors cover a wide range of devices and applications such as anemometers[36], shear-stress sensors[37], flow meters, etc. Most of the flow sensors are based on thermal detection principles. A comprehensive review has been given by van Oudheusden[38] for air and gas flow sensors. A brief review of flow sensors for liquid applications has been given by Gravesen[7].

Microfluidic System

An example of a microfluidic system is the integrated gas chromatography system developed at standford university by S. Terry, J. H. Jerman and J. B. Angell[39, 40] nearly twenty years ago. This system consists of a 1.5 m capillary column, a gas control valve, and a detector element all fabricated on a 2 in silicon wafer. Except for that, a Joule-Thomson minirefrigeration system is also demonstrated at Standford University by W. A. Little[41] Another typical microfluidic system is the constant flow rate dosing system. Such a system integrates a flow sensor with either a valve or a pump[23, 42, 43].

Other than that, a new type of microflow system designed specifically for studying gas flow on micron scale has been developed by the Caltech micromachining group[44]. This system includes a microchannel and a series of pressure sensors. Using this system, the pressure distribution inside a microchannel can be measured.

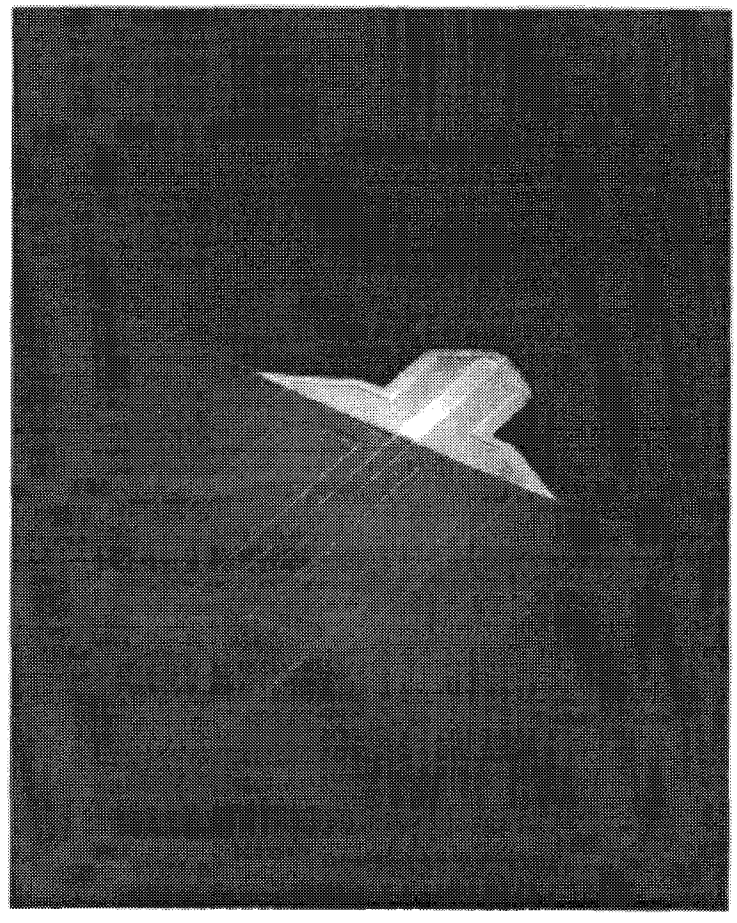

Figure 1.2: An anemometer developed at Caltech's micromachining lab for wind speed measurements. Courtesy of Fukang Jiang.

1.3.3 Conclusion

As one has seen, microfluidics is a multidisciplinary research area, for example, fluid mechanics, chemistry, medication, etc. It has attracted a tremendous amount of interest in the past several years because of both its wide applications and advancement of microfabrication technology which took place during the past twenty years. As a result of all these efforts, numerous microfluidic devices have been developed which include valves, pumps, flow sensors and microfluidic systems for medical and chemical applications.

In contrast to the great amount of effort spent on developing new devices, studies of the micro flow related phenomenons are really rare and still primitive. As in the most fundamental fluidic device-a flow channel (or pipe), experiments are limited to the two-point pressure and channel flow rate measurements. It has long be realized that the fluid flow on micron scales may be different, i.e., Navier-Stokes may not be an accurate model to describe the flow on micron scale. Some initial experimental results clearly suggest that some modifications to the Navier-Stokes equation are necessary. However, due to very limited amount of knowledge, to further advance the microflow study is very difficult. Therefore, it is believed that fundamental studies of microfluidics will play an important role in the future development of microfluidics.

Bibliography

[1] S. C. Terry, J. H. Jerman, and J. B. Angell, "A gas chromatographic air analyzer fabricated on a silicon wafer," *IEEE Trans. Electron. Devices*, pp. 1880–1886, 1979.

[2] D. B. Tuckermann and R. F. W. Pease, "High performance heat sinking for vlsi," *IEEE Electron Device, Lett.*, vol. ED-2, pp. 126–129, 1981.

[3] M. J. Zdeblick, P. W. Barth, and J. A. Angell, "Microminiature fluidic amplifier," in *Tech. Digest IEEE Solid-State Sensor and Actuator Workshop*, (Hilton Head Island, SC), 1986.

[4] E. Bassous, H. H. Taub, and L. Kuhn, "Ink jet printing nozzle arrays etched in silicon," *Appl. Phys. Lett.*, vol. 31, pp. 135–137, 1977.

[5] K. E. Petersen, "Fabrication of an integrated planar silicon ink-jet structure," *IEEE Trans. Electron Devices*, vol. ED-26, pp. 1918–1920, 1979.

[6] K. E. Petersen, "Silicon as a mechanical material," *Proc. IEEE*, vol. 70, pp. 420–457, 1983.

[7] P. Gravesen, J. Branebjerg, and O. S. Jensen, "Microfluidics-a review," in *Proceedings, MME'93*, 1993.

[8] M. Knudsen, "Die gesetze der molecular stromung und die inneren reibungstromung der gase durch rohren," *Annalen der Physik*, vol. 28, pp. 75–130, January 1909.

[9] S. A. Schaaf and P. L. Chambre, *Flow of Rarefied Gases.* New Jersey: Princeton University Press, 1961.

[10] J. Pfahler, J. Harley, and H. Bau, "Gas and liquid flow in small channels," in *Micromechanical Sensors, Actuators, and Systems*, vol. 32, pp. 49–60, ASME, 1991.

[11] S. B. Choi, R. F. Barron, and R. O. Warrington, "Fluid flow and heat transfer in microtubes," in *Micromechanical Sensors, Actuators, and Systems*, vol. 32, pp. 123–134, ASME, 1991.

[12] E. B. Arkilic, K. S. Breuer, and M. A. Schmidt, "Gaseous flow in microchannels," in *Application of Microfabrication to Fluid Mechanics 1994, International Mechanical Engineering Congress and Exposition* (P. R. Bandyopadhyay, K. S. Breuer, and C. J. Blechinger, eds.), vol. 197, (Chicago, Illinois), pp. 57–66, Academic Press, November 1994.

[13] J. Liu, Y.-C. Tai, J. Lee, K.-C. Pong, Y. Zohar, and C.-M. Ho, "In-situ monitoring and universal modelling of sacrificial psg etching using hydrofluoric acid," in *Proceedings of IEEE Micro Electro Mechanical Systems*, (Fort Lauderdale, Florida), pp. 71–76, IEEE, February 1993.

[14] E. H. Kennard, *Kinetic Theory of Gases.* McGraw-Hill, 1938.

[15] L. B. Loeb, *Kinetic Theory of Gases.* McGraw-Hill, 2nd ed., 1934.

[16] D. J. Tritton, *Physical Fluid Dynamics.* Molly Millars Lane, Wokingham, Berkshire, England: Van Nostrand Reinhold Company, 1977.

[17] C. d. P. Donaldson, "An approximate method for estimating the incompressible laminar boundary layer characteristics on a flat plate in slipping flow," *NACA Research Mem.*, vol. L9CO2, 1949.

[18] A. Beskok and G. E. Karniadakis, "Simulation of heat and momentum transfer in complex microgeometries," *J. of Thermophysics and Heat Transfer*, vol. 8, pp. 647–755, Oct.-Dec. 1994.

[19] A. Sreekanth, "Slip flow through long circular tubes," in ***Rarefied Gas Dynamics-Proceedings of the 6th International Symposium on rarefied Gas Dynamics*** (L. Trilling and H. T. Wachman, eds.), vol. 1, (New York), Academic Press, July 1968.

[20] J. Israelachvili, "Measurement of the viscosity of liquids in very thin films," *J. of Colloid and Interface Science*, vol. 110, pp. 263–271, march 1986.

[21] J. Harley and H. Bau, "Fluid flow in micron and submicron size channels," *IEEE Trans.*, vol. THO249-3, pp. 25–28, 1991.

[22] D. Sobek, A. M. Young, M. L. Gray, and S. D. Senturia, "A microfabricated flow chamber for optical measurements in fluids," in *Micro Electro Mechanical Systems*, (Fort Lauderdale, FL), pp. 219–224, February 1993.

[23] M. J. Zdeblick, *A planar process for an electric-to-fluidic valve.* PhD thesis, Standford University, 1988.

[24] J. Branebjerg and P. Gravesen, "A new electrostatic actuator providing improved stroke length and force," in *Proc. MEMS 92* (W. Bemecke and H. C. Petzold, eds.), (Travemunde, Germany), pp. 6–11, 1992.

[25] S. Shoji, van der Schoot B., N. F. de Rooji, and M. Esashi, "Smallest dead volume microvalves for integrated chemical analyzing systems," in *Tech. Digest IEEE Transducers' 91*, (San Francisco, CA), pp. 1052–1055, 1991.

[26] R. L. Schmidt, R. W. Bower, and S. D. Collins, "The design and fabrication of a magnetically actuated micromachined flow valve," *Sensors and Actuators, A*, vol. 24, pp. 47–53, 1990.

[27] S. Bouwstra, P. Kemna, and R. Legtenberg, "Thermally excited resonating membrane mass flow sensor," *Sensors and Actuators, A*, vol. 20, pp. 213–223, 1989.

[28] M. A. Huff, J. R. Gilbert, and M. A. Schmidt, "Flow characteristics of a pressure-balanced microvalve," in *Tech. Digest IEEE Transducers 93*, (Yokohama), pp. 98–101, 1993.

[29] J. H. Jerman, "Electrically-actived, normally-closed diaphragm valves," in *Tech. Digest IEEE Transducers' 91*, (San Francisco), pp. 1045–1048, 1991.

[30] J. Tiren, L. Tenerz, and B. Hok, "A batch-fabricated non-reverse valve with cantilever beam manufactured by micromachining of silicon," *Sensors and Actuators*, vol. 18, pp. 389–396, 1989.

[31] S. Park, W. H. Ko, and J. M. Prahl, "A constant flow-rate microvalve actuator based on silicon and micromachining technology," in *Tech. Digest IEEE Solid-State Sensor and Actuator Workshop*, (Hilton Head Island, SC), pp. 136–139, 1988.

[32] M. Shikida, K. Sato, and S. Tanaka, "Electrostatically-actuated gas valves with large conductance," in *Tech. Digest IEEE Transducers' 93*, (Fort Lauderdale, FL), pp. 102–105, 1993.

[33] J. G. Smits, "Piezoelectric micropumps with three valves working peristaltically," *Sensors and Actuators, A*, vol. 21-23, pp. 203–206, 1990.

[34] H. T. G. Van Lintel, F. C. M. van de Pol, and S. Bouwstra, "A piezoelectric micropump based on micromachining of silicon," *Sensors and Actuators*, vol. 15, pp. 153–167, 1987.

[35] V. Gass, B. H. van der Schoot, S. Jeanneret, and N. F. de Rooij, "Integrated flow-regulated silicon micropump," in *Tech. Digest IEEE Transducers' 93*, (Yokohama), pp. 1048–1051, 1993.

[36] F. Jiang, Y.-C. Tai, C. Ho, and W. Li, "A micromachined polysilicon hot-wire anemometer," in *Solid-State Sensor and Actuator Workshop, 1994*, (Hilton Head Island, SC), 1994.

[37] C. Liu, Y.-C. Tai, J.-B. Huang, and C.-M. Ho, "Surface micromachined thermal shear stress sensor," in *Application of Microfabrication to FLuid Mechanics 1994, International mechanical Engineering Congreee and Exposition* (P. R. Bandyopadhyay, K. S. Breuer, and C. J. Blechinger, eds.), vol. 197, (Chicago, Illinois), pp. 9–15, Academic Press, November 1994.

[38] B. W. van Oudheusen, "Silicon thermal flow sensors," *Sensors and Actuators, A*, vol. 30, pp. 5–26, 1992.

[39] S. C. Terry, *A gas chromatography system fabricated on a silicon wafer using integrated circuit technology.* PhD thesis, Standford University, 1975.

[40] S. C. Terry, J. H. Jerman, and J. B. Angell, "A gas chromatograph air analyzer fabricated on a silicon wafer," *IEEE Trans. Electron.*, vol. ED-26, p. 1880, 1979.

[41] W. A. Little, "Design and construction of microminiature cyrogenic refrigerators," in *AIP Proc. of Future Trends in Superconductive Electronics*, (University of Virginia, Charlottesville), 1978.

[42] M. Esashi, "Integrated micro flow control systems," *Sensors and Actuators*, vol. A21-A23, pp. 161–167, 1990.

[43] T. S. J. Lammerink, M. Elwenspoek, and J. H. J. Fluitman, "Integrated micro-liquid dosing system," in *Proc. MEMS 93*, (Fort Lauderdale, FL), pp. 245–259, 1993.

[44] J. Liu, Y.-C. Tai, K.-C. Pong, and C.-M. Ho, "Micromachined channel/pressure sensor systems for microflow studies," in *The 7th International Conference on Solid-State Sensors and Actuators, Transducers' 93*, (Yokohama, Japan), pp. 995–997, June 1993.

Chapter 2

Microchannels

2.1 Introduction

Channels or pipes are the most fundamental devices for applications related to fluid flow. Because of their popularity, extensive studies of fluid flow in the channels or pipes have been carried out in the past. Many models have been developed for almost any kind of flow conditions. In contrast, fluid flow in microchannels with sizes ranging from submicron to hundreds microns are rarely studied. This situation might be attributed to several reasons: first, there only very limited applications for very small channels; second, conduction of a microflow measurement is not easy because it is very difficult to interface the microchannel with other instruments for measurements. For example, glass capillaries can be made as small as several microns in diameter without difficulty. However, interfacing them with probes or sensors for studying fluid flow inside the capillaries is almost impossible. So far, fluid flow experiments with microchannels are limited with measurements only at the entrance and exit. The detailed information inside the microchannel is still missing. Now, with the advanced microfabrication technology, most difficulties can be overcome. Therefore, it is very natural for one to choose the microchannel first for studying microflow.

One way of making microchannels is to use bulk micromachining technology. There are two major steps in this technology. First, etch a groove on a silicon substrate; second, cover the groove by bonding a silicon or glass substrate to the wafer. Microchannels with

width varying from several micron to hundreds micron have been fabricated this way[1]. The advantages of this kind of microchannels include easy fabrication and high pressure compatibility. However, it is difficult to integrate microchannels with a large number of sensors using the bulk micromachining technology since the bonding requires a highly cleaned and flat surface.

An alternative is to use surface micromachining technology. With this technology, microchannels can be integrated with sensors such as temperature and pressure sensors. The fabrication involves several steps, for examples, sacrificial layer deposition, patterning, cover layer deposition, etching hole opening and sacrificial layer etching, etc. The key step is the sacrificial layer etching. This sacrificial layer etching technique has been widely used to make free standing microstructures such as beams, bridges, gears and motors, etc.[2]. Doped phosphorsilicate glass (PSG) is the most popular material used as the sacrificial layer since its etching rate in concentrated HF solutions (e.g. 49 wt.%) can be as high as microns per second and etching selectivities over other material such as, silicon and silicon nitride, are very high.

From the chemistry point of view, the PSG etching process is the dissolution of silicon dioxide (SiO_2) by acidic fluoride solutions. This is probably one of the most familiar chemical reactions. However, since high etch rate is preferred, the chemical concentration in the etching solution used in sacrificial layer etching is usually much higher than that used in the conventional IC fabrication process. The mechanisms of etching SiO_2 in concentrated HF solution is rarely studied, and no workable model can be found for simulating the sacrificial layer etching.

In this chapter, the design and fabrication of microchannels and chambers are presented. The chambers are used for the pressure sensors which are integrated with microchannels to form a complete microflow measurement system. Since the performance of a microsystem and, to some extent, the yield of the working device depends upon the design of the microchannels and chambers, a great number of experimental studies of the etching process are conducted with various 1-D and 2-D microstructures. A universal semi-empirical model has been developed based upon the experimental data. Such a model can be used to simulate the dynamic etching process in both 1-D and 2-D structures.

2.2 Microchannel Fabrication

2.2.1 Preparation of PSG Film

There are many methods for preparing phosphorsilicate glass (PSG) film. Each method is characterized by the chemicals involved, the deposition temperature and reactors. Physical properties of the PSG film can be different if one of the deposition conditions is different. The chemical reactions can be carried out either at atmospheric pressure in a continuous reactor or at reduced pressure in an LPCVD reactor. The PSG film used as the sacrificial layer in the microchannels and microflow systems is deposited using the following system:

$$SiH_4 + O_2 \longrightarrow SiO_2 + 2H_2 (< 500^\circ C) \tag{2.1}$$

$$4PH_3 + 5O_2 \longrightarrow 2P_2O_5 + 6H_2 \tag{2.2}$$

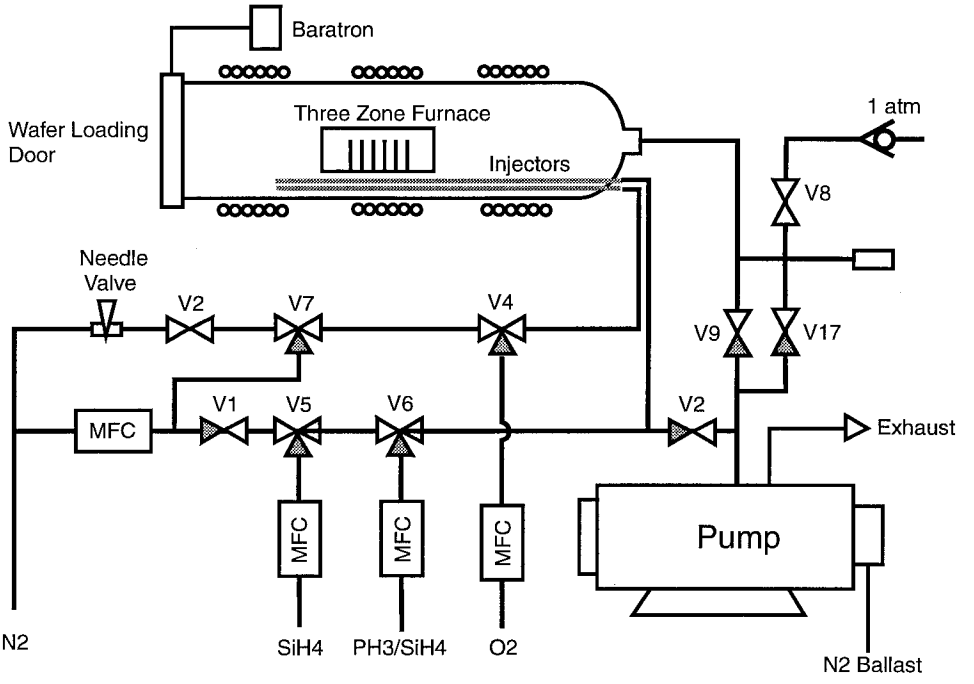

Figure 2.1: Schematic of the low pressure chemical vapor deposition system (LPCVD) for deposition of low temperature oxide (LTO) and phosphorus doped oxide.

Fig. 2.1 shows the schematic of the low pressure chemical vapor deposition system

(LPCVD) for low temperature silicon dioxide and phosphorus doped oxide (PSG). Co-oxidation of diluted PH_3 with SiH_4 plus excess O_2 at 300-500 °C leads to phosphorsilicate glasses, $(SiO_2)_{1-x}(P_2O_5)_x$, rather than a physical mixture of SiO_2 and P_2O_5. For IC fabrication, the major advantage of the system is the low deposition temperature allowing films to be deposited on top of the aluminum metallization. Consequently, the PSG film is widely used for passivation coatings over the final IC device and insulation between aluminum or other conduction layers. The main disadvantage is poor step coverage and particles caused by loosely adhering deposits on the reactor walls.

Here the PSG film is used as the sacrificial layer. Thus an important factor is to control its etching rate during the etching. Since the PSG etching rate strongly depends upon the phosphorus concentration[3], changing the PH_3 flow rate or the ratio of PH_3/SiH_4 in the system can change the phosphorus concentration in the film. To decide the phosphorus concentration in the PSG film, people usually use the experimentally determined curves of PSG etching rate in buffered HF solution vs. the phosphorus concentration[4, 5]. In the microchannel fabrication, it is preferred to have a very high etching rate. This purpose can be achieved by increasing the phosphorus concentration in the film. However, if the phosphorus concentration is too high, the film becomes very porous[6]. Therefore, a high temperature annealing step always follows the PSG deposition to improve the film quality.

2.2.2 Preparation of Low-stress Silicon Nitride Film

The LPCVD system used to deposit silicon nitride film is

$$3SiCl_2H_2 + 4NH_3 \longrightarrow Si_3N_4 + 6HCl + 6H_2 \tag{2.3}$$

Depositions are normally carried out in between 700 to 900 °C. The high temperature LPCVD nitride film has very good uniformity and step coverage[7]. The LPCVD nitride system used to deposit films for the microchannels and integrated microflow system is shown in Fig. 2.2.

For microflow system applications, the silicon nitride is used as the cover layer of microchannels and diaphragms of the pressure sensors. One of the most important properties is the intrinsic stress of the film. Silicon nitride usually has a high tensile stress.

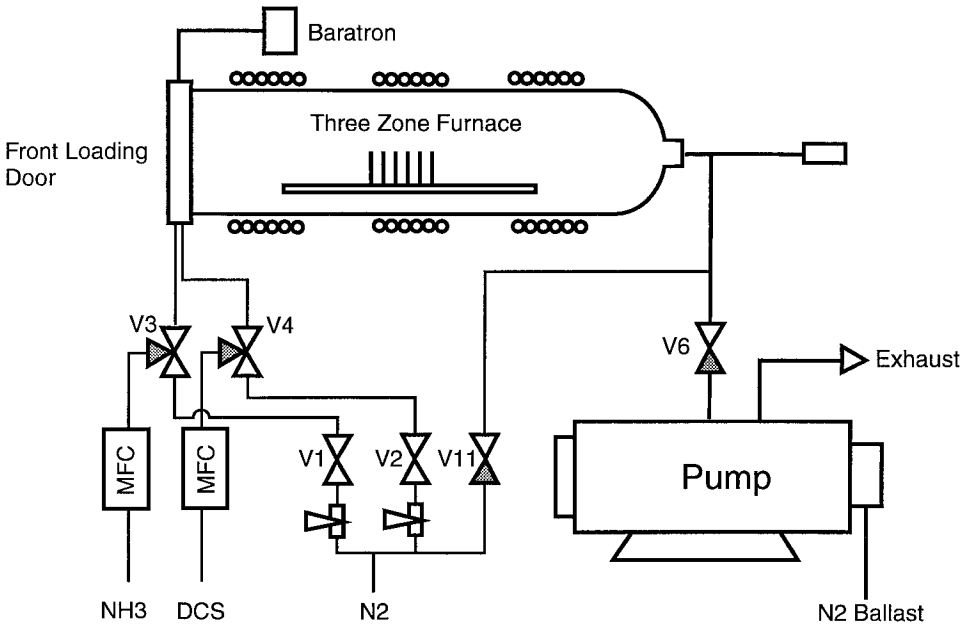

Figure 2.2: Schematic of low pressure chemical vapor deposition system for silicon nitride deposition.

The stress in stoichiometric silicon nitride (Si_3N_4) deposited at about 800 °C can be as strong as 10^{10} dyne/cm^2. Films thicker than 200 nm sometimes crack because of the high stress. For IC use, a stress compensation layer (for example, oxidation layer) is deposited first before depositing the silicon nitride to prevent the crack. However, to use the silicon nitride as a diaphragm material, the intrinsic stress has to be reduced. Sekimoto et al.[8] conducted some experiments to study the relationship between the intrinsic stress and the deposition conditions, specifically the ratio of $SiCl_2H_2/NH_3$. He found that by increasing the ratio, the stress can be significantly reduced, even changing sign (the stress becomes compressive). Due to the significant increase of $SiCl_2H_2$ flow rate, the deposited silicon nitride film contains more Si atoms than stoichiometric nitride. For example, the low stress silicon nitride used in the microflow chip fabrication has a composition of $Si_3N_{3.6}$ instead of Si_3N_4 for the stoichiometric silicon nitride.

Since the intrinsic stress in a diaphragm can significantly reduce the sensitivity of a pressure sensor (Ch. 3), it is preferred to make stress free silicon nitride film (by increasing

the ratio of $SiCl_2H_2/NH_3$). However, in practice, if there is not enough tensile stress in the film, a free standing diaphragm will most likely stick to the substrate after the sacrificial layer is removed[9, 10]. It is found that a little tensile stress can prevent the diaphragm from sticking to the bottom. Therefore, a number of experiments with various $SiCl_2H_2/NH_3$ ratio have been conducted and film stress are measured (the method is discussed in Ch. 4) in order to find adequate depositon conditions. The final recipe used for depositing silicon nitride for pressure sensor diaphragm can be seen in Appendix A.

2.2.3 Surface Microchannel Fabrication

There are many ways of making microchannels using surface micromachining technology. Two of them are to be discussed in following sections. The first type of microchannel (Fig. 2.3(a)) is built on the top of silicon substrate without etching substrate, so called surface microchannel. Because of its easy fabrication, it is used for studying the sacrificial layer etching problems. The sacrificial layer is made with a single PSG layer. The second type of microchannel (Fig. 2.3(b) is similar to the first one, but its surface is much smoother due to the use of local oxidation technique (LOCOS). The sacrificial layer is composed of a thin PSG film deposited above a wet oxidation layer. Since HF based solution etches PSG much faster than undoped oxide (whither grown or deposited oxide), the time taken to etch a microchannel with composite sacrificial layer is much less than a channel with only wet oxide as the sacrificial layer. Actually, undoped oxide alone is rarely used as the sacrificial layer especially when E_s (defined by Eq. 2.4) is large due to its slow etching rate. The fabrication of the second type of microchannels is more complicated than that of the first type of microchannels. However, since the surface topology can be made very smooth, the yield is improved and final devices are stronger. This type of microchannels are used exclusively in the design of microflow measurement systems.

The schematic fabrication steps for the first type of microchannel are listed in Table 2.1 (the description of the fabrications with recipes are presented in Appendix A.1). Since the height of the microchannel is defined by the thickness of the annealed PSG film, one can easily change the vertical dimensions of the microchannel by increasing or decreasing the PSG deposition time without modifying any other steps in the fabrication. As one

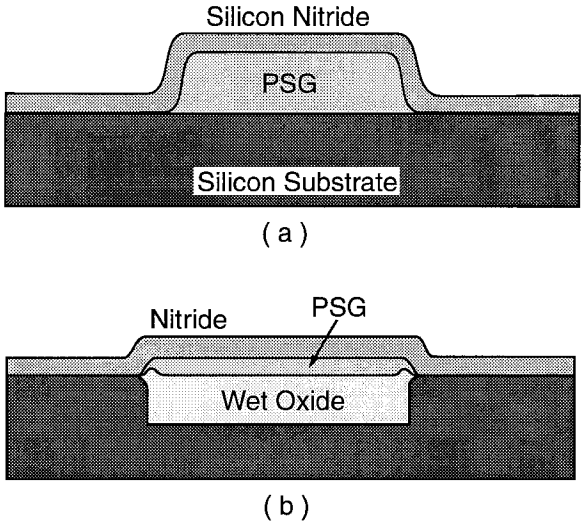

Figure 2.3: (a)a surface microchannel is fabricated on top of the silicon substrate. (b)a recessed surface microchannel has smoother surface topology.

Table 2.1: Flowchart for Fabrication of the Microchannels (I)

1	deposit a PSG sacrificial layer	
2	do furnace annealing and PSG densification	
3	perform photolithograph	mask #1
4	pattern the PSG with buffered HF solution	
5	deposit a thick silicon nitride layer	
6	perform photolithograph to pattern the etch windows	mask #2
7	etch through the silicon nitride using plasma etcher	
8	etch PSG sacrificial layer in concentrated HF solution (49 wt.%)	
9	deposit a thick LTO to seal the etching windows	

Table 2.2: Flowchart for Fabrication of the Microchannels (II)

1	deposit a thin layer of silicon nitride	
2	pattern the nitride down to silicon substrate	mask #1
3	etch down silicon substrate	
4	perform wet oxidation	
5	remove the silicon nitride film	
6	deposit the PSG sacrificial layer	
7	and do furnace annealing for PSG densification	
8	perform photolithograph	mask #2
9	etch PSG with buffered HF solution	
10	deposit silicon nitride cover layer	
11	perform photolithograph to pattern the etch windows	mask #3
12	etch through the silicon nitride with plasma	
13	etch PSG sacrificial layer to free release the microchannels	
14	deposit thick LTO to seal the etching windows	

can see, the fabrication of a microchannel alone needs only two masks. One disadvantage of this type of microchannel is that the surface topology is not smooth. The height of the surface step is equal to the thickness of the PSG film. In order to have good step coverage, a very thick silicon nitride layer needs to be deposited when the channel height is large. Since the concentrated HF solution will also attack the silicon nitride film (experiments show that HF of 49 wt.% etches the low-stress silicon nitride film at about 40~50 Å/min), bad step coverage can lead to leaks, even total destruction of the microchannel if it is over exposed in the concentrated HF solution.

This problem can be minimized if the surface topology is smoothed. Fig. 2.3(b) shows one of the methods which uses local oxidation (LOCOS) to smooth out the surface. The fabrication is a little bit more complicated than that for the first type of microchannel. In addition to the steps described above, several steps related to LOCOS are inserted. The major fabrication steps are listed in Tab. 2.2.

Fig. 2.4 shows the surface profile of a recessed microchannel scanned by Alpha-step 2000. The height of microchannel is about 1.2 microns while the height of the bump is only about 200 nm. This type of microchannel has been used in the first and second generation microflow measurement system which are described in detail in Ch. 3-5.

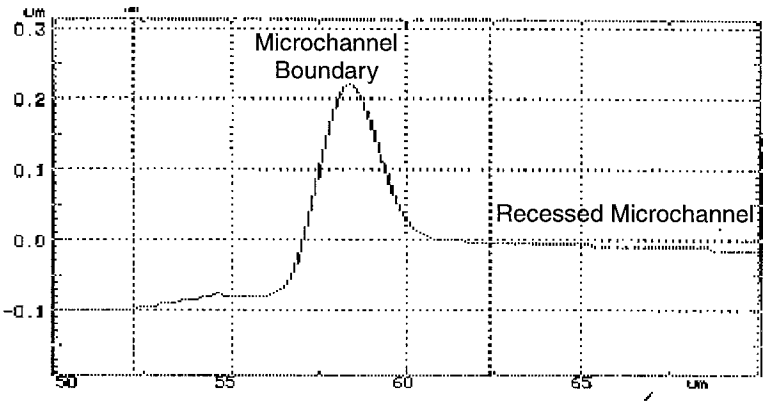

Figure 2.4: Surface profile of a recessed microchannel.

2.3 Microchannel Etching Modelling

2.3.1 Etching Characterization

To characterize the etching process, a dimensionless quantity E_s may be defined as

$$E_s = \frac{A_c}{A_s} \tag{2.4}$$

where A_c is the contact area between the chemical etchant and film to be etched; A_s is the patterned surface area to be etched away. In the case of microchannel etching, for example, the A_c is the cross-sectional area of the microchannel, while the A_s is the surface area of the channel (=length×width of the channel).

In the conventional IC fabrication, etching process is used for patterning structures. Under etch should be avoided if possible since it makes the final geometry size of the patterns different from the design specifications. However, in micromachining technology, etching process is used sometime to pattern structures, sometime to free-release micromechanical structures. In later cases, the fast underetching is preferred. These two applications can be well characterized with the E_s values. In micromachining technology E_s varies from one to much less than one while in IC fabrication $E_s \sim 1$. In other words, if the etching is used to transfer patterns, then $E_s \sim 1$; if the etching is used for structures free-release, then usual $E_s \ll 1$.

There are usually two most important mechanisms in the chemical etching process. One is the chemical reaction; the other is chemical transportation. From the values of E_s, one can tell which mechanism is more important. For a case of $E_s \sim 1$, a constant concentration can be assumed as long as the certain conditions are satisfied, for example, sufficient chemical solution and agitation in wet etching; constant power, pressure and gas flow rate in plasma etching. As a result, the etching rate will be dominated by the chemical reaction rate and can be assumed constant during the whole etching process. However, for the case of $E_s \ll 1$, constant concentration at the etching front can not be guaranteed even with strong agitations. Chemical transportation mechanisms will affect, and eventually dominate the etching progress. Etching rate will generally decrease with time.

Modelling the etching process with $E_s \sim 1$ is relatively easy. Once the rate is experimentally determined, the etching time can be found simply by dividing the thickness of the film with the etching rate. However, for the case $E_s \ll 1$, modeling becomes very complicated. Factors such as chemical reaction rate, transportation, pattern geometry, etc., all have to be considered. To my knowledge, so far, there is still no process simulation for sacrificial layer etching since many necessary parameters are unknown.

2.3.2 Microchannel Etching Data Collection

Uniform Microchannel for Etching Experiments

Normally, to find the etching rate of silicon dioxide or PSG, one would dip a sample into HF. After a certain amount of time, weight (for bulk material) or film thickness is measured. However, if the PSG layer is used as a sacrificial layer, the etching is usually carried out in concentrated HF based solutions where the etching rate is extremely fast. The traditional methods of measuring the rate would be inaccurate. Furthermore, the diffusion effect on etching rate has to be studied with other methods in case E_s is much less than one. One method used by D. J. Monk[11] is to etch a PSG channel encapsulated in silicon nitride and monitor the change of etched distance. To measure the etching distance, the chip has to be take out from the chemical etchant and rinsed. This method is modified here; the etching process is *in*-situ monitored under microscope so that the error caused by the rinse

is avoided and much more data points can be collected.

Straight one dimensional PSG microchannels of different dimensions have been fabricated. Fig. 2.5(a) shows the cross-section of a channel. One end of each channel is completely sealed, while the other end is an etching window. The typical length of the channels is 3 mm. The widths of these channels range from 2 μm to 200 μm. The height of the channels, which is also the PSG thickness, is 1 μm if not specifically mentioned. To facilitate the measurement of the etching lengths under a microscope, scales with 10 μm per division were integrated on the chip. Fig. 2.5b is a photograph of three channels which have been etched partially in HF solution.

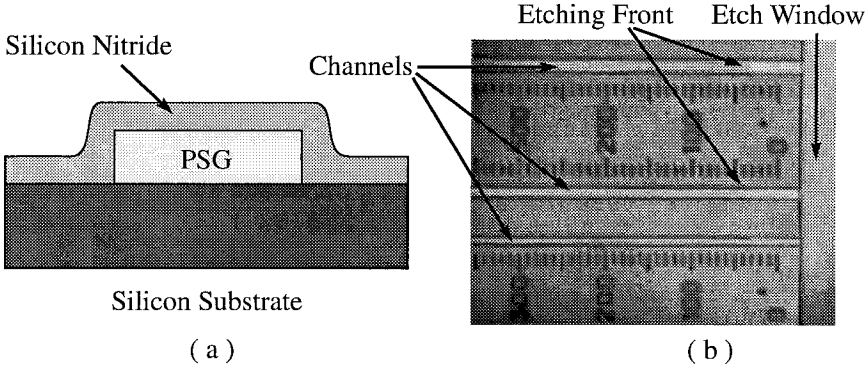

Figure 2.5: (a)The cross-sectional schematic of a PSG microchannel. (b) Photograph of a set of three PSG microchannels for *in*-situ etching monitoring.

Experimental Setup and Results

Etching experiments are carried out under an *in*-situ monitoring system which is schematically shown in Fig. 2.6. This monitoring system consists of a microscope, a video camera, a tape recorder, and a temperature-controlled hot chuck. Etching of the chip is performed in a specially designed polypropylene container with a transparent plastic cover slide. A chip is fixed inside the container and HF solution is injected into the container to start the PSG etching. The whole process is video-recorded. Later on, data of channel etching length vs. time are read from tape. The hot chuck is used only for study of temperature effects.

One problem found during etching is the HF vapor condensation on the container

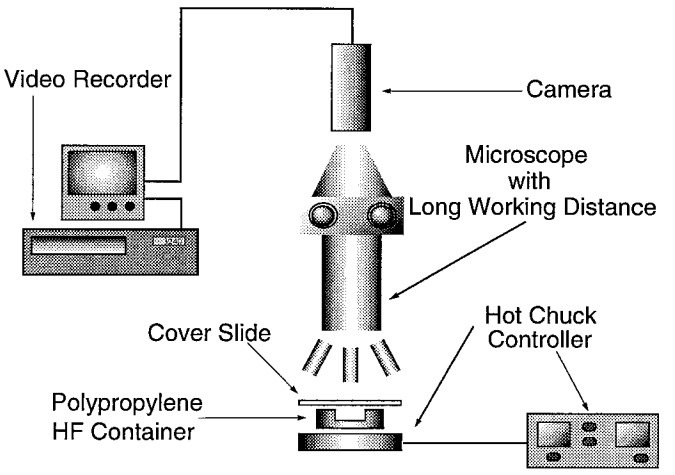

Figure 2.6: Schematic of experimental setup for PSG sacrificial layer etching.

cover slip. Because of this, the cover slip has to be replaced every couple of minutes in order to maintain a clear image on the camera. A plastic patch dish cover can last longer than glass cover between every replacement. Care must be taken due to the potential danger from any spit of HF solutions.

Another problem is the control of etching start-up. Since the initial etching is very fast, a one minute time error can lead to tens of micron inaccuracy in final data. Thus the etching start time must be controlled as accurately as possible. Using the method described before, injecting HF into the container can reduce the timing error down to several seconds.

Fig. 2.7 shows the experimental results, namely the curves of etched distance in microchannels vs. time for several different bulk concentrations. The microchannel etching experiments have been carried out with more than 20 chips; each includes a different set of microchannels. Each curve in Fig. 2.7 is an average of measurements of many samples. Bars in the plot represents the scattering of the data. Since the etched distance does not depend upon the width of the microchannels (details to be discussed in section 2.4), the data from microchannels with different width are put together as long as the other etching conditions such as temperature, bulk concentration, etc., are the same.

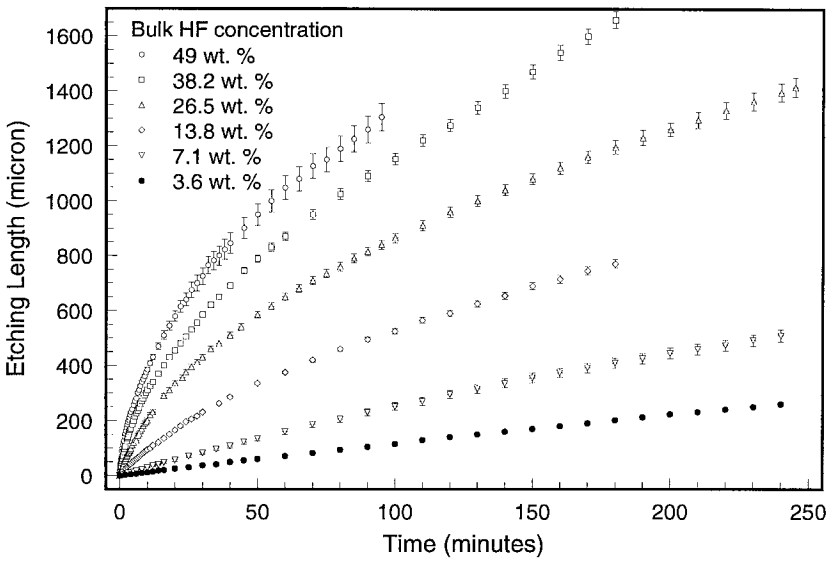

Figure 2.7: The curve of microchannel etching distance vs. time. The data are collected from many microchannels with different width and from different chips, but the same batch of fabrication. Vertical bars represent the scattering of these measurements.

2.3.3 Universal Modeling

Recently, Monk et el.[12, 11] reported the first study of PSG etching in microchannels using HF-based solutions. Both Deal-Grove and non-first-order models have been examined. It was shown that under specific concentrations both models can fit etching data well. However, no information on the applicability of the models over a wide range of HF concentration was provided. In fact, from our data, we have found that neither model is universal. Here, we present our work to find a universal model which includes a first-and-second order chemical-reaction mechanism.

To model the etching, we make the following assumptions: the channel Etching is one dimensional; the diffusion coefficient is a constant; all the liquid has a constant density; the heat generation at the etching front is negligible; the reaction products have no chemical effects on the reaction-chemical distribution. We also assume that the overall chemical reaction is

$$6HF + SiO_2 \rightleftharpoons H_2SiF_6 + 2H_2O \tag{2.5}$$

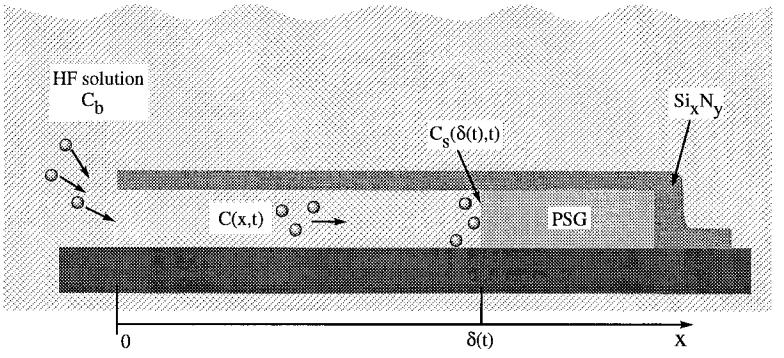

Figure 2.8: Conventions used in our model formulation.

Using the coordinates defined in Fig. 2.8, the continuity equation for reaction chemical concentration is

$$\frac{\partial C}{\partial t} + u\frac{\partial C}{\partial x} = D\frac{\partial^2 C}{\partial x^2} , \tag{2.6}$$

where u is the flow velocity, $C(x,t)$ is the concentration of the reaction chemical and D is the diffusion constant. The diffusive flux, J_d, is then given by Fick's first law,

$$J_d = -D\frac{\partial C}{\partial x} . \tag{2.7}$$

We wish to determine the relative magnitude of the convection and diffusion term in Eq. (2.6). According to Eq. (2.5), there is a volume change of the liquid at the etching front that for the etching of every mole of SiO_2, there is a generation of 2 moles of H_2O. The molecular weight, [MW], of SiO_2 and H_2O is 60 and 18 g/mole, respectively. Their corresponding densities, ρ, are 2.1 and 1 g/cm^3. Thus, for every mole of SiO_2 etched, the solid volume decreases by 28.6 cm^3, but the liquid volume increases by 36 cm^3. The net volume change then is an increase of 7.4 cm^3/mole ($\sim$ 26%). The velocity of the etching front is found experimentally to be 20 μm/min for PSG in 49 wt.% HF. Thus, the back-flow velocity, u, caused by volume increase is about 6 μm/min. With a $D \sim 3 \times 10^{-5}$ cm/sec,

the order-of-magnitude estimate of the ratio between the convective and diffusion terms is

$$u\frac{\partial C}{\partial x}\Big/ D\frac{\partial^2 C}{\partial x^2} \approx \frac{u\delta(t)}{D} \sim 3\times 10^{-5}\frac{\delta(t)}{\mu m} \ . \tag{2.8}$$

It can be concluded that for $\delta(t)$ up to several thousand microns, the convection term in the continuity equation is negligible. This, however, may not be true if forced-convection sources, such as bubble formation, exist.

Neglecting the convective term, the governing equation now becomes

$$\frac{\partial C}{\partial t} - D\frac{\partial^2 C}{\partial x^2} = 0 \ . \tag{2.9}$$

The boundary conditions are

$$\begin{aligned} C(0,t) &= C_b \ , \\ C(\delta(t),t) &= C_s \ , \end{aligned} \qquad \text{for} \quad t>0 \ , \tag{2.10}$$

where C_b is the bulk HF concentration, and C_s is the etching front concentration. To solve Eq. (2.9) and (2.10), we need a third boundary condition which can be derived as follows. In a stoichiometric reaction, one has

$$J_{[SiO_2]} = \frac{1}{6}J_{[HF]} \ , \tag{2.11}$$

and the etching rate is proportional to the SiO_2 flux at the front,

$$\frac{d\delta}{dt} = J_{[SiO_2]}\frac{[MW]_{[SiO_2]}}{\rho_{[SiO_2]}} \ . \tag{2.12}$$

From Eq. (2.7), (2.11) and (2.12), the third boundary condition is

$$\frac{d\delta}{dt} = -\frac{D_{[HF]}}{6}\frac{[MW]_{[SiO_2]}}{\rho_{[SiO_2]}}\frac{\partial C}{\partial x}\Big|_{x=\delta(t)} \ , \tag{2.13}$$

where $D_{[HF]}$ is the diffusion constant of the HF molecule in the etching solution. Eq. (2.9), (2.10) and (2.13) form the basis for the following models.

Diffusion Model

If the chemical reaction rate is very high, the etching speed of the microchannels is limited by diffusion. In this case, concentration of reactant chemicals at the etching front would

be very low. In the extreme, $C_s = 0$. Eq. (2.9) with boundary conditions (2.10) and (2.13) then represent a standard one phase Stefan problem[13]. The solutions are

$$C(x,t) = C_b - \frac{6\rho_{[SiO_2]}}{[MW]_{[SiO_2]}} A e^{A^2/4} \int_0^{\frac{x}{2\sqrt{Dt}}} e^{-\xi^2} d\xi \ , \tag{2.14}$$

$$\delta(t) = A\sqrt{Dt} \ , \tag{2.15}$$

where the constant A can be solved by

$$A e^{A^2/4} \int_0^{\frac{A}{2}} e^{-\xi^2} d\xi - \frac{[MW]_{[SiO_2]}}{6\rho_{[SiO_2]}} C_b = 0 \ . \tag{2.16}$$

There are two good reasons to study the diffusion model. First, the diffusion model helps to justify a very important simplification that the HF concentration distribution inside the etched channel is linear as shown in Fig. 2.9a. Secondly, because $C_s = 0$ is assumed, Eq. (2.15) predicts the maximum etching length as a function of t. Alternatively, the best fit of the data to Eq. (2.15) gives the lower limit of diffusion coefficient, D_{min}. As shown in Fig. 2.9b, a lower limit of D of 1.2×10^{-5} cm^2/sec is found from our data. However, Fig. 2.9b also shows that the diffusion model is not a universal model. This is because in reality $C_s \neq 0$.

Deal-Grove (D-G) Model

In the D-G model, the concentration in the channel is assumed to be linear as justified by diffusion model, so

$$J_d = -D\frac{\partial C}{\partial x} = D\frac{(C_b - C_s)}{\delta} \ . \tag{2.17}$$

Furthermore, the rate of chemical reaction is assumed to be linearly proportional to the etching front concentration,

$$J_{[HF]} = kC_s \ , \tag{2.18}$$

where k is the first-order reaction rate coefficient. $J_{[HF]}$ is the reaction flux of HF. In steady state, $J_d = J_{[HF]}$, the solution of the D-G model is[11],

$$\delta = -\frac{D}{k} + \sqrt{\left(\frac{D}{k}\right)^2 + \frac{DC_b[MW]_{[SiO_2]}}{3\rho_{[SiO_2]}} t} \ . \tag{2.19}$$

D-G model is a first-order chemical reaction model. This model fails to fit our etching experimental data as shown in Fig. 2.10.

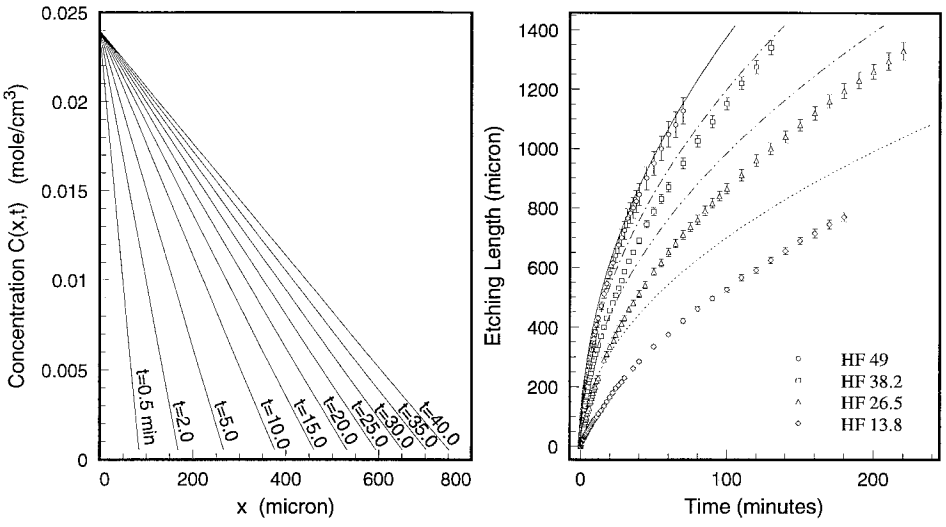

Figure 2.9: (a) Calculated concentration distribution along microchannels assuming $C_s = 0$. (b) Fitting of the diffusion model to experimental data with $D = 1.2\times10^{-5}$ cm^2/sec. Clearly, the diffusion model can not fit a wide range of HF concentration, hence it is not universal.

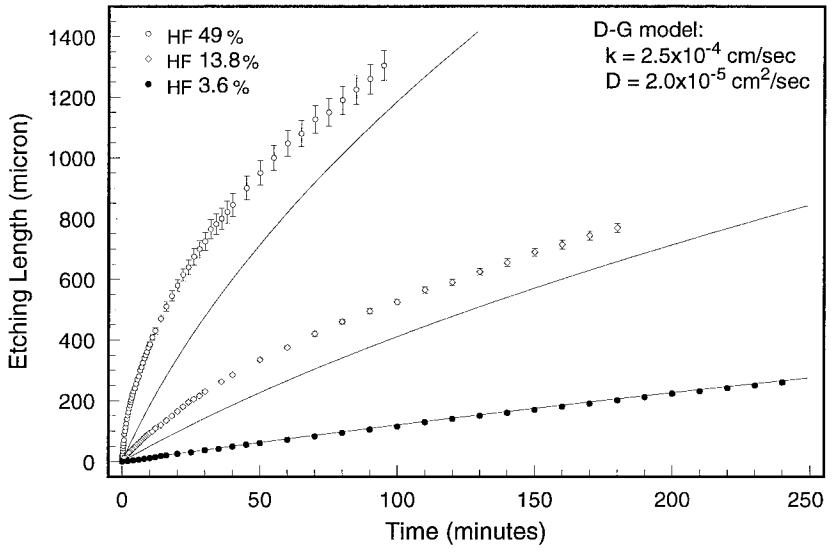

Figure 2.10: Fitting of D-G model to experimental data. Obviously, D-G model is not universal.

Combined First-and-Second Order Model

In this model, the concentration distribution is also linear such that, in steady state,

$$J_{[HF]} = D\frac{(C_b - C_s)}{\delta} \ . \tag{2.20}$$

However, the reaction rate equation includes both a linear and a quadratic term,

$$J_{[HF]} = k_1 C_s + k_2 {C_s}^2 \ . \tag{2.21}$$

Solving Eq. (2.20) and (2.21), one has,

$$J_{[HF]} = \frac{1}{2k_2}\left(\frac{D}{\delta}\right)^2\left(1 + b\left(\frac{\delta}{D}\right) - \varphi\right) \ . \tag{2.22}$$

where

$$\begin{aligned} b &= k_1 + 2C_b k_2 \ , \\ \varphi &= \sqrt{1 + 2b\left(\frac{\delta}{D}\right) + k_1^2\left(\frac{\delta}{D}\right)^2} \ . \end{aligned} \tag{2.23}$$

Substitute Eq. (2.22) into Eq. (2.11) and (2.12), and a first order differential equation can be derived as

$$\frac{d\delta}{dt} = a\left(\frac{D}{\delta}\right)^2\left[1 + b\left(\frac{\delta}{D}\right) - \varphi\right] \ . \tag{2.24}$$

where $a = [MW]_{[HF]}/4\rho_{[SiO_2]}k_2$. This equation can be solved numerically. However, instead of searching for solutions of the form $\delta = f(t)$, one can integrate this equation from $\delta = 0$ at $t = 0$ to δ at time t to find:

$$\begin{aligned} t &= \frac{D\left\{\varphi\phi + 2k_1^2\left(\frac{\delta}{D}\right) + b\left(k_1^2\left(\frac{\delta}{D}\right)^2 - 1\right)\right\}}{8aC_b k_1^2 k_2(k_1 + C_b k_2)} \\ &\quad - \frac{D}{2ak_1^3}\log\frac{\phi + k_1\varphi}{2\left(k_1 + C_b k_2\right)} \ , \end{aligned} \tag{2.25}$$

where

$$\phi = k_1 + 2C_b k_2 + k_1^2\left(\frac{\delta}{D}\right) . \tag{2.26}$$

Coefficients of k_1, k_2, and D can be determined experimentally. A non-linear least-square-fit method (*Levenberg-Marquardt method*[14]) is used to fit Eq. (2.25) to experimental data, and results are shown in Fig. 2.11.

In Fig. 2.11, bulk concentration, C_b, varies from 3.6 to 49 wt.%. The data are collected from many etching experiments with data scattering represented by the error

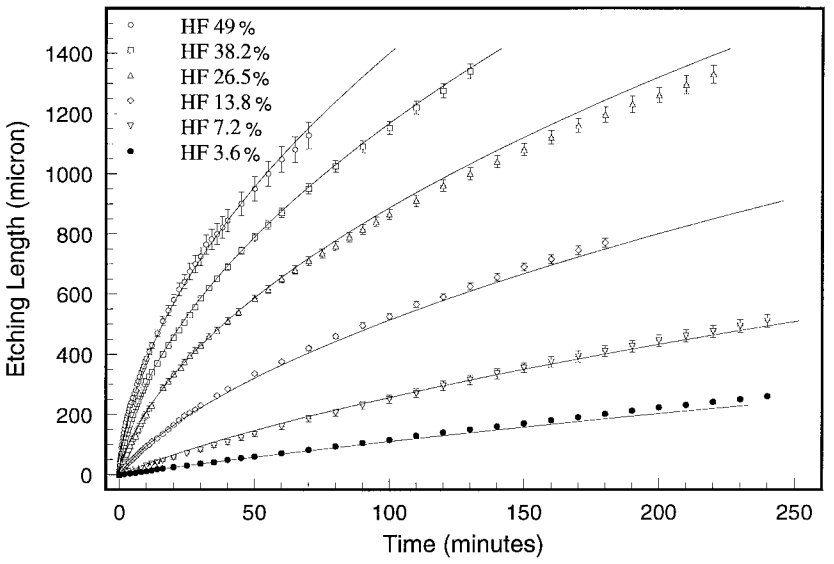

Figure 2.11: PSG channels etching with different HF concentration. Vertical bars show the scatter of different channel etching data. Solid lines are our model with parameter $k_1 = 1.2 \times 10^{-4}$ cm/sec, $k_2 = 6.5 \times 10^{-2}$ cm^4/mole·sec, and $D = 1.6 \times 10^{-5}$ cm^2/sec. A wide range of good fit is obtained.

bars. Clearly, this model fits all the data well using $k_1 = 1.2 \times 10^{-4}$ cm/sec, $k_2 = 6.5 \times 10^{-2}$ cm^4/mole·sec, and $D = 1.6 \times 10^{-5}$ cm^2/sec. Note that the diffusion constant, D, is indeed larger than D_{min} (1.2×10^{-5} cm^2/sec) predicted from the diffusion model.

Another useful equation relating C_s with δ can be derived from Eq. (2.20) and (2.21) which is

$$C_s = \frac{-D - k_1\delta + D\varphi}{2k_2\delta} \,. \tag{2.27}$$

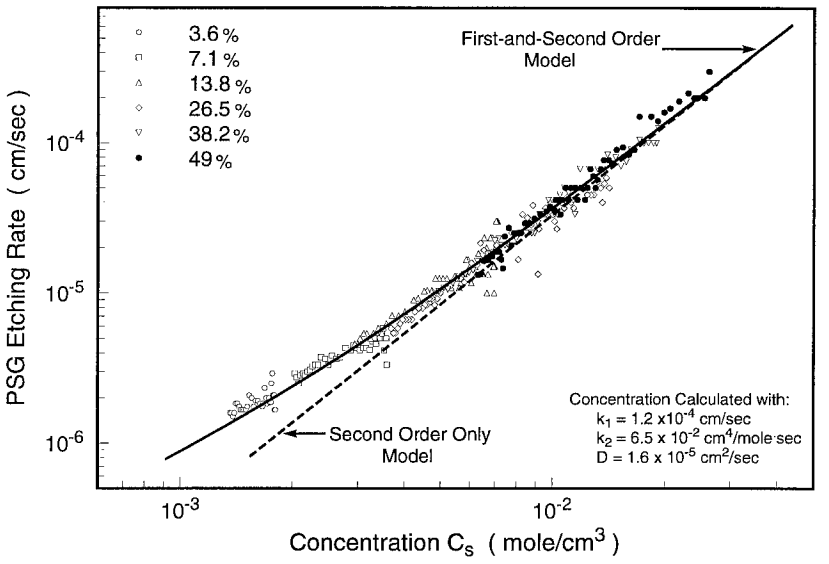

Figure 2.12: PSG etching rate dependence on concentration, C_s. Solid line represents the first and second order model with parameters shown in the graph.

With Eq. (2.27) we can plot an etching rate vs. HF concentration curve at the etch front for each set of experimental data by taking time derivatives of the data shown in Fig. 2.11. Results are presented in Fig. 2.12. Since etching rate depends only upon concentration, all the data point should fall into a single smooth curve according to the formula expressed parametrically by Eq. (2.25) and (2.27). Again, the results in Fig. 2.12 confirms our model in predicting correct etching for all concentrations.

Fig. 2.13 further shows concentration variation at the etching front. Initially, HF concentration drops very fast for high concentrated HF. After several hundreds microns, the concentration varies slowly as in low HF concentration.

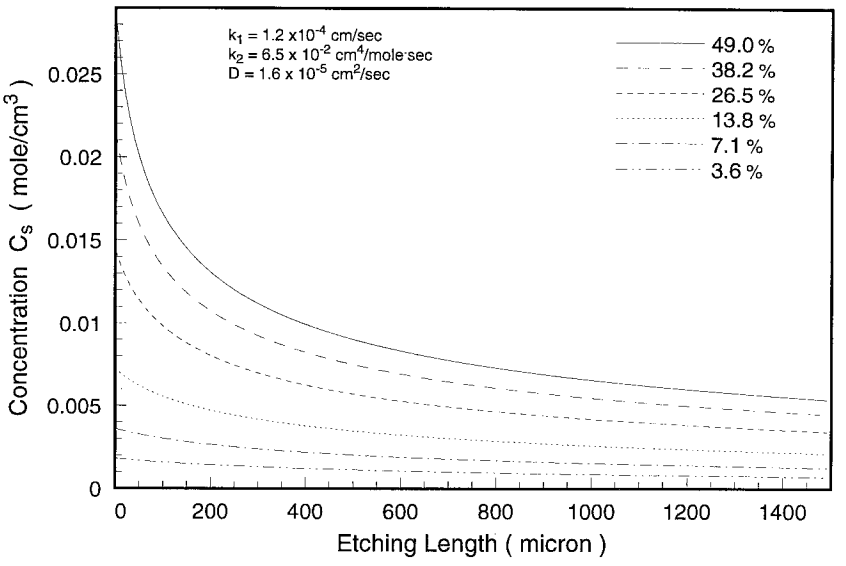

Figure 2.13: Concentration at the etching front.

Finally, Langmuir-Hinshelwood (L-H) chemical kinetic model has also been proposed to predict etching process ($r = -k_1[HF]/(1 + k_2[HF])$)[15]. We solved L-H and diffusion coupled model numerically. We have found that even with three fitting parameters, the L-H model fails to fit the data universally.

2.3.4 Discussion

Chemical Foundation for the Universal Model

As shown, among all the models, the combined first-and-second model is the only one which can fit universally. It clearly means, at low concentrations, the etching is dominated by a first order chemical reaction, and at high concentrations by a second order chemical reaction. In fact, Eq. (2.21) is reasonable from other chemistry studies which are summarized in the following.

The aqueous HF solutions are characterized by the following equilibria[15],

$$HF \rightleftharpoons H^+ + F^- , \tag{2.28}$$

$$2HF \rightleftharpoons H^+ + HF_2^- , \tag{2.29}$$

$$\cdots \qquad \cdots$$

$$iHF \;\rightleftharpoons\; H^+ + H_{i-1}F_i^- \ . \tag{2.30}$$

In equilibrium, many species such as H^+, F^-, HF, HF_2^-, etc., can exist simultaneously. It has been shown that free fluoride can be excluded from one of the species responsible for the silicon dioxide etching[16, 15]. A rate equation of the form,

$$-r = A[HF] + B[HF_2^-] + C \ , \tag{2.31}$$

was therefore proposed by Judge[16]. He concludes that the reaction with HF_2^- is about four to five times as fast as the reaction with HF. On the contrary, however, Kline[15] claims that rapid dissolution of silicates by hydrofluoric acid can be completely attributed to HF molecules. Nevertheless, neither can explain concentrated HF etching data. This problem may be solved using Eq. (2.29) from which one can write

$$-r = C_1[H^+][HF_2^-] = C_1C_2[HF]^2 \ . \tag{2.32}$$

This rate law was reported by Born in 1979 and was added to Eq. (2.31) by Helms in 1991 in order to fit data collected using concentrated hydrofluoric acid[17]. Recently, Monk[11] used a non-first order rate law in his study of PSG etching by high concentrated HF and fit his data successfully. But it was not pointed out in which order the model was. In our work, it is found that the second order term is dominant at high HF concentration.

Finally, the etching rate of PSG (phosphorsilicate glass) is different from that of SiO_2. The rates for variously doped SiO_2 in buffered HF solution have been reported by Kikuyama[5]. However, the mechanism that phosphorus doping changes the etching rate of silicon dioxide is still unclear. Kikuyama's study with doped oxide suggests that the etching difference between doped and undoped SiO_2 is caused by valence differences between silicon and the dopant elements. According to him, the role of phosphorus is to weaken silicon-oxygen bonds in the doped film thus facilitating the etching process. This agrees with the etching mechanism described by Prigogine. A cautious conclusion, however, is that the basic chemistry is unaffected by the presence of phosphors. Therefore, the rate law for SiO_2 etching should be applicable to PSG etching. This agrees with our modelling results where same chemical reaction mechanisms have been used for both SiO_2 and PSG.

2.4 Design and Etching Experiments of Microstructures

2.4.1 Microchannel Design

As mentioned before, the critical points of microchannel design is the layout of etching holes. In order to etch a microchannel millimeters long, a number of etching holes have to be placed along the channel (Fig. 2.14). The distance between two etching holes, l, determines the etch time. Small distance or, in other words, more etching holes means short etching time. In a microchannel system for fluid flow studies, however, it is preferred to have fewer etching holes since the introducing of the holes unavoidably interferes with the fluid flow. But if the number of etching holes is too small, it will take a very long time to etch a microchannel, and extended exposure of the microdevices to the concentrated HF can also cause structure damages. Therefore, the design of etching holes should be optimized.

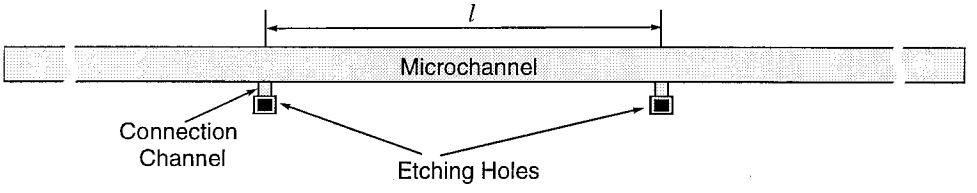

Figure 2.14: Design schematics of the microchannel with holes for etching PSG sacrificial layer.

With the universal model proposed in the previous section, the etching process can be simulated in a computer. For a straight channel with holes placed directly on top of the channel, the 1-D universal model can be used. However, for structures like the one shown in Fig. 2.14 where the etching holes are placed beside the microchannel (connected together through a small bridging channel), it is necessary to consider the effect of etching holes. In other words, a two dimensional simulation is necessary. If the microchannel is fabricated using a composite sacrificial layer, for example, PSG/SiO_2, the simulation is even more complicated. Unfortunately, this is the actual situation of the microchannel used in the microflow system.

Realized that the computer simulation is a very time consuming work, experimental

methods are used to determine the etching time. Fig. 2.15 shows the various test patterns used in the experiments. These test patterns are designed with following two considerations in mind:

1. Study the effect of the width of the etching holes to the microchannel etching.

2. Study the effect of the connecting channel length (connect the etching holes to the flow channel).

Fig. 2.15 shows some test patterns used in the etching experiments. Group I and Group III are various combinations of etching hole position and width of channels.

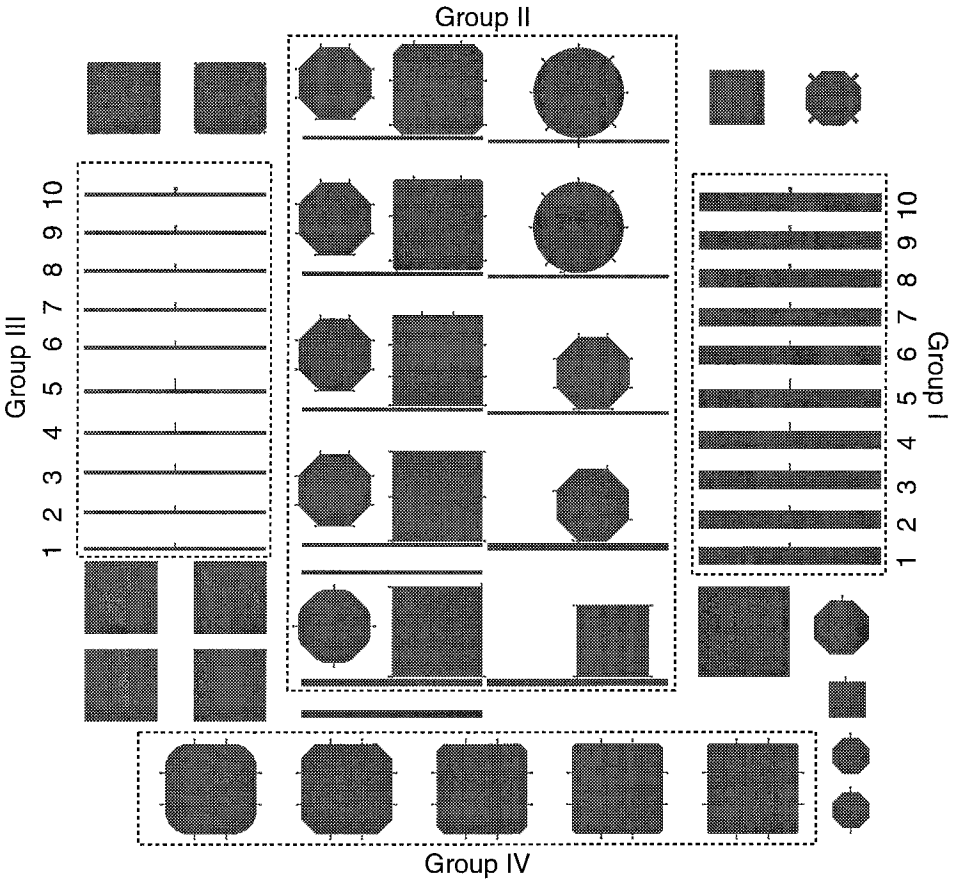

Figure 2.15: Test patterns for etching experiments.

2.4.2 Design of 2-D Structures

The integrated microflow system requires not only the microchannel for the fluid flows, but also pressure sensors for measuring the pressure in the fluid. Each pressure sensor has a chamber with silicon nitride as its diaphragm material. The free-standing diaphragm can be made with similar sacrificial layer etching technique as the microchannel fabrication. In the integrated microflow system (Chapter 4), the chamber and the microchannel are formed at the same time during the fabrication, namely after PSG/SiO_2 sacrificial layer free etching. The universal etching model developed from the 1-D microchannel etching experiments can also be used for modeling the 2-D chamber etching.

However, the geometry differences between the microchannels and the chambers are significant enough such that etching experiments with specifically designed 2-D structure are necessary.

Group II and IV in Fig. 2.15 are some of the test patterns designed for the purpose of finding the optimum etching time and geometry for the micro chambers.

2.4.3 Discussion of Experimental Results

Etching Hole Effects

Fig. 2.16(a) shows a snap shot of the microchannel etching process. As one can see, the etched distance (from the etching front to the connection channels) decreases as the length of the connection channel increases or the width of the connection channel decreases. This clearly shows that the etching is affected by the design of the etching holes. To reduce the time of etching a certain length of microchannel or, in other words, increase the etching rate, the width of connections channels should be wide enough; and its length should be as short as possible. The best is to place the etching holes directly on top of the microchannel (Fig. 2.17(c)). However, considering the etching hole is to be sealed after the etching. The etching holes can never be placed on top of the flow channel.

Fig. 2.16(b,c) shows the snap shots at two different moments of the etching process for a group of non-uniform cross-section microchannels. As one can see, the converging channel 2 (the cross-section is decreasing) is the fastest to be etched. Diverging channel 3

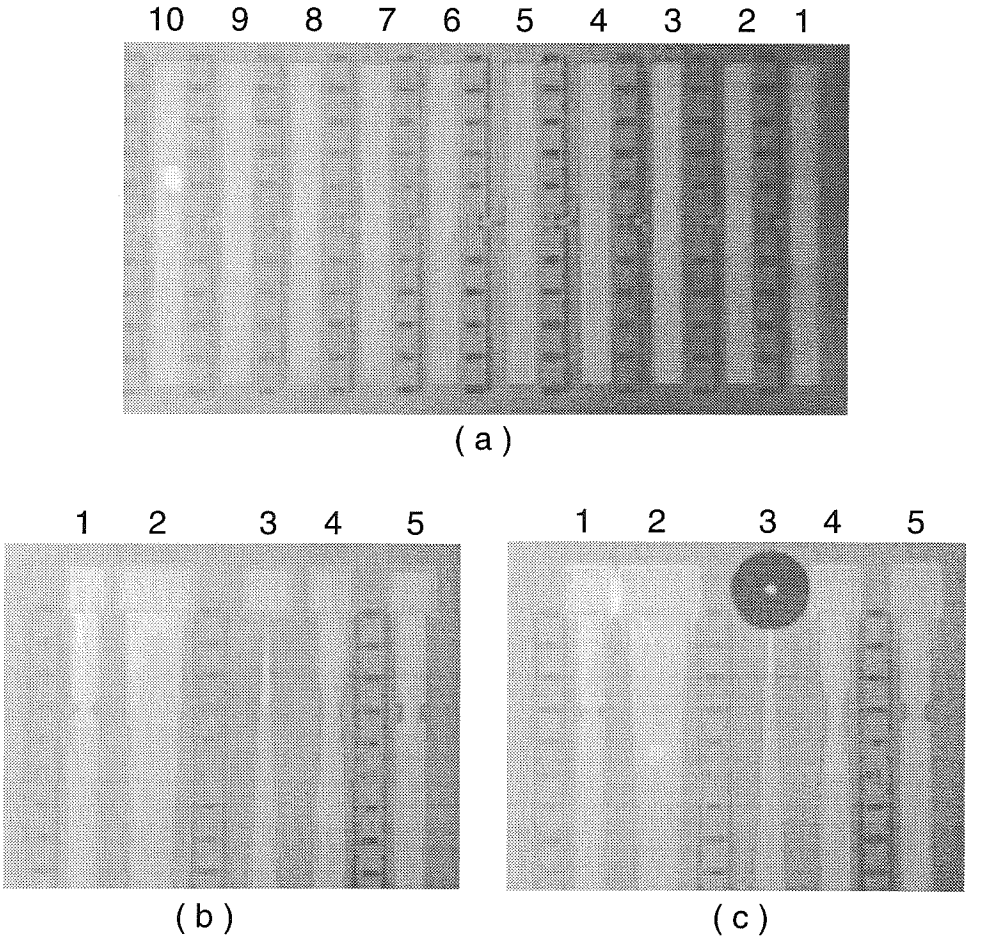

Figure 2.16: Snap shot photograph of the microchannel etching process. (a) Group I microchannels in the Fig. 2.15. (b, c) Etching of various non-uniform microchannels at two time instant.

(the cross-section is increasing) is the slowest in the group. The reasons are obvious. The other three channels (1,4,5) are almost the same in terms of the etched distances. The difference between these three channels only shows up after at least several hundreds of microns being etched away.

Fig. 2.17(a,b) are the snap shots of micro chamber etching process. As expected, the chamber which has the most holes is the fastest to be etched.

Temperature Effect

During the course of data collection, we have found many factors which can potentially affect the reliability of our data. Temperature is one of these factors. Fig. 2.18(a) shows our preliminary experimental results of the etching length vs. time under different temperatures. It is interesting to see that higher temperature increases the etching speed at least at the beginning of the etching, which shows that the reaction constants are sensitive to temperature[16]. It is also interesting to see that after 300 μm channel etching, bubbles start to form and the etching lengths, after 100 minutes, are almost the same even at different temperatures. We believe that bubble-enhanced convection is the reason to explain this phenomenon.

Microchannel Height Effects

From the experiments, it is first observed that the width of the uniform microchannels does not affect etching speed for widths ranging from 4 μm to 200 μm as long as channel thickness is the same. On the other hand, thickness is found to have significant effects on the etching speed as shown in Fig. 2.18(b). Samples with heights from 0.24 μm to 1.7 μm are etched in 26.5 wt% HF solution. Results show that thinner PSG channels are etched much slower than the thicker ones.

There are two possible reasons for the height dependence of etching rate; one is surface interaction between solid and liquid which may either increase or reduce etching rate. The other is that flow is involved in the etching. In this case, we would expect that the etching rate will increase with the channel height since the channels with larger cross-sections tend to allow stronger fluid motion.

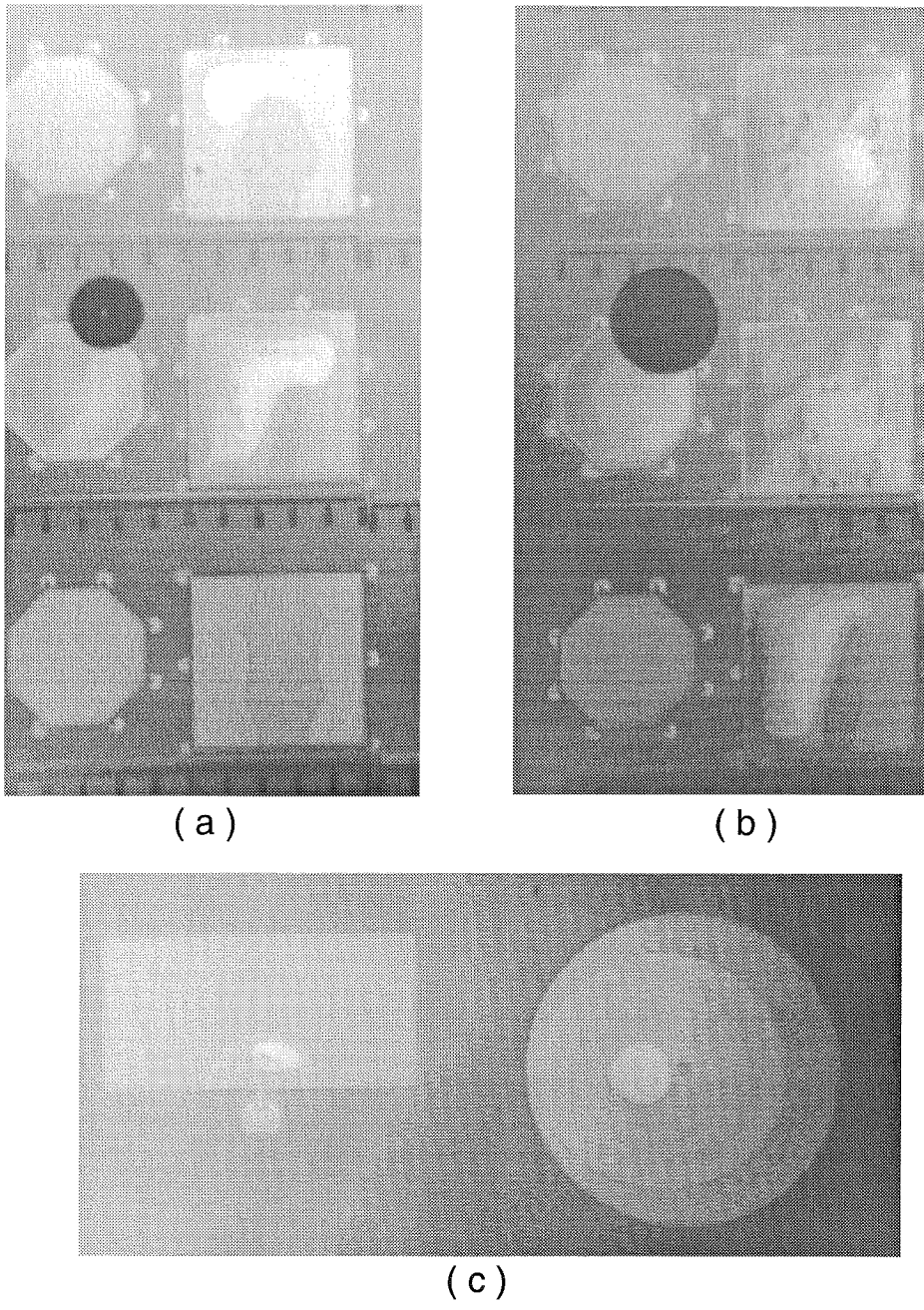

Figure 2.17: Snap shot photograph of two dimensional chambers. (a, b) Etching holes are placed around the chambers (c) The left rectangular chamber has one etching hole on its edge; the right circular pattern has one etching hole in the center.

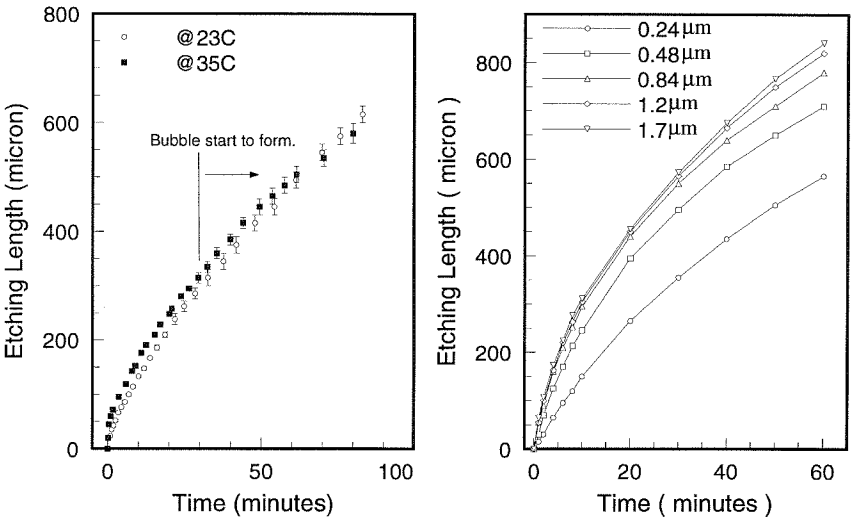

Figure 2.18: (a) PSG channels etching at different temperatures. (b) Five PSG channels of different thickness etching in 26.5 wt.% HF solution.

Bubble Effect

From *in*-situ monitoring channel etching, we have observed bubble forming and moving inside the channels and chambers. In KOH etching silicon, bubble formation has been reported[18]. Since the chemical reaction between SiO_2 and hydrofluoric acid does not generate gas product, it is not expected to see the bubbles. In fact, we have found no other reports on bubble formation in HF etching.

From our experiments, it is found that bubbles always form certain time after etching begins. Once bubble formation is initialized, it will not stop by itself. In most of the cases, the bubbles grow in size inside the channel and move out of the channel repeatedly. Fig. 2.19 shows such a process of bubble forming. Photograph in Fig. 2.17 all show the bubbles.

Effects of the bubbles on channel etching depend upon the size of the channels. Since bubbles are always in motion (they move out from the etching channel and, at the same time, expand in volume), micro-convection can be induced if channel sizes are large, otherwise liquid is pushed out for awhile in small channels. Thus there is a width threshold of about 10 μm. Above this, etching rate may speed up. Below this threshold, etching rate slows down. In the case of 2D chambers, etching always speeds up once bubbles start to

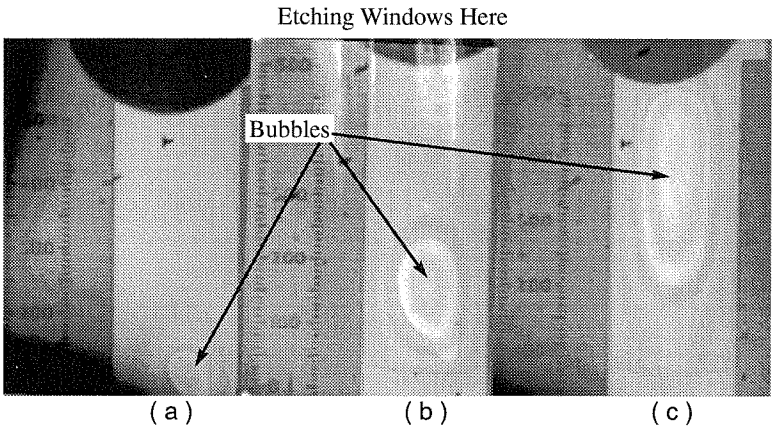

Figure 2.19: Bubble formation and its sequential movement. (a) A bubble forms near the etching front. (b) The bubble moves toward the etching window. (c) The bubble reaches the etching window. Note that the bubble grows in size during its movement.

form. This can be clearly seen in Fig. 2.17. In Fig. 2.17(c), the etched circle is initially symmetrical around the center hole; however, since the bubble forms, the etching front becomes asymmetrical; the etching front at the bubble side moves faster than the other part.

Another interesting phenomenon related with the bubbles are the liquid condensation on the inner surface of the diaphragm. Fig. 2.17(b) shows this phenomenon. This may imply that the gas in the bubble is vaporized HF solution.

Finally, we find that bubble formation is very sensitive to temperature. The generation rate and moving speed after bubble formation decrease with temperature. The lag time for bubble formation, however, increases with temperature decrease.

2.5 Summary

Microchannels are the simplest and the most important fluidic devices. Using surface micromachining technology, microchannel may be fabricated and integrated with other microdevices, for examples, sensors, IC circuits, etc. In this chapter, the fabrication, modeling and design of microchannels are presented. Studies of sacrificial layer etching technology

are carried out in depth through specially designed channels and other test patterns. A universal model has been found for modeling the sacrificial etching process.

The microchannels described in this chapter are attached to the silicon substrate. Since silicon is a good thermal conductor, the conduction of thermal energy from the fluid to the substrate could make the analysis of the results of microflow experiments very complicated. The next improvement is to make a free standing microchannel as shown in Fig. 2.20. A good thermal isolation can be achieved by encapsulating the device in a vacuum chamber. Such a microchannel would be ideal for thermal analysis of microscopic fluid flows.

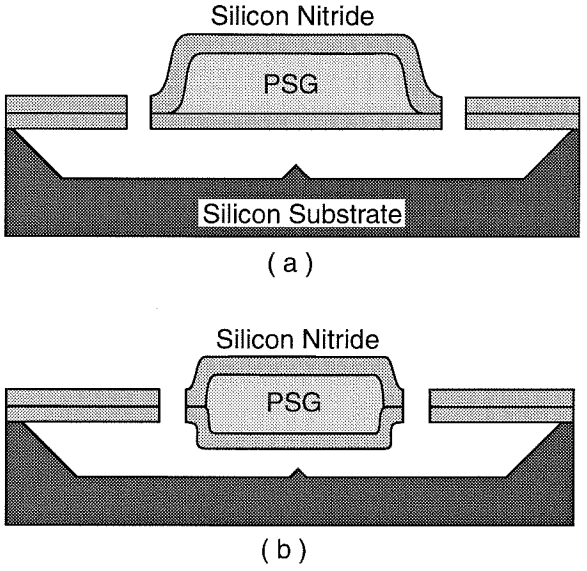

Figure 2.20: (a)Free-standing microchannel for thermal isolation. (b)Recessed free-standing microchannel.

Bibliography

[1] J. Pfahler, J. Harley, and H. Bau, "Gas and liquid flow in small channels," in *Micromechanical Sensors, Actuators, and Systems*, vol. 32, pp. 49–60, ASME, 1991.

[2] L. S. Fan, Y. C. Tai, and R. S. Muller, "Integrated movable micromechanical structures for sensors and actuators," *IEEE Trans. on Electron Devices*, vol. ED-35, no. 6, pp. 724–730, 1988.

[3] D. Poenar, P. J. French, R. Mallee, P. M. Sarro, and Wolffenbuttel, "Psg layers for surface micromachining," *Sensors and Actuators*, vol. 41-42, no. A, pp. 304–309, 1994.

[4] K. Chow and L. G. Garrison, "Phosphorus concentration of chemical vapor deposited phosphosilicate glass," *J. Electrochem. Soc.*, vol. 124, pp. 1133–1136, July 1977.

[5] H. Kikuyama, M. Waki, I. Kawanabe, M. Miyashita, T. Yabune, N. Miki, J. Takano, and T. Ohmi, "Etching rate and mechanism of doped oxide in buffered hydrogen fluoride solution," *J. Electrochem. Soc.: Solid-State Science and Technology*, vol. 139, pp. 2239–2243, August 1992.

[6] C. Pavelescu and C. Cobianu, "Etch rate behaviour of phosphosilicate glass films chemically vapour deposited in the sih_4 ph_3 o_2 n_2 system at low temperature," *Thin Solid Films*, vol. 196, pp. 351–360, 1991.

[7] S. M. Sze, ed., *VLSI Technology*, ch. 6. McGraw-Hill Book Company, 2nd ed., 1988.

[8] M. Sekimoto, H. Yoshihara, and T. Ohkubo, "Silicon nitride single-layer x-ray mask," *J. Vac. Sci. Technol.*, vol. 21, pp. 1017–1021, Nov./Dec. 1982.

[9] R. L. Alley, G. J. Cuan, R. T. Howe, and K. Komvopoulos, "The effect of release-etch processing on surface microstructure stiction," in *IEEE Solid-State Sensor and Actuator Workshop*, (Hilton Head Island, SC, USA), pp. 202–207, IEEE, 1992.

[10] C. H. Mastrangelo and C. H. Hsu, "A simple experimental technique for the measurement of the work of adhesion of microstructures," in *IEEE Solid-State Sensor and Actuator Workshop*, (Hilton Head Island, SC, USA), pp. 208–212, IEEE, 1992.

[11] D. J. Monk, *Controlled Structure Release for Silicon Surface Micromachining.* PhD thesis, University of California at Berkeley, Chemical Engineering, Graduate Division, 1993.

[12] D. J. Monk, D. S. Soane, and R. T. Howe, "A review of the chemical reaction mechanism and kinetics of hydrofluoric acid etching of silicon dioxide for surface micromachining applications," *Thin Solid Films*, vol. 232, pp. 1–12, 1993.

[13] J. R. Cannon, *The One-Dimensional Heat Equation*, ch. 17, p. 281. Addison-Wesley publishing company, 1984.

[14] W. H. Press, B. P. Flannery, S. A. Teukoisky, and W. T. Vetterling, *Numerical Recipes, The Art of Scientific Computing [FORTRAN Version]*, ch. 14, p. 521. Cambridge, 1989.

[15] W. E. Kline and H. S. Fogler, "Dissolution of silicate minerals by hydrofluoric acid," *Ind. Eng. Chem. Fundam.*, vol. 20, no. 2, pp. 155–161, 1981.

[16] J. S. Judge, "A study of the dissolution of sio_2 in acidic fluoride solutions," *Journal of the Electrochemical Socity: Solid-State Science*, vol. 118, pp. 1772–1775, November 1971.

[17] C. R. Helms and B. E. Deal, "Mechanisms of the hf/h_2o vapor phase etching of sio_2," *J. Vac. Sci. Technol.*, vol. A 10, pp. 806–811, July/August 1992.

[18] O. Tabata, K. Shimaoka, and S. Sugiyama, "In-situ observation and analysis of wet etching process for micro electro mechanical systems," *IEEE*, 1991. CH2957-9/91/0000-0099.

Chapter 3

Pressure Sensors

3.1 Introduction

From the theoretical point of view, the pressure distribution inside a fluid channel provides very important information about the state of the fluid. The pressure is also experimentally almost the easiest measurable physical parameter comparing with others such as velocity distribution. It is thus chosen as the first micro device to be integrated with microchannels (microflow measurement system) for studying fluid flow on microscopic scale.

Micro pressure sensors have been developed and widely used for several decades[1]. There are several types of pressure sensors. Piezo-junction pressure sensors utilize pressure-induced changes in reverse leakage current[2]. Piezoresistive sensors employ a thin diaphragm with strain sensitive elements distributed on the diaphragm. These elements can be diffused into the diaphragm (bulk silicon micromachined pressure sensor)[1] or placed on top of the diaphragm (surface micromachined pressure sensor). Another type is capacitive pressure sensor which uses a thin silicon diaphragm as the movable plate of a capacitor[3].

However, so far, all the pressure sensors developed are targeted for certain commercial or industrial applications. To use for an integrated microflow system (an integrated microchannel/pressure sensors chip), there are several issues which need to be addressed. These issues are as follows:

1. *Fabrication Compatibilities*

This issue is related with the fabrication procedure of the pressure sensors. An integrated microflow system includes not only pressure sensors, but also microchannels and other interfacing structures. The fabrications of all these devices have to be compatible with each other or, in other words, each device is fabricated without affecting other devices.

2. *Scale and Sensitivity*

   This issue is related with the design of the pressure sensors. That includes the choices of strain gauge and diaphragm material, size of the diaphragm and dynamic pressure range in which a sensor can measure. Since the final object is to integrate sensors with microchannels for pressure distribution measurements, the scale of the pressure sensors is very important. If the scale is bigger much big than a microchannel, the number of sensors which can be connected to a microchannel might be not enough to provide very detailed information about microflow.

3. *Microchannel Gas Flow Interruption*

   When attaching pressure sensors to a microchannel, interruptions to gas flow in the channel is unavoidable. Depending upon the design of the pressure sensor, there are several methods to connect a sensor to a microchannel. One should always pick up the one which has minimum effects on the gas flow.

Considering these issues, none of the pressure sensors developed in the past is adequate for the microflow system. Therefore, a new type of surface micromachined pressure sensor which uses silicon nitride as its diaphragm material, polysilicon resistor as its strain gauge and PSG sacrificial layer etching technology is developed. In this chapter, the design, modeling and experiments of pressure sensors will be presented. The issue of using these sensors in the microflow system is discussed in the next chapter.

3.2 Pressure Sensor Design

3.2.1 Gauge Factor and Piezoresistivity

The gauge factor of a material is defined as the fractional changes in resistance, R, of a material per unit strain, ϵ. That can be expressed as[4], in terms of Poisson's ratio, μ, and resistivity, ρ,

$$\frac{\Delta R}{R\epsilon} = \begin{cases} 1 + \mu_x + \mu_y + \Delta\rho/\rho\epsilon & \text{(longitudinal)} \\ -1 + \mu_x - \mu_l + \Delta\rho/\rho\epsilon & \text{(transverse)} \end{cases} \tag{3.1}$$

where x, y and l represent the two axes perpendicular to the current flow and the axis parallel to the flow.

A piezoresistive material will change its resistivity if a strain is applied on it. Analogs to the stress which can be fully described by a 3×3 symmetrical tensor (with only 6 independent variables), the change of the resistivity, Δ, can also described by a third order tensor. A certain relationship exists between the stress tensor and the tensor of the change of resistivity, Δ. If the second order effect is ignored, the two tensors are related linearly as

$$[\Delta] = [\Pi][T] \tag{3.2}$$

where the tensor $[\Pi]$ is called piezoresistance tensor which is a 6×6 matrix. For cubic type single crystal material such as silicon and germanium, the matrix of the piezoresistance tensor based on principal axes is

$$\Pi = \begin{bmatrix} \pi_{11} & \pi_{12} & \pi_{12} & 0 & 0 & 0 \\ \pi_{12} & \pi_{11} & \pi_{12} & 0 & 0 & 0 \\ \pi_{12} & \pi_{12} & \pi_{11} & 0 & 0 & 0 \\ 0 & 0 & 0 & \pi_{44} & 0 & 0 \\ 0 & 0 & 0 & 0 & \pi_{44} & 0 \\ 0 & 0 & 0 & 0 & 0 & \pi_{44} \end{bmatrix} \tag{3.3}$$

As can be seen, it needs only three coefficients, π_1, π_{12} and π_{44} to describe the piezoresistivity of the single crystal silicon. However, all 36 of the coefficients may be nonzero when referred to a Cartesian system of arbitrary orientation relative to the crystallographic

axes. For example, in a coordinate system (x', y', z') which is related to the principal axes system through

$$\begin{bmatrix} x' \\ y' \\ z' \end{bmatrix} = \begin{bmatrix} l_1 & m_1 & n_1 \\ l_2 & m_2 & n_2 \\ l_3 & m_3 & n_3 \end{bmatrix} \begin{bmatrix} x \\ y \\ z \end{bmatrix}, \tag{3.4}$$

where the direction cosines l_i, m_i and n_i are defined as

$$\begin{bmatrix} l_1 & m_1 & n_1 \\ l_2 & m_2 & n_2 \\ l_3 & m_3 & n_3 \end{bmatrix} = \begin{bmatrix} c\phi c\theta c\psi - s\phi c\psi & s\phi c\theta c\psi + c\phi s\psi & -s\theta c\psi \\ -c\phi c\theta s\psi - s\phi c\psi & -s\phi c\theta s\psi + c\phi c\psi & s\theta s\psi \\ c\phi s\theta & s\phi c\theta & c\theta \end{bmatrix} \tag{3.5}$$

in which $c\phi$ stands for $\cos\phi$ and $s\psi$ stands for $\sin\psi$, etc., the piezoresistance coefficients, π'_{11} and π'_{12}, can be calculated by

$$\pi'_{11} = \pi_{11} - 2(\pi_{11} - \pi_{12} - \pi_{44})(l_1^2 m_1^2 + l_1^2 n_1^2 + m_1^2 n_1^2) \tag{3.6}$$

$$\pi'_{12} = \pi_{12} + (\pi_{11} - \pi_{12} - \pi_{44})(l_1^2 l_2^2 + m_1^2 m_2^2 + n_1^2 n_2^2) \tag{3.7}$$

Analogs to the piezoresistance coefficients, the compliance coefficients, S_{ij}, which relate the strain and the stress in a single crystal material can be calculated by

$$S'_{ii} = S_{11} + (S_{44} + 2S_{12} - 2S_{11})(l_i^2 m_i^2 + l_i^2 n_i^2 + m_i^2 n_i^2) \tag{3.8}$$

$$S'_{ij} = S_{12} + (S_{11} - S_{12} - \frac{1}{2}S_{44})(l_i^2 l_j^2 + m_i^2 m_j^2 + n_i^2 n_j^2) \tag{3.9}$$

The gauge factor at an arbitrary direction is defined as[4]

$$G = 1 - \sum \frac{S_{ij}}{S_{ii}}(1 - \delta_{ij}) + \frac{\pi_l}{S_{ii}} \tag{3.10}$$

3.2.2 Polysilicon Strain Gauge

The electrical properties of polysilicon can be described by means of the "carrier-trapping model" originally proposed by Kamins[5], Rai-Choudhury and Hower[6] and Seto[7]. This model starts from the assumption that the grain boundaries comprise a large number of traps and that the doping atoms are uniformly distributed and ionized. The initially electrically neutral traps are charged through the trapping of free carries at the grain boundaries, and the effective carrier density is reduced. For neutrality reasons, depletion regions occur in the

adjacent crystal grains. This results in potential barriers formed at the grain boundaries. Fig. 3.1 shows the one-dimensional structure of polysilicon and band diagram of the "carrier-trapping model".

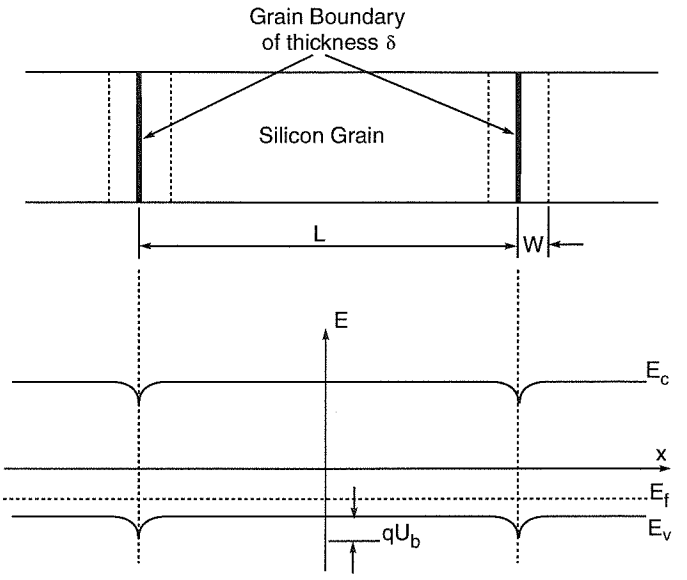

Figure 3.1: Carrier-trapping model: (a)one-dimensional grain structure; (b) energy band diagram for p-type polysilicon.

According to this model, the polysilicon resistivity can be expressed as

$$\rho = \rho_g \frac{[L-(2w+\delta)]}{L} + \rho_b \frac{(2w+\delta)}{L} \tag{3.11}$$

where ρ_g and ρ_b are resistivities of the grain and the barrier respectively. L is the length of the grain, w is the width of the depletion region, δ is the thickness of the grain boundary. Thus, the change in resistivity induced by the strain can be found using the following formula

$$\frac{\Delta\rho}{\epsilon} = \frac{[L-(2w+\delta)]}{L}\frac{\Delta\rho_g}{\epsilon} + \frac{(2w+\delta)}{L}\frac{\Delta\rho_b}{\epsilon} \tag{3.12}$$

For a single grain which can be considered as a single crystal silicon, the gauge factor can be obtained by combining the Eq. (3.12) and (3.10) which leads to

$$G = 1 - \sum_j \frac{S'_{ij}}{S'_{ii}}(1-\delta_{ij}) + \frac{\rho_g \pi_{lg}}{[\rho_g + (2w+\delta)\rho_b/[L-(2w+\delta)]]S'_{ii}}$$

$$+\frac{\rho_b \pi_{lb}}{[\rho_b + [L-(2w+\delta)]\rho_g/(2w+\delta)]S'_{ii}} \tag{3.13}$$

where π_{lg} and π_{lb} are the longitudinal piezoresistive coefficients of the grain and barrier respectively. Both π_{lg} and π_{lb} incorporate high doping level effects.

Depending upon the deposition conditions and the thermal history, polysilicon film may or may not show a preferential texture in the directional distribution of the single crystal grain. However, for the reason of simplicity, it is assumed that the orientation distribution of the silicon grain in the polysilicon film is random. Thus by averaging the expression (3.13), the gauge factor of a polysilicon film is

$$G = 1 - 2\left\langle \frac{S'_{ij}}{S'_{ii}} \right\rangle + \left\langle \frac{R_1 \pi_{lg}}{S'_{ii}} + \frac{R_2 \pi_{lb}}{S'_{ii}} \right\rangle \tag{3.14}$$

where

$$R_1 = \frac{\rho_g}{\rho_g + (2w+\delta)\rho_b/[L-(2w+\delta)]} \tag{3.15}$$

$$R_2 = \frac{\rho_b}{\rho_b + [L-(2w+\delta)]\rho_g/(2w+\delta)} \tag{3.16}$$

and

$$\left\langle \frac{S'_{ij}}{S'_{ii}} \right\rangle = \int_{\theta=0}^{\pi/2}\int_{\phi=0}^{\pi/4} \left(\frac{S'_{ij}}{S'_{ii}}\right)\Big|_{\psi=0} d\theta d\phi \Big/ \int_{\theta=0}^{\pi/2}\int_{\phi=0}^{\pi/4} d\theta d\phi \tag{3.17}$$

with a similar equation being used for $\langle (R_1\pi_{lg}/S'_{ii}) + (R_2\pi_{lb}/S'_{ii})\rangle$.

3.2.3 Sensitivity Analysis

Diaphragm Bending and Stress Distribution

Under an assumption which states that the middle plane of a plate remains natural plane (in other words, there is no stress in the middle plane), the deflection of a flat plate under uniform pressure load can be found by solving the fourth-order differential equations as below:

$$\frac{\partial^4 w}{\partial x^4} + 2\frac{\partial^4 w}{\partial x^2 \partial y^2} + \frac{\partial^4 w}{\partial y^4} = \frac{p}{D} \tag{3.18}$$

where $w = f(x, y)$ denotes the displacement of the natural plane from its original position; p is the pressure loading force in the direction of the deflection w; and D denotes a constant

which depends upon the Young's module, E, and poisson's ratio, ν, of the plate material, namely

$$D = \frac{Et^3}{12(1-\nu^2)} \tag{3.19}$$

If the differential equation is solved for w, the strains in the plate can then be calculated using the following expressions:

$$\begin{aligned} \epsilon_x &= -z\frac{\partial^2 w}{\partial x^2} \\ \epsilon_y &= -z\frac{\partial^2 w}{\partial y^2} \\ \gamma_{xy} &= 2z\frac{\partial^2 w}{\partial x \partial y} \end{aligned} \tag{3.20}$$

Once the strain distribution is known, the stress in the plate can be calculated using the following formula:

$$\begin{aligned} \sigma_x &= \frac{E}{1-\nu^2}(\epsilon_x + \nu\epsilon_y) \\ \sigma_y &= \frac{E}{1-\nu^2}(\epsilon_y + \nu\epsilon_x) \\ \tau_{xy} &= G\gamma_{xy} = \frac{E}{2(1+\nu)}\gamma_{xy} \end{aligned} \tag{3.21}$$

For the case of a thin plate under uniform pressure load, if all edges are clamped as stated below,

$$w|_{x=0,a} = 0 \quad \left.\frac{\partial w}{\partial x}\right|_{x=0,a} = 0 \tag{3.22}$$

$$w|_{y=0,b} = 0 \quad \left.\frac{\partial w}{\partial y}\right|_{y=0,b} = 0 \tag{3.23}$$

The differential equation can be solved using fourier series expansion method. The solution is[8]

$$w = \sum_{m=1}^{\infty}\sum_{n=1}^{\infty} a_{mn}\left(1-\cos\frac{2m\pi x}{a}\right)\left(1-\cos\frac{2n\pi y}{b}\right) \tag{3.24}$$

where coefficients, a_{mn}, are determined from the condition that the potential energy of the system

$$\mathbf{\Pi} = \mathbf{U} - \mathbf{W} \tag{3.25}$$

is a minimum with respect to a_{mn}. The bending-strain energy can be calculated using

$$\mathbf{U} = \frac{D}{2}\iint\left(\frac{\partial^2 w}{\partial x^2} + \frac{\partial^2 w}{\partial y^2}\right)^2 dxdy \tag{3.26}$$

and the potential energy of the external force is

$$\mathbf{W} = \iint pwdxdy \tag{3.27}$$

The condition of minimum potential energy

$$\frac{\partial \mathbf{\Pi}}{\partial a_{mn}} = 0 \tag{3.28}$$

therefore gives

$$\begin{aligned} 4D\pi^4 ab \Bigg\{ \left[3\left(\frac{m^4}{a^4}\right) + 3\left(\frac{n^4}{b^4}\right) + 2\left(\frac{m^2}{a^2}\right)\left(\frac{n^2}{b^2}\right) \right] a_{mn} \\ + \sum_{r=1, r\neq n}^{\infty} 2\left(\frac{m^4}{a^4}\right) a_{mr} + \sum_{r=1, r\neq m}^{\infty} 2\left(\frac{n^4}{b^4}\right) a_{rn} \Bigg\} - pab \;=\; 0 \end{aligned} \tag{3.29}$$

It would be accurate enough for us to just consider the case $m, n = 1, 2, 3$. For a square plate ($a = b$), the solutions to equations (3.29) are

$$\begin{aligned} a_{11} &= 0.11774p' \quad a_{12} = a_{21} = 0.01184p' \\ a_{22} &= 0.00189p' \quad a_{13} = a_{31} = 0.00268p' \\ a_{33} &= 0.00020p' \end{aligned} \tag{3.30}$$

where $p' = pa^4/4D\pi^4$. Correspondingly, the strain at the surface of the plate (diaphragm of a pressure sensor) is

$$\epsilon_x(x, y) = -\frac{4\pi^2 t}{a^2} \sum_{m=1}^{\infty} \sum_{n=1}^{\infty} a_{mn} m^2 \cos\left(\frac{2\pi m x}{a}\right) \left[1 - \cos\left(\frac{2\pi n y}{a}\right)\right] \tag{3.31}$$

By interchanging x and y, one can easily find $\epsilon_y(x, y)$. The stress on the surface of the plate is

$$\begin{aligned} \sigma_x(x, y) \;=\; & -\frac{4\pi^2 t}{a^2} \frac{E}{1-\nu^2} \sum_{m=1}^{\infty} \sum_{n=1}^{\infty} a_{nm} \left[m^2 \cos\left(\frac{2m\pi x}{a}\right) + \nu n^2 \cos\left(\frac{2n\pi y}{a}\right) \right. \\ & \left. -(m^2 + \nu n^2) \cos\left(\frac{2m\pi x}{a}\right) \cos\left(\frac{2n\pi y}{a}\right) \right] \end{aligned} \tag{3.32}$$

Fig. 3.2(a) shows the normalized diaphragm deflection under uniform pressure loading. Fig. 3.2(b) shows the normalized strain (x-direction) distribution. Noticed, the strain changes direction from the center of the plate to the edge. Because of this, some polysilicon strain gauges are placed around the center, and some are placed on the edges. So when the

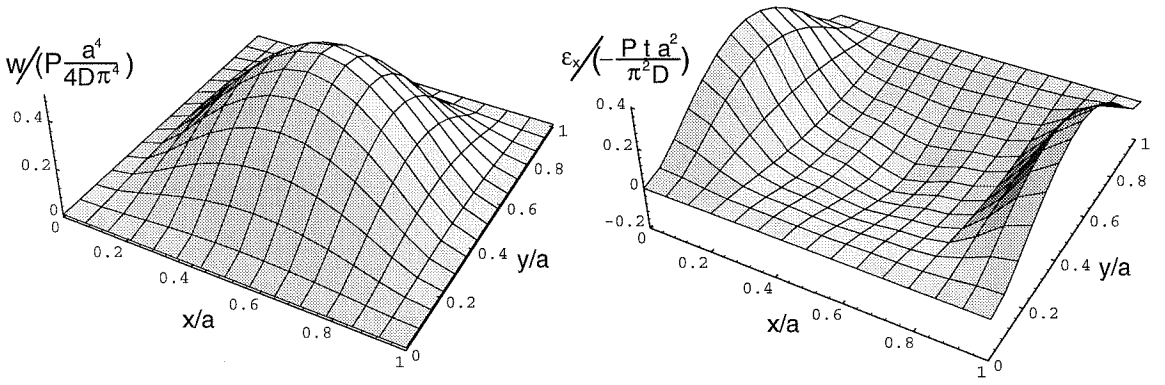

Figure 3.2: (a) The bending of a plate under uniform pressure loading. (b) The normalized strain distribution, $\epsilon_x(x,y)/\left(-\frac{Pta^2}{\pi^2 D}\right)$.

plate bends under the loading pressure, resistances of the gauges on the center change in opposite directions as those of the gauges on the edges. Thus a full Wheatstone bridge can be made out of the isotropic polysilicon material.

Strain Gauge Placement and Sensitivity Optimization

With known strain distribution in the bending plate (diaphragm of the pressure sensors), the sensitivity of the pressure sensors can be optimized by placing the polysilicon strain gauges at the places where the maximum strain is located (Fig. 3.2). Since the vertical strain component is much larger than the transverse (parallel to the edge), for example, $\epsilon_x \gg epsilon_y$ at $(x = 0or1; y = 0.5)$, the strain gauges should be vertically placed on the center of the edge. As one can see from Fig. 3.2, the strain is very non-uniform over the diaphragm. The measured strain by the strain gauge is averaged over the area it covers. The average strain for a gauge placed vertically at the center of an edge can be calculated with

$$\langle \epsilon_x \rangle = \frac{1}{l} \int_0^l \epsilon_x(x,y)|_{y=0.5a}\, dx \tag{3.33}$$

where $l = \int dx$ is the length of the polysilicon strain gauge. The average strain for gauges placed at the center of the diaphragm can be similarly calculated. Fig. 3.3 shows the averaging effect. As one can see, the effective strain, $< \epsilon_l >$, is reduced by as much as 25%

($< \epsilon_l >= 0.75\epsilon_{max}$) if the length of the strain gauge is 10% of the diaphragm size, $l = 0.1a$.

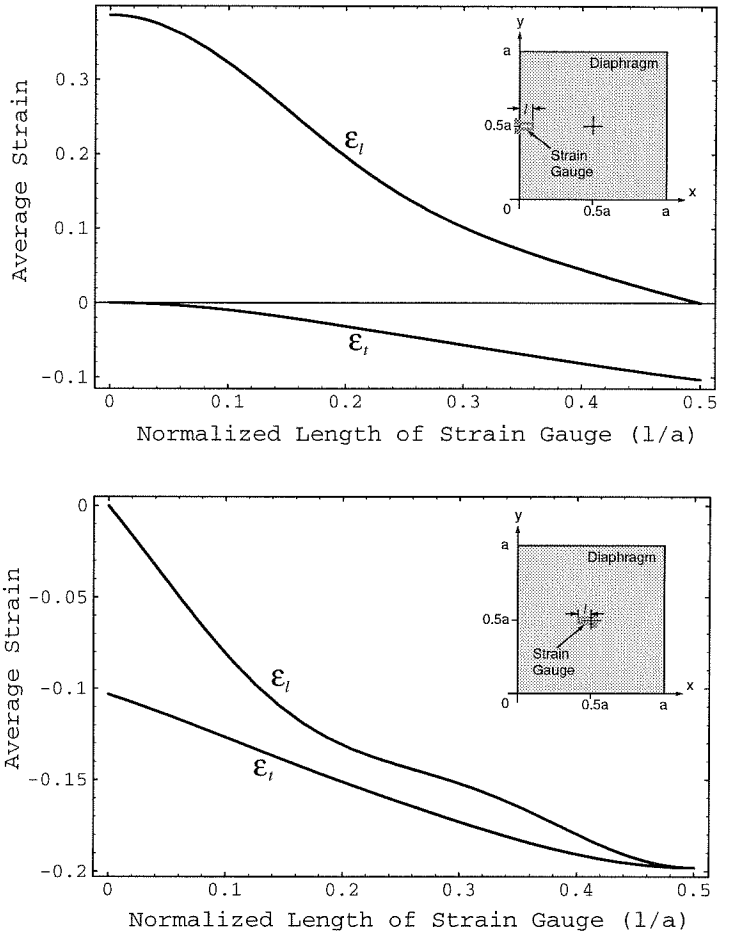

Figure 3.3: The averaged strain (longitudinal $< \epsilon_l >$ and transverse $< \epsilon_t >$) as a function of the length of the strain gauge (l/a). (a) The strain gauge is placed at the edge. (b) The strain gauge is placed at the center.

Thus the size of the gauge should be made as small as possible. However, the size of the gauge is limited by several factors; one is the photolithography capability of the fabrication; the other is the total resistance of the gauge required for the electrical measurements. Furthermore, a negative effect of reducing gauge size is the resistance mismatch of the Wheatstone bridge becomes more pronounced.

Fig. 3.4 shows a designed polysilicon strain gauge which is simply a heavily doped polysilicon resistor[9]. The gauge is used in the pressure sensors on the microflow measure-

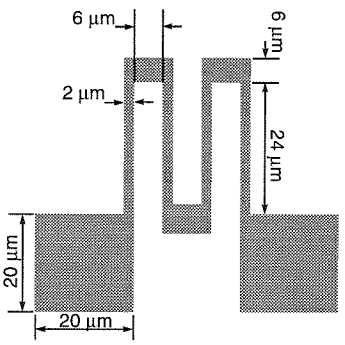

Figure 3.4: Design parameters of the polysilicon resistor used as pressure sensors gauge.

ment system. The size of the pressure sensors diaphragm is 250×250 μm^2. The length of the gauge is 24 μm ($l/a \sim 10\%$). For a sheet resistance of about 50 $\Omega/\square$, the total resistance of the gauge is about 50□×50 $\Omega/\square$=2.5 KΩ.

The relative change of resistance can be calculated using

$$\frac{\Delta R}{R} = G_l \langle \epsilon_l \rangle + G_t \langle \epsilon_t \rangle \tag{3.34}$$

where the subscript l and t represent the longitudinal and transverse direction. The averaged strain, $< \epsilon_l >$ and $< \epsilon_t >$, for gauges at the edge and center of a square diaphragm are shown in Fig. 3.3. Once the gauge factors for polysilicon are known, the sensitivity of the pressure sensor can then be estimated with the following formula:

$$S = \frac{\Delta R}{R} \frac{1}{p} \tag{3.35}$$

where p is the pressure.

3.2.4 Pressure Sensor Design and Modeling

Pressure Sensor Design and Fabrication

The pressure sensor integrated into the microflow measurement system utilize a silicon nitride film as its diaphragm material. The chamber is formed by etching away a sacrificial layer underneath the diaphragm. A deposited polysilicon film is patterned as the piezoresistor for strain measurement. A cross-sectional diagram of the sensor can be seen in Fig. 3.5.

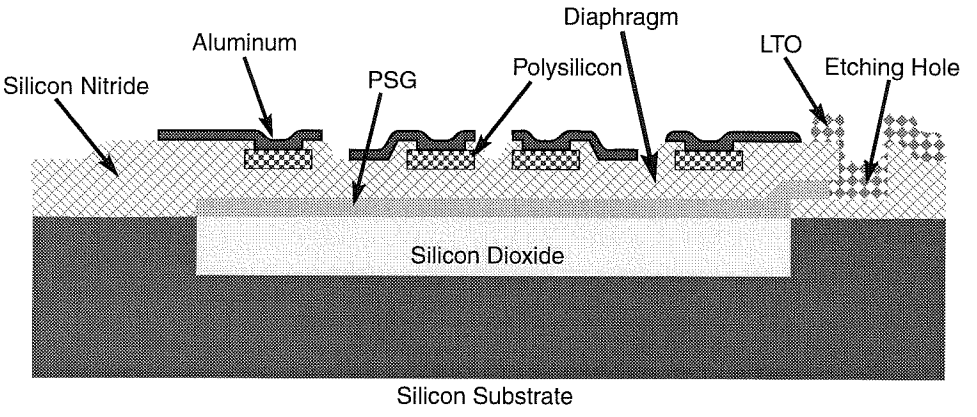

Figure 3.5: Schematics of the cross section of the pressure sensor.

On a 250×250 μm^2silicon nitride diaphragm, there are four polysilicon resistors placed around the center and another four are placed on the edge of the diaphragm. The thickness of the diaphragm is total 1.5 micron thick which consists of two layers of low intrinsic stress silicon nitride, $Si_3N_{3.6}$). Polysilicon resistors are buried inside the diaphragm. The thickness of the polysilicon resistors is 500 nm. The sheet resistance of the heavily doped polysilicon film is in the range of 50-150 $\Omega/\square$. Underneath the diaphragm is a 250×250×1.2 μm^3 chamber. Fig. 3.6(a) shows a photography of the sensor. Evaporated aluminum film is used to form good ohmic contact to the heavily doped p type polysilicon. The polysilicon resistors are connected to form a Wheatstone bridge for temperature compensation although the heavily doped polysilicon shows very small temperature coefficient.

Table 3.1 is a typical fabrication flowchart for a surface micromachined pressure sensor which is abstracted from the fabrication process of a microflow measurement system. The whole fabrication process will be discussed in detail in Chapter 4.

Pressure Sensor Modeling

The photography of a pressure sensor and its circuit model are shown in Fig. 3.6. Let $R_1 = R_{c1} + R_{c2}$, $R_2 = R_{e3} + R_{e4}$, $R_3 = R_{c3} + R_{c4}$ and $R_4 = R_{e1} + R_{e2}$ (Fig. 3.6(b)), then

Table 3.1: Flowchart for Pressure Sensor Fabrication

1	Wafer cleaning.
2	Deposit thin low-stress silicon nitride (Chapter 2).
3	Pattern silicon nitride (the chamber area of sensors).
4	Etch silicon down 600 nm.
5	Grow silicon dioxide 1.0 nm (sacrificial layer).
6	Deposit LPCVD PSG 300 nm.
7	Pattern PSG (sacrificial layer).
8	Deposit thick low-stress silicon nitride 1.0 μm (sensor diaphragm).
9	Deposit 500 nm polysilicon film.
10	Pattern polysilicon (the resistors).
11	Deposit another low-stress silicon nitride.
12	Pattern etching holes.
13	Perform sacrificial layer etching with concentrated HF 49 wt.%.
14	Deposit thick LTO to seal the etching holes (1.0 μm).
15	Pattern the LTO layer.
16	Pattern the contact windows.
17	Evaporate 1.0 μm thick Aluminum.
18	Pattern the metal.
19	Sinter contacts.

the differential output voltage from the Wheatstone bridge can be calculated using

$$\begin{aligned}\left(\frac{v}{V}\right)_{p=0} &= \Delta V = V_1 - V_2 \\ &= \frac{R_1R_3 - R_2R_4}{(R_1+R_4)(R_2+R_3)}\end{aligned} \tag{3.36}$$

where V is the bias voltage applied to the bridge; v is the DC offset voltage; subscript $p = 0$ denotes the condition of zero gauge pressure. Ideally, this DC offset voltage is zero if the Wheatstone bridge is balanced (when condition $R_1R_3 = R_2R_4$ is satisfied). However, in reality, this condition is never satisfied. So the DC offset voltage, v, is in general not zero. Suppose a pressure, p, is applied to the sensor, then each polysilicon resistor suffers an external strain due to the bending of the diaphragm. Thus each resistor changes its resistance from R_i to $R_i + \delta R_i$ according to the magnitude of the strain. The new DC voltage from the differential output of the Wheatstone bridge is then

$$\begin{aligned}\left(\frac{v}{V}\right)_p &= \frac{(R_1+\delta R_1)(R_3+\delta R_3) - (R_2+\delta R_2)(R_4+\delta R_4)}{(R_1+R_4+\delta R_1+\delta R_4)(R_2+R_3+\delta R_2+\delta R_3)} \\ &= \left(\frac{v}{V}\right)_{p=0} + \frac{1}{(R_1+R_4)(R_2+R_3)}\left[R_1R_3\left(\frac{\delta R_1}{R_1}+\frac{\delta R_3}{R_3}\right) - R_2R_4\left(\frac{\delta R_2}{R_2}+\frac{\delta R_4}{R_4}\right)\right]\end{aligned}$$

$$-\left(\frac{v}{V}\right)_{p=0}\left(\frac{\delta R_1+\delta R_4}{R_1+R_4}+\frac{\delta R_2+\delta R_3}{R_2+R_3}\right)+O\left(\left(\frac{\delta R}{R}\right)^2\right) \tag{3.37}$$

Even the zero pressure offset voltage does not vanish; it is usually much smaller than the DC bias voltage. In other words, $\left(\frac{v}{V}\right)\big|_{p=0} \ll 1$. Thus, the third term in Eq. (3.37), comparing with the second term, can be neglected. Finally, after neglecting the second order effect, the output of the Wheatstone bridge can be written as

$$\left(\frac{v}{V}\right)_p=\left(\frac{v}{V}\right)_{p=0}+\frac{1}{(R_1+R_4)(R_2+R_3)}\left[R_1R_3\left(\frac{\delta R_1}{R_1}+\frac{\delta R_3}{R_3}\right)-R_2R_4\left(\frac{\delta R_2}{R_2}+\frac{\delta R_4}{R_4}\right)\right] \tag{3.38}$$

For a balanced Wheatstone bridge with condition $R_1 = R_2 = R_3 = R_4$, the Eq. (3.38) can be further simplified as

$$\left(\frac{v}{V}\right)_p=\frac{1}{4}\left[\left(\frac{\delta R_1}{R_1}+\frac{\delta R_3}{R_3}\right)-\left(\frac{\delta R_2}{R_2}+\frac{\delta R_4}{R_4}\right)\right] \tag{3.39}$$

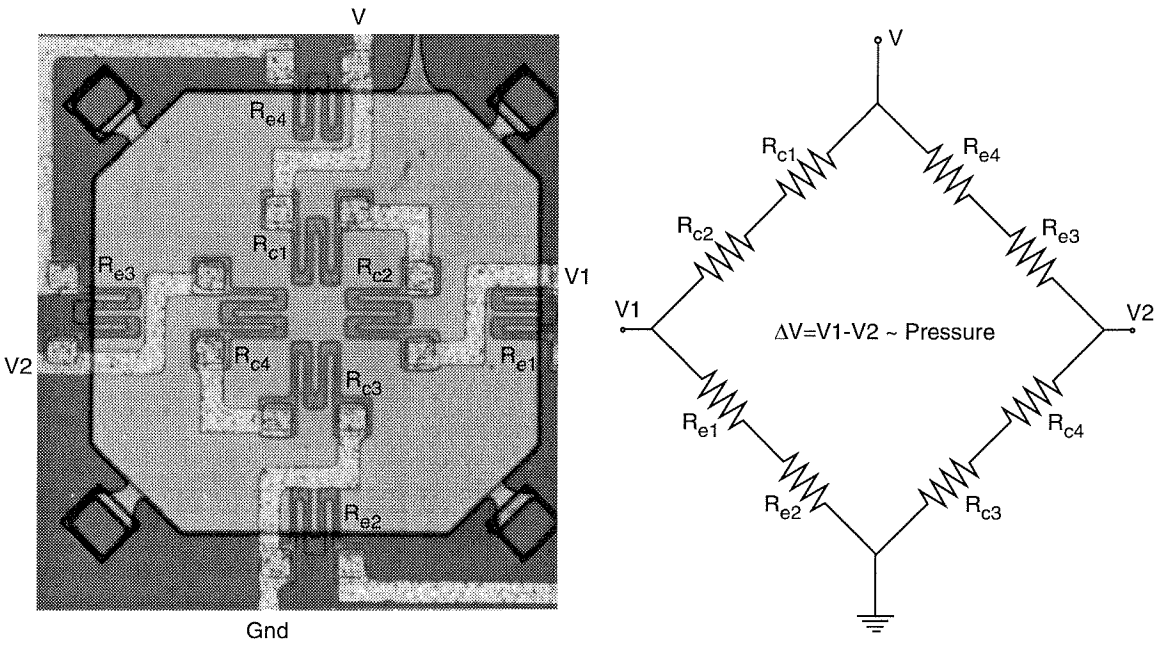

Figure 3.6: The designed pressure sensor for microflow measurement system.

Eq. (3.34) says the relative change of resistance depends only upon the gauge factor and averaged strain applied on the resistor. Since the symmetrical placement of the resistors

around the edge and center of the diaphragm, the following relations exist:

$$\left(\frac{\delta R}{R}\right)_c = \left(\frac{\delta R_1}{R_1}\right) = \left(\frac{\delta R_3}{R_3}\right) = G_l \langle \epsilon_l \rangle_e + G_t \langle \epsilon_t \rangle_e \tag{3.40}$$

$$\left(\frac{\delta R}{R}\right)_e = \left(\frac{\delta R_2}{R_2}\right) = \left(\frac{\delta R_4}{R_4}\right) = G_l \langle \epsilon_l \rangle_c + G_t \langle \epsilon_t \rangle_c \tag{3.41}$$

where subscript c and e denote the parameters are calculated at the edge and center of the diaphragm respectively. With these relations, Eq. (3.39) now becomes

$$\left(\frac{v}{V}\right)_p = \frac{1}{2}\left[G_l(\langle \epsilon_l \rangle_e - \langle \epsilon_l \rangle_c) + G_t(\langle \epsilon_t \rangle_e - \langle \epsilon_t \rangle_c)\right] \tag{3.42}$$

The sensitivity of the pressure sensor is

$$S = \frac{1}{p}\left[\left(\frac{v}{V}\right)_p - \left(\frac{v}{V}\right)_{p=0}\right] \tag{3.43}$$

Fig. 3.7 shows the sensitivity as function of diaphragm aspect ratio, a/t, for gauge factors 10 and 20. The measured average sensitivity for sensors from the first generation microflow system chip is also shown in the figure as a circle. The aspect ratio of real pressure sensors is about $\frac{250}{1.5} \sim 170$. As one can see, the measured sensitivity is very close to the designed value (targeted at 150-200 μV/V·psi).

Effects of Some Non-ideal Conditions

So far, all the analysis and modeling for pressure sensors are based upon some assumptions which might not be satisfied in practical situations. These 'non-ideal' conditions deserve some more discussion here.

Intrinsic Stress The previous analysis of bending a silicon nitride diaphragm is based on an assumption that there is no build-in stress (intrinsic stress) in the diaphragm. However, the presence of intrinsic stress in the practical structures is almost unavoidable and sometimes preferred. Its effects on sensitivity of a bulk micromachined pressure sensor has been discussed by Chau et al.[10]. For pressure sensors with silicon nitride diaphragm (isotropic material), the stress effects is also isotropic. Here, a circular diaphragm is considered since mathematically it is easier than a square diaphragm and sufficient to illustrate the intrinsic

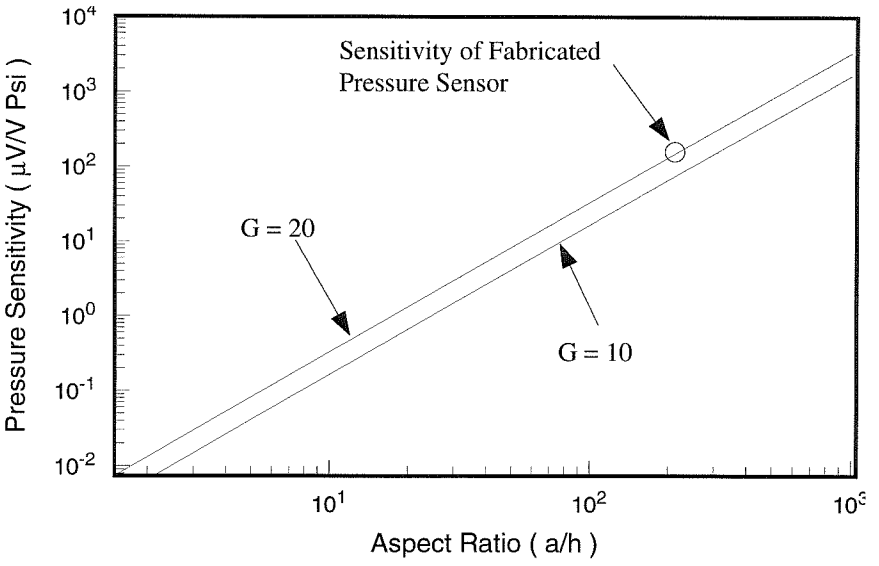

Figure 3.7: The pressure sensors sensitivity calculated from a simpe model and comparision with the experimental results. (Sensor is from the first generation microsystem chip with a gauge factor of about 20.)

stress effect. As shown by Chau et al., the normalized center deflection of the diaphragm, w_c' (deflection with intrinsic stress divided by stress-free deflection), is given by

$$w_c' = \frac{16[2 - 2I_0(k) + kI_1(k)]}{k^3 I_1(k)} \tag{3.44}$$

where I_n is the modified Bessel function of the first kind of order n; and

$$k^2 = \frac{12(1-\nu^2)\sigma_i a^2}{Eh^2} \tag{3.45}$$

in which σ_i is the intrinsic stress (assumed uniform across the diaphragm).

As one can see, the effect of intrinsic stress on the deflection and therefore the sensitivity of the pressure sensor depends upon σ_i, a and h for a given material. The larger or thinner the diaphragm or intrinsic stress is, the more severe the effect. Fig. 3.8 shows the curve of normalized deflection vs. diaphragm aspect ratio for several intrinsic stress σ_i. As an example, for a diaphragm with 10^8 dyne/cm^2 intrinsic and an aspect ratio of 200, its sensitivity is only about 50% of a stress free diaphragm. Therefore, the intrinsic stress in the silicon nitride diaphragm should be made as small as possible.

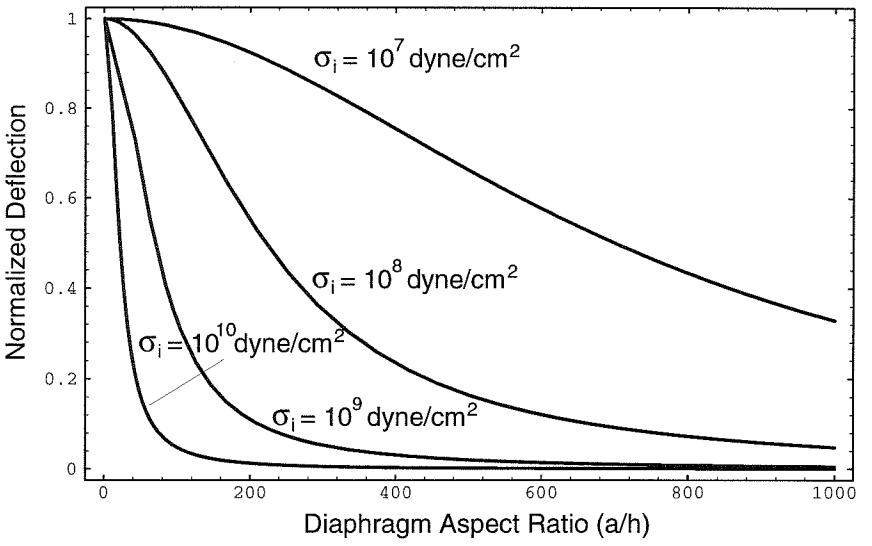

Figure 3.8: Normalized diaphragm center deflection as a function of diaphragm aspect ratio (a/h). The Young's module for silicon nitride is 3.85×10^{12} dyne/cm^2 and the poisson ratio is 0.25.

Buried Strain Gauge As noticed in Fig. 3.5, the polysilicon strain gauges are buried inside the silicon nitride diaphragm. Depending upon their position in the diaphragm, the final sensitivity of the sensor may be seriously different from the previous analysis. While the deflection of the diaphragm is unaffected by the buried gauges (as long as the gauge is small comparing with the diaphragm), the strain now is

$$\epsilon_x^b = -\frac{12(1-\nu^2)p}{\pi^2 E}\left(\frac{2h}{t}\right)\left(\frac{a}{t}\right)^2 g(x,y) = \left(\frac{2h}{t}\right)\epsilon_x^s \tag{3.46}$$

where superscript b and s denote the buried strain gauge and one placed on the surface of the diaphragm. As an example, if t is 1.8 μm and h is 0.4 μm, the strain applied on the gauges in only 44% of the strain on the surface of the diaphragm. So the cover layer of the strain gauges should be deposited as thinly as possible.

Surface Topography There are a total of eight strain gauges buried in the diaphragm of a pressure sensor. These gauges are 500 nm thick each. As results, the thickness of the diaphragm is not uniform and 500 nm high steps are distributed on the surface of the diaphragm at positions where strain gauges are buried. Furthermore, because of the

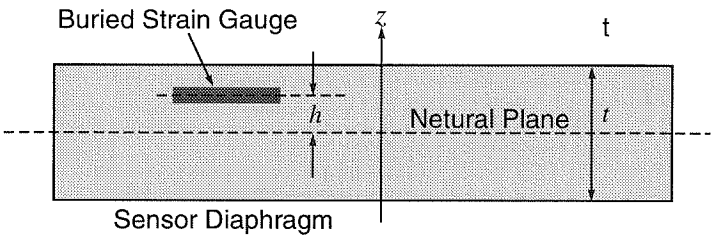

Figure 3.9: Diagram of a buried strain gauge with some conventions.

bird-beak formed during the local-oxidation of the pressure sensor chamber, the edge of the diaphragm is a 300 nm bump. However, it is believed that these structures will cause trivial influence on the behavior of the pressure sensor. As arguments, first, the thickness of the diaphragm is 1.5 μm which is much larger than that of the bump and the strain gauges; second, the strain gauges take less than 5% area of the diaphragm; and finally, Young's modulus of the silicon nitride is much larger than that of the polysilicon (strain gauges). Therefore, the surface topology effects are negligible. Fig. 3.10(a) shows a SEM of the surface of a pressure sensor.

3.3 Experimental Results and Discussion

3.3.1 Experimental Setup

Isolated and Non-isolated Pressure Sensors

Experimental studies of pressure sensors are carried out using integrated microflow system chips. On such a chip, there are two kinds of the pressure sensors: one is the isolated pressure sensor, and the other is connected to the microchannel; therefore, its chamber is opened to the air through inlet/outlet of the microchannel system (Ch. 4).

Fig. 3.11(a) shows an isolated pressure sensor. Its chamber is sealed at low pressure environment. Inside pressure depends upon the sealing process; for example, if used LPCVD LTO, then the chamber pressure is around 150 mtorr. The sensor can be used as an absolute pressure sensor as long as the chamber pressure is lower than the required accuracy for the

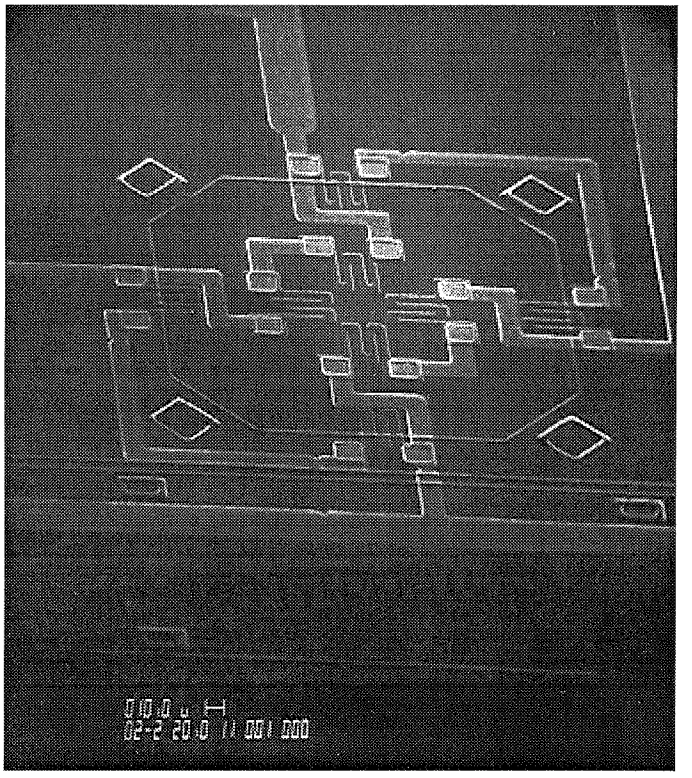

Figure 3.10: SEM picture of a pressure sensor.

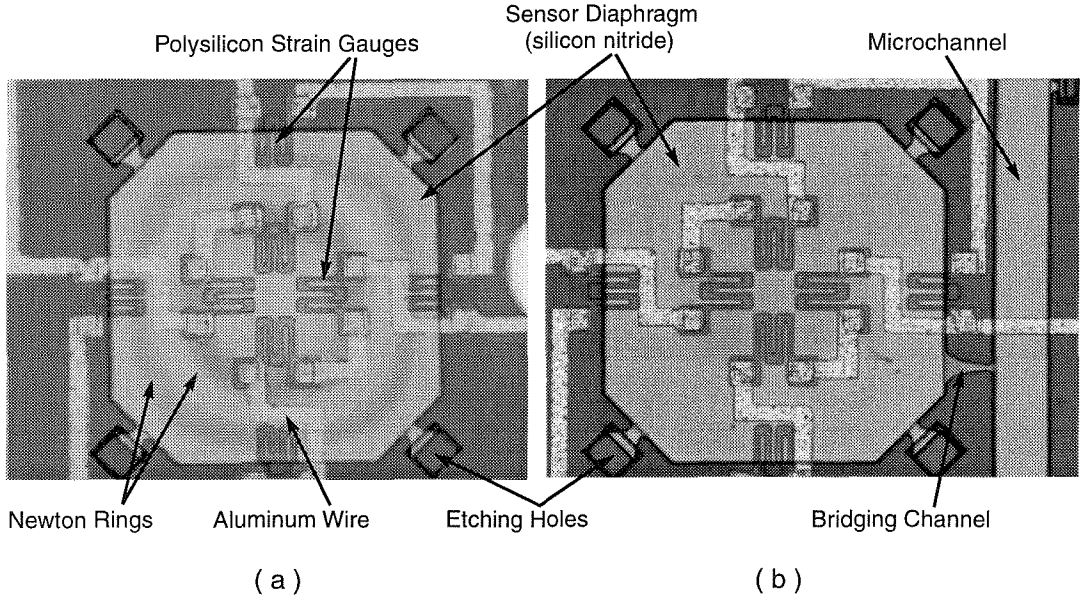

Figure 3.11: Photography of the pressure sensors on a microflow system chip; (a) an isolated pressure sensor; (b) in an integrated microflow measurement system, the sensor is connected to the microchannel through a bridging channel.

measurement. Since the pressure between two sides of the sensor diaphragm is different when the chamber is sealed, the diaphragm is bent. Because of optical reflections between the surface of the bent diaphragm and the bottom of the chamber, one can see newton optical interference rings under a microscope. Such an observation is used for chamber sealing check during the chip fabrication; if there are no newton rings on a supposedly sealed chamber, the sealing process is then unsuccessful. To study the performance, an isolated pressure sensor is encapsulated in a closed container. By varying the pressure inside the container, one can calibrate the pressure sensor with a high accuracy commercial pressure transducer.

Except for these isolated pressure sensors, most sensors on a microflow system chip are connected to the microchannel through a short bridging channel (Fig. 3.11(b)). Since the microchannel is opened to the air at its inlet and outlet (Chapter 4), both sides of the diaphragm of each pressure sensor are under atmosphere pressure. Therefore, no newton rings can be seen. Calibrations of those pressure sensors can be conducted using a special experimental setup which is described in Chapter 5. In principle, first, the chamber of each pressure sensor is pressurized to a desired value; second, output voltage of the sensors is measured with a voltmeter. The pressure inside the chamber of each sensor is measured with a commercial pressure transducer with 0.1% overall accuracy. The gas flows into the chamber of each pressure sensor through the microchannel and bridging channels. Since chamber inside pressure is higher than outside, the diaphragm is bent upward instead of downward as in the calibration of an isolated pressure sensor. Newton rings can still be seen under a microscope. Since there is no protection for over-pressure, the diaphragm of the sensor may break if applied pressure is too high.

AC Drive Method for Pressure Sensors

Usually the pressure sensors are driven using a DC bias voltage. This method has many advantages such as circuit simplicity, easy compensation, etc. However, the measurement accuracy is limited to the noise level of the system. In measuring pressure sensors, the equivalent noise level can be as high as ± 1 psi. Furthermore, in a delicate microflow measurement, the heat conducted from resistors (joule heating effect) to the fluid in the

channel could seriously change the flow pattern. To minimize these two problems, therefore, an AC drive method for pressure sensors is used here.

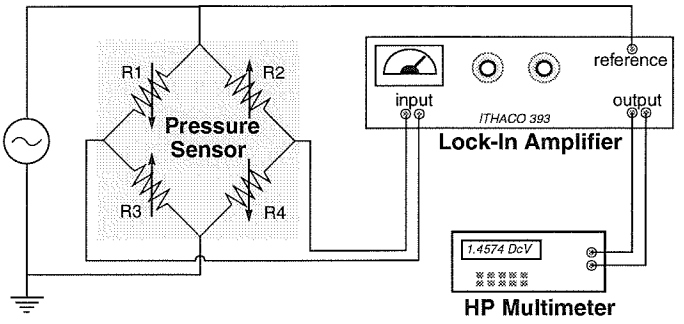

Figure 3.12: Experimental setup for studying pressure sensors using AC drive.

The configuration of the AC drive setup is shown in Fig. 3.12. It consists of an AC signal source, a lock-in amplifier (LIA) and DC voltage meter. The modulated AC signal from the Wheatstone bridge carries the pressure information and is fed into the lock-in amplifier. In the lock-in amplifier, the signal passes an extremely narrow band-pass filter and is then demodulated before being sent out (Fig. 3.13). The DC signal from the lock-in amplifier is proportional to the applied pressure timed the gain of the lock-in amplifier. The advantage of the AC-setup is the output signal has a very high signal-to-noise ratio which allows one to study accurately the second order effect such as nonlinerity and hystersis, etc.

3.3.2 Experimental Results and Discussion

Pressure Sensor Calibrations

Fig. 3.14 shows a calibration curve of an isolated pressure sensor. The curve is measured with a normal DC drive setup. The error bars in the plot represent the fluctuation of the readings. As one can see, the response of a pressure sensor (from -14 to 14 psig) can be modeled with linear function. The slope of the sensor is approximately 120 μV/V·psi. An interesting but expected phenomenon is the saturation of the sensors response when applied pressure is higher than 20 psig. Obviously, this is caused by the diaphragm of the sensor touching the bottom of the chamber. Experiments with many sensors show that the offset

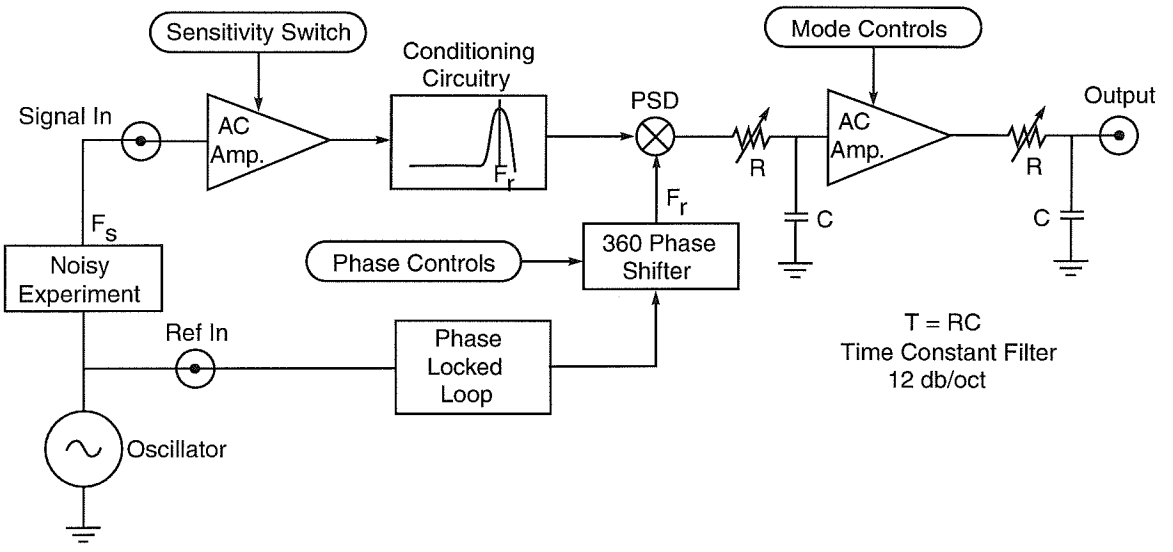

Figure 3.13: Schematic of working principle for a basic single-phase lock-in amplifier.

of the most sensors are in the range from -0.3V to 0.3 V.

Fig. 3.15 shows calibrations of four non-isolated pressure sensors. The average sensitivity of the sensors is about 120 μV/V·psi but individually various about 20% from sensor to sensor. While shown here are sensors only from the first generation of microflow system chip (Chapter 4), the sensors from the second generation chip show an average sensitivity almost two times bigger (245 μV/V·psi). This is mainly due to increased polysilicon gauge factors (from 20 to almost 40). Nevertheless, all the responses show nice linearity to the applied pressure in a range from 0 to 20 psig.

Pressure Response Nonlinearity

To study the second-order effect, the AC drive method is used to minimize any possible inaccuracy in the measurements. The sensor response is modeled with a polynomial function, namely

$$v = v_0 + c_1 p + c_2 p^2 \tag{3.47}$$

where v is the output of the sensor; v_0 is the DC offset. Fig. 3.16 shows a typical calibration of a pressure sensor. The small circle dots in the plot are the measurements. The solid line

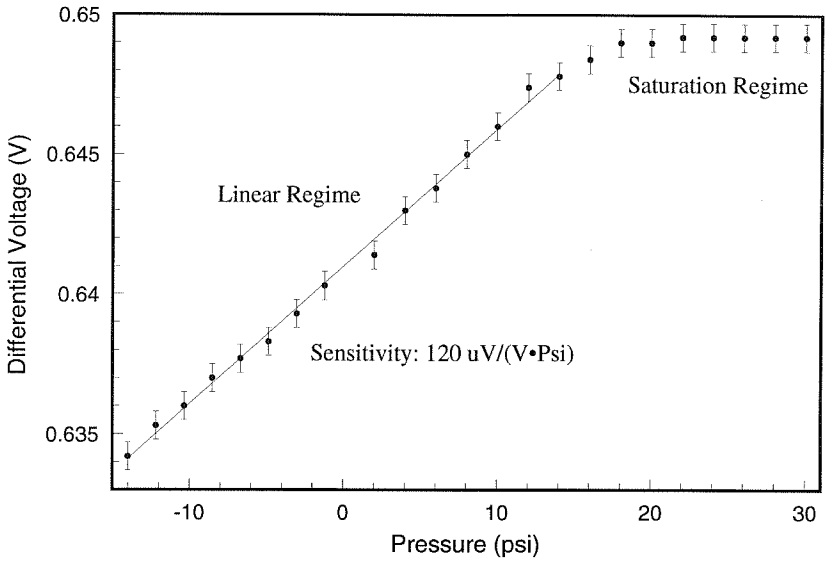

Figure 3.14: The calibration curve for an isolated pressure sensor.

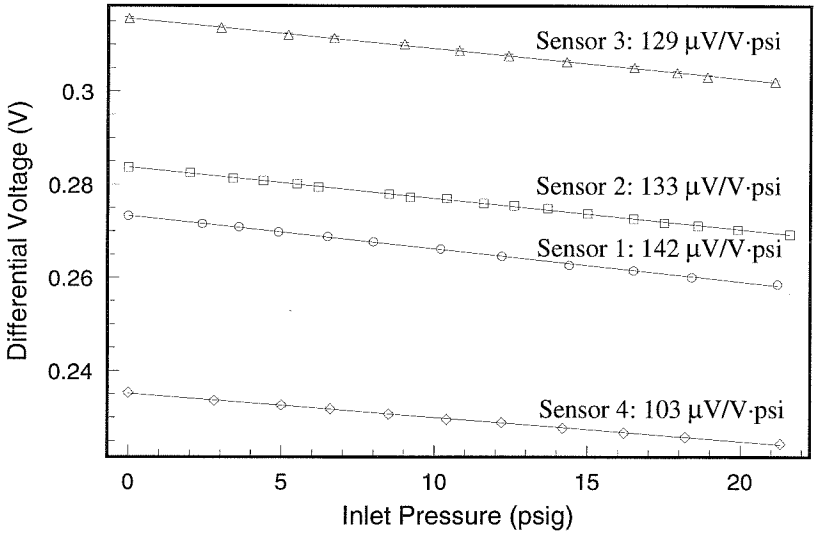

Figure 3.15: The calibrations for four non-isolated pressure sensors (sensors come from the first generation microflow system chip (Chapter 4).

which goes almost perfectly though all the dots is model fitting with a quadratic function (Eq. (3.47)). To study the accuracy of a linear model, a least-square fitting is also performed on the data with a linear function (solid straight line in Fig. 3.16). As can been seen, the difference between a linear and quadratic model is well below 0.5 psi in the range from 3 to 26 psi. The error can be even smaller if the pressure range is less than 30 psi. Thus in a measurement with about 1.0 psi noise level, the error of using a linear model can be neglected. Therefore, the linear response model is used throughout the data analysis of microflow experiments.

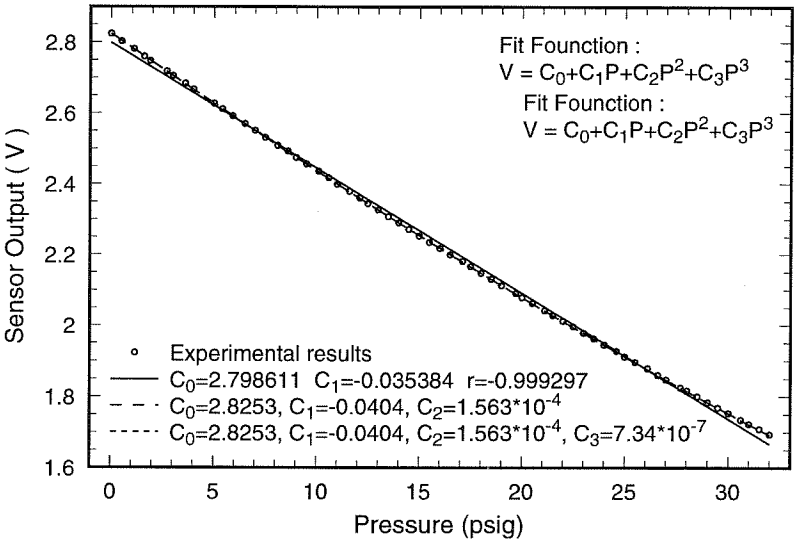

Figure 3.16: Calibration of a typical pressure sensor from the integrated microflow system chip (Chapter 4).

Pressure sensor drift

The drift of the pressure sensors are studied by applying a DC bias voltage on the Wheatstone bridge of the pressure sensors for a long period of time. Periodically the calibration curves for a group of eight pressure sensors are measured.

Fig. 3.17 shows the DC offset voltage drift with 5V bias on the Wheatstone bridge. As one can see, all the pressure sensors show less than several millivolts drift in a ten day

period. Another trend can be noticed from these curves is that initially the DC offset changes very fast, and gradually the drift seems to slow down. The typical time needed to reach a relatively stable condition can be shortened by an aging process; apply a much higher bias voltage (usually 35V, depends on the maximum current limit of the aluminum wires on the chip) to the pressure sensors for a certain time (typically, 10-30 minutes). After the process, the DC drifts of all the pressure sensors drop to below 1 mV/day. Thus, if calibrations of sensors are performed before and after each experiment, the DC drift effect is negligible.

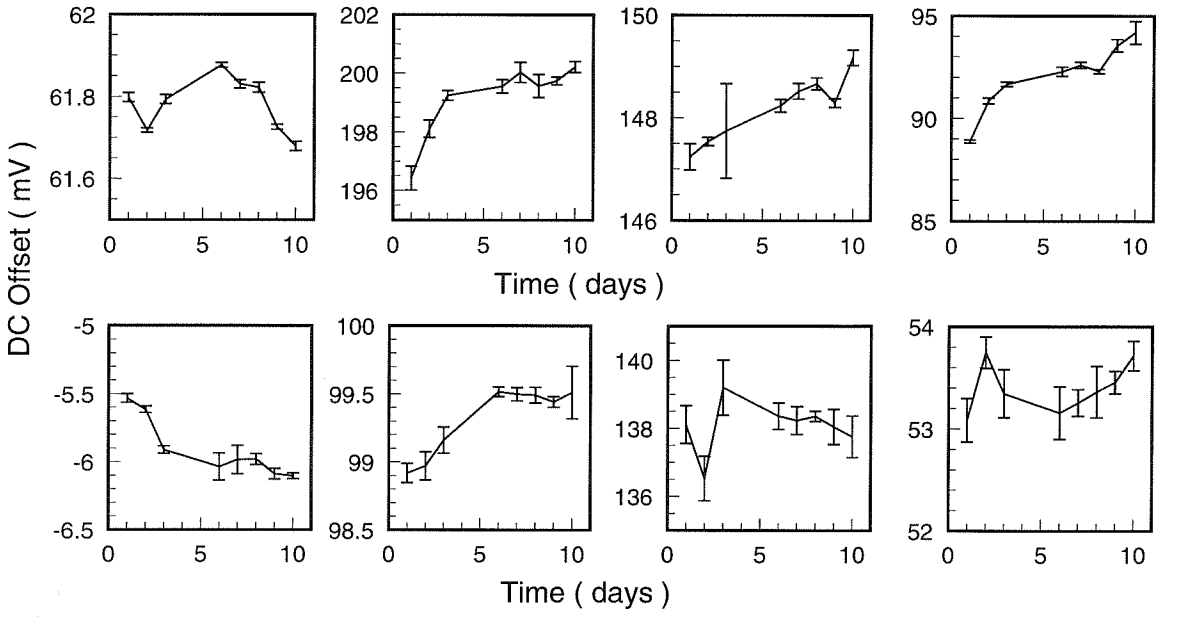

Figure 3.17: DC drift of the pressure sensors.

Temperature Sensitivity

Temperature Effect on Polysilicon Resistance The temperature coefficient of the resistance, so called TCR, is defined as

$$TCR(T) = \frac{1}{R(T)} \frac{dR(T)}{dT} \tag{3.48}$$

where T represents the temperature.

One purpose of using Wheatstone bridge configuration in the design of the pressure sensor is to minimize the temperature sensitivity. Unfortunately, a fabricated pressure sensor always shows DC offset. Therefore, pressure measurements will still be affected by the temperature variation. However, since the polysilicon used for strain gauges is heavily doped (10^{20} cm^{-3}), temperature coefficient is usually less than 0.1%/°C. Fig. 3.18 shows the measured polysilicon resistance and TCR as a function of doping level.

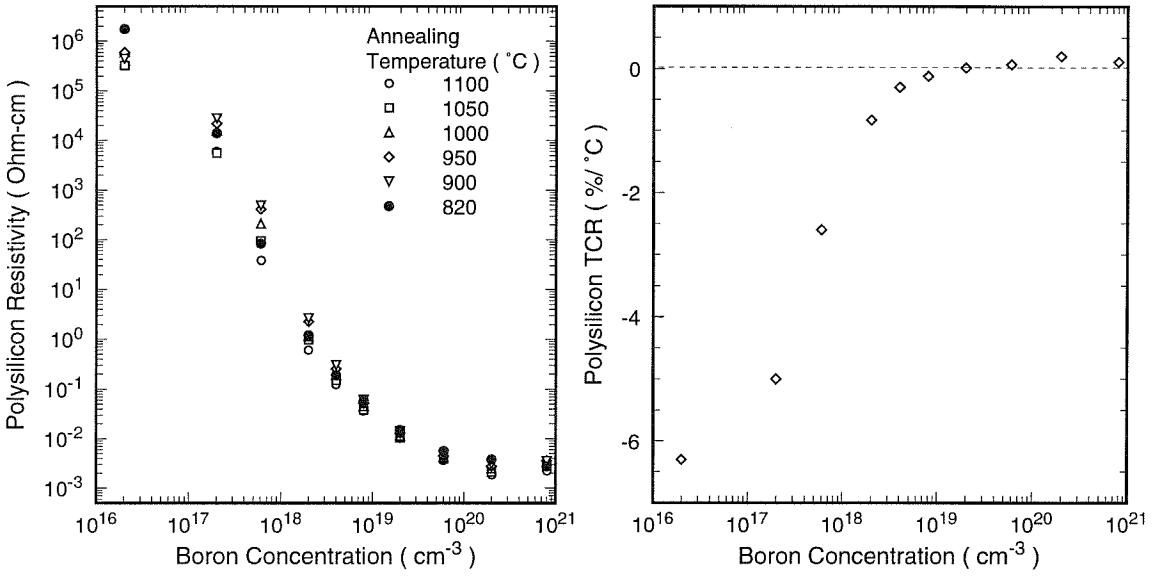

Figure 3.18: Polysilicon resistivity and temperature coefficient as function of doping concentration.

The DC offset of a Wheatstone bridge can be calculated using Eq. (3.36). Assume the polysilicon resistance change linearly with temperature, for example, $R = R_0(1 + CT)$, where C is the temperature coefficient of the resistance. Then, to the first order of the approximation, the change of DC offset voltage can be estimated by

$$\Delta_{drift} = 2C\frac{\Delta V}{V} \tag{3.49}$$

where Δ_{drift} stands for the DC offset drift caused by temperature change. For the pressure sensors in the second generation integrated microflow system, a typical DC offset is about 0.2 V for 5V DC bias. With a TCR of about 0.05%/°C for heavily doped polysilicon, the

DC drift is less than 0.004%V/V·°C. That corresponds to 0.2 mV/°C drift while the bridge is biased 5V.

Temperature Effect on Diaphragm Bending Due to the mismatch of thermal expansion coefficients between silicon and silicon nitride, temperature variation can change the stress state in the nitride diaphragm. The total stress in the diaphragm can be calculated with following formula,

$$\sigma_f = \frac{(\alpha_f - \alpha_s)E_f \Delta T}{1 - \nu_f} + \sigma_{if}, \tag{3.50}$$

where α_s and α_f are thermal expansion coefficients of the silicon substrate and silicon nitride film respectively, E_f and ν_f are Young's modulus and Poisson's ratio of the film, and σ_{if} is the intrinsic stress of the film which is dependent upon the process. For example, α_f=0.8×10^{-6} /°C, α_s=2.33×10^{-6}/°C, E_f=3.85×10^{12} dyne/cm^2. For a Poisson's ratio of 0.3, Eq. (3.50) becomes

$$\sigma_f = 8.7 \times 10^6 \Delta T + \sigma_{if} \qquad [\text{dyne/cm}^2] \tag{3.51}$$

Since the intrinsic stress in the film is in the order of 10^8 dyne/cm^2, the temperature effect on the diaphragm can be ignored most of the time.

3.4 Summary

Pressure sensor is the second important device in the integrated microflow system. The fabrication of the surface micromachined pressure sensor is compatible with that of the microchannel described in Chapter 2. The design and modeling of the pressure sensors are presented in detail in this chapter. Experimental results using pressure sensors fabricated with the integrated microflow system are also presented. These sensors have an average sensitivity of 120 μV/V·psi for the first generation and 245 μV/V·psi for the second generation. The response of the sensor can be well modeled with a linear function with less than 0.5 psi error. Some important factors which may affect the sensor's performance are discussed.

Bibliography

[1] O. N. Tufte, P. W. Chapman, and D. Long, "Silicon diffused-element piezoresistive diaphragms," *Journal of Applied Physics*, vol. 33, pp. 3322–3327, November 1962.

[2] J. J. Wortman and L. K. Monteith, "Semiconductor mechanical sensors," *IEEE Trans. Electron Devices*, vol. ED-16, pp. 855–860, 1969.

[3] W. D. Frobenius, A. C. Sanderson, and H. C. Nathanson, "A microminiature solid-state capacitive blood pressure transducer with improved sensitivity," *IEEE Trans. Biomed. Eng.*, vol. BME-20, pp. 101–109, 1973.

[4] P. J. French and A. G. R. Evans, "Piezoresistance in polysilicon and its applications to strain gauges," *Solid-State Electronics*, vol. 32, no. 1, pp. 1–10, 1989.

[5] T. I. Kamins, "Hall mobility in chemically deposited polycrystalline silicon," *J. Apps. Phys.*, vol. 42, pp. 4357–4365, 1971.

[6] P. Rai-Choudhury and P. L. Hower, "Growth and characterization of polycrystalline silicon," *J. Electrochem. Soc.*, vol. 120, pp. 1961–1766, 1973.

[7] J. Y. Seto, "The electrical properties of polycrystalline silicon films," *J. Apps. Phys.*, vol. 46, pp. 5247–5254, 1975.

[8] C. T. Wang, *Applied Elasticity*, ch. 11, p. 286. McGraw-Hill Book Company, Inc., 1953.

[9] R. Pennell and J. Foerstner, "Resistivity control of boron-doped polysilicon resistors," *J. Electrochem. Soc.*, vol. 138, pp. 860–863, March 1991.

[10] H.-L. Chau and K. D. Wise, "Scaling limits in batch-fabricated silicon pressure sensors," *IEEE Transactions on Electron Devices*, vol. ED-34, no. 4, pp. 850–858, 1987.

Chapter 4

Integrated Microflow System

4.1 Introduction

A conventional fluid experiment always involves assembling many individual components such as fluid conduits, probes, a fluid supply system, etc. This method has also been used in experiments for studying microflow. Mostly, people assemble a micro-pipette with macro sensors attached to the ends of the channel[1, 2]. Although some interesting information has been revealed[1, 2, 3], the method used is obviously very primitive. A common problem shared by all the microflow experiments carried out in the past is that they have very limited or no access to microflow field; for example, the pressure measurement is limited at the entrance and exit of a microchannel. Even micro-scaled sensors have existed for a long time. There is no success of trying to assemble microsensors and channels together for flow measurements. Because a small interruption (from the view of macroscopic scale) could have a huge impact on a microflow system, trying to interface sensors with microchannels in the transitional manner is almost impossible.

A new approach is to make an integrated microflow measurement system[4]. Such a system includes at least two basic components; a microchannel for carrying the flow and micro sensors for measuring the physical properties of the fluid flow. Interfacing structures for introducing the fluid into the microchannel and connecting the sensors to the channel are also necessary in the integrated microflow system. It is hoped that, by shrinking the

measurement system to a microscopic scale, the interruption induced by the measurements becomes trivial or at least analytically tractable. Furthermore, interfacing two micro devices with the same fabrication basis is much easier than interfacing two devices with huge differences in their scales. So far, an integrated microflow measurement system is the most promising device for studying fluid flow on a microscopic scale.

Fluid pressure inside a microchannel is a very important physical parameter for both theoretical modeling and engineering applications[5], for example, flow meters utilizing pressure drop measurement across a non-uniform flow channel. Therefore, pressure sensors are chosen as the first micro sensors to be integrated with microchannels for the microflow measurement system. However, fabrications of an integrated microflow system are much more complicated than a simple mix of the two together. For example, the fabrications of the microchannels and sensors are all carried out on the front side of the wafer, while as we will see, the microflow systems are processed on both sides of the wafer. Furthermore, many extra processing steps are added in order to protect some devices while making the others. Therefore, one can find many ways of making microchannels and sensors, but there is a limited choice in making integrated microflow systems with given technology. As it is agreed, surface micromachining provides the most promising technology for integrating micro devices. In the following section, design and fabrication of several microflow systems fabricated with combined bulk and surface micromachining technology are discussed in detail.

4.2 The First Generation Microflow System

4.2.1 System Design

A schematic drawing of a typical microflow system is shown in Fig. 4.1. The system has a microchannel for carrying the fluid and a series of pressure sensors attached to the microchannel. These sensors are used to measure the pressure distribution along the channel. Pressure sensors are connected to the flow channel through a bridging channel which is made as small as possible to reduce its interruption to the flow. The structure of the bridging channel is shown in Fig. 4.2. At the end of the microchannel, there is a vertical inlet/outlet

hole for connecting the channel to the fluid supply system.

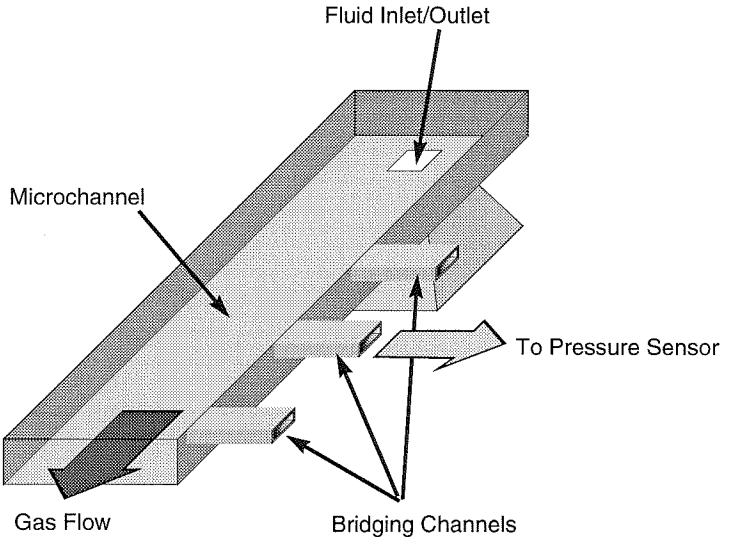

Figure 4.1: Schematic of a microflow flow measurement system.

Fig. 4.3 shows a photograph of a real microflow system (the first generation microflow system). In this system, there are three straight uniform cross-section microchannels each 3 mm long. The top channel is 5 μm wide and 1.2 μm high; the middle and bottom microchannel are 40 μm wide and 1.2 μm high. All the channels share the same inlet and outlet on the chip. There are four pressure sensors attached to the top and bottom microchannels. The diaphragm of the pressure sensors is 250×250 μm^2. The size of the bridging channel is 2×0.25 μm^2(w×h). The system is built on the surface of a silicon wafer with combined bulk and surface micromachining technology. The inlet/outlet holes are etched through to the back of the silicon substrate.

Since it is unknown what the pressure distribution might be, pressure sensors are placed with equal intervals along the microchannel. The total number of pressure sensors along the microchannel is constrained by two factors. One is the pressure sensitivity with given diaphragm size. For example, a large diaphragm will give better sensitivity but the distance between each sensors has to be larger. Another factor is the yield of the fabrication. Even if only one pressure sensor breaks during fabrication, the whole system

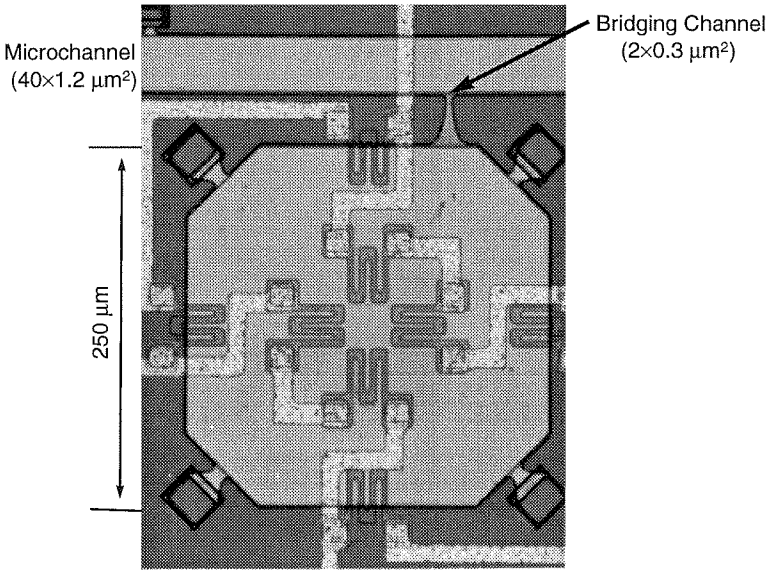

Figure 4.2: Photograph of a bridging channel which connects a pressure sensor to microchannel.

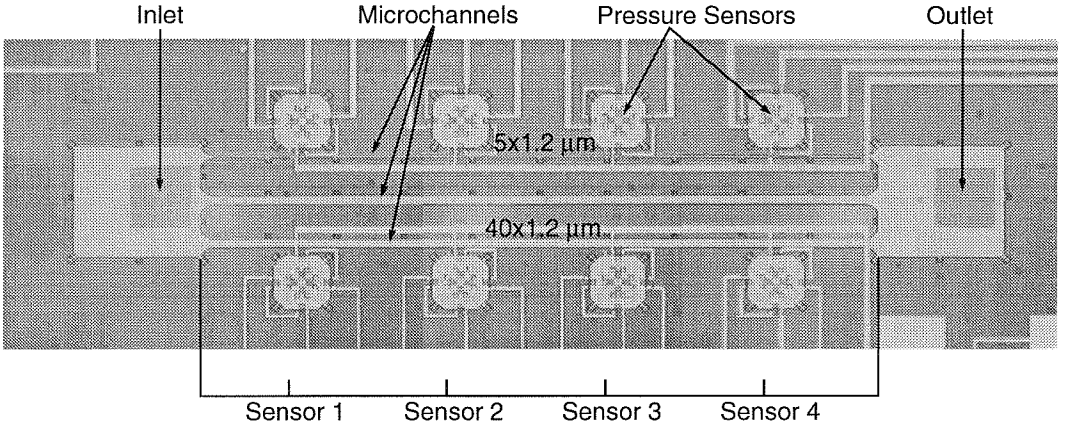

Figure 4.3: Photograph of the first generation microflow system.

becomes unusable. The more pressure sensor each microflow system has, the lower the yield is. Thus there are only eight pressure sensors in the first generation microflow system.

In order to investigate the dependence of pressure distribution upon the geometry of the channel, two microchannels with different widths are designed in the system which share the same inlet and outlet. Therefore, the same inlet/outlet pressure values are guaranteed.

4.2.2 Fabrication

The process flowchart for the first generation microflow measurement system is shown in Table 4.1. Correspondingly, the cross-sectional diagrams of the fabrication steps are shown in Fig. 4.4. A full description of the fabrication with process recipes and pictures of masks are in Appendix A. The following discussions will concentrate on the problems met during the fabrications.

Steps 1-6 The fabrication use 4" (100) wafers with no particular preference on p or n type as long as its doping level is low and would not cause any selectivity effect during the silicon etching process[6, 7]. The thin silicon nitride layer is used as the oxidation mask. Mask #1 (Fig. A.1) defines the cavity area for pressure sensors and microchannel. Silicon nitride is dry etched using a plasma etcher (SF_6 plasma) with an etching rate of about 120 nm/min. There are two possible processes which can be used to etch the silicon substrate: one is the dry etch with SF_6 plasma; the other is wet etch. Dry etching is preferred since it gives better uniformity across the whole wafer and the etching rate (about 100 nm/min) is more controllable than fast wet etching. However, for unknown reasons, the bottom of the cavities is sometimes not flat. To etch down 600 nm, the non-uniformity of the wet etching process can be as big as 200 nm across the wafer while it is definitely less than 100 nm with the dry etch technique. The wet oxidation process can take as long as four hours; in the end, the surface of the oxidation area should be the same level as the rest of the area protected by the silicon nitride film. A smooth surface topography is very important. The yield of the fabrication and the maximum pressure applicable to the pressure sensors partly depend upon the quality of the surface. For these reasons, the thin silicon nitride film (even if it is only 100 nm thick) is removed after the oxidation step. The silicon nitride is removed

Table 4.1: Flowchart for Fabrication of the 1st Generation Microsystem

1	Clean wafer	
2	Deposit LPCVD low-stress silicon nitride	(100 nm)
3	Do photolithography and pattern the nitride film	mask #1
4	Etch silicon substrate	(600 nm down)
5	Perform wet oxidation	(1.0 μm)
6	Remove silicon nitride film	
7	Deposit LPCVD PSG film	(250-300 nm)
8	Do photolithography and pattern PSG	mask #2
9	Perform PSG densification and reflow	
10	Deposit LPCVD low-stress silicon nitride	(1.2-1.3 μm)
11	Deposit LPCVD polysilicon	(500 nm)
12	Dope the polysilicon film	(heavy boron doping)
13	Do photolithography and pattern the polysilicon	mask #3
14	Deposit LPCVD low-stress silicon nitride	(400-500 nm)
15	Perform photolithography on the back of the wafer	mask #4
16	Pattern the back inlet/outlet holes	
17	Etch through silicon substrate to form the inlet/outlet	
18	Clean the wafer	
19	Perform photolithography to pattern etching holes	mask #5
20	Etch PSG/SiO_2 sacrificial layer	
21	Rinse and dry in-and-out	
22	Deposit PECVD oxynitride to seal the etching holes	
23	Protect wafer backside and pattern oxynitride	mask #6
24	Protect wafer backside and pattern the contact holes	mask #7
25	Perform metal evaporation	(1.0 μm Aluminum)
26	Protect wafer backside and pattern metal	mask #8
27	Sinter the contact	
28	Dice the wafer	

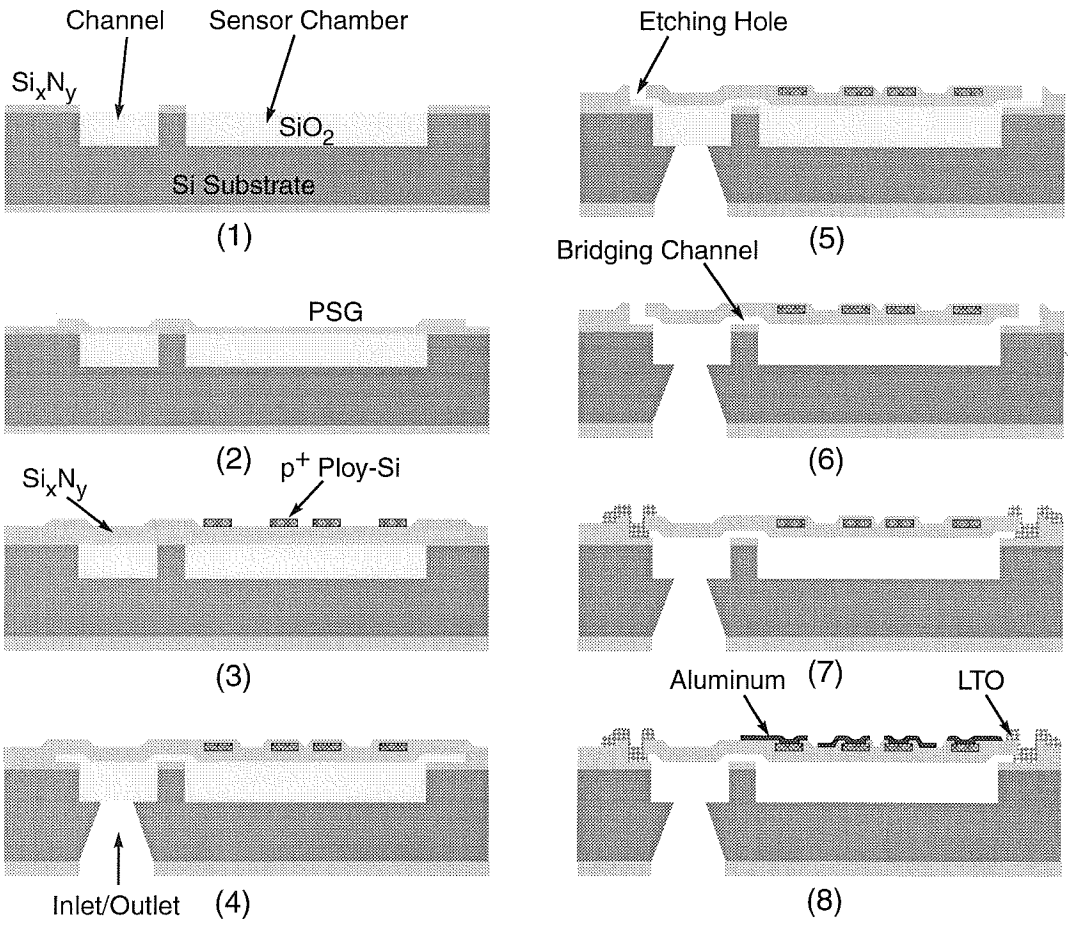

Figure 4.4: Schematics of the fabrication process for the first generation microflow system.

in heated H_3PO_4 (160-180 °C). Since the oxidation will also go into the silicon and nitride interface, a small bump is formed at the edge of the cavity. For 1.0 μm thick oxidation layer, the bump can be as high as 250-350 nm. The height of the bumps can be reduced by a planerization step; namely a photoresist spin cover and uniform plasma etching process.

Steps 7-9 The PSG layer studied in Chapter 2 is used here as the sacrificial material. The oxidation layer in step 5 is also used as the sacrificial layer. The microchannel, pressure sensor chamber, bridging channel and etching channel are all formed by sacrificial layer etching technique. However, the etching holes and bridging channels require much thinner sacrificial layer than the microchannels and sensor chambers. Thin etching channels are easier to seal. Thin bridging channels can reduce the interruption to fluid flow. Thus two layers of sacrificial material need to be deposited, but patterned differently. The mask #2 (Fig. A.1) defines the microchannel and chamber of the pressure sensor (these are the same as the mask #1), plus the etching channel and the bridging channel. The purpose of step 9 is to smooth out the corner of the PSG pattern for better silicon nitride coverage in step 10.

Steps 10-14 The quality of the silicon nitride film deposited in step 10 is very important. Intrinsic stress of the film should be carefully controlled (Chapter 3). As mentioned before, a strong intrinsic stress could reduce the pressure sensitivity significantly and tend to crack or peel off the film as it gets thicker. But if the stress is too small, the diaphragm can easily stick to the bottom after step 20. The deposition of the polysilicon film should follow immediately after the deposition of silicon nitride to avoid any possible contamination and moisture absorption. There are many ways to dope the polysilicon, for example, ion implantation, furnace diffusion, etc. The doping level is not controllable if using the furnace diffusion method. Ion implantation provides the most reliable and accurate doping of polysilicon. To pattern the polysilicon, either dry etching or wet silicon etching can be used. The dry etching method for example, RIE or plasma etching, is preferred since it is more controllable than wet etching, especially when etching very fine patterns. After these steps, the wafer should be very carefully cleaned. A diluted HF dip to remove the native oxidation layer is

necessary. The next step, another low-stress silicon nitride deposition, is done to protect the polysilicon from future EDP and concentrated HF etching. It is found that to ensure good step coverage, the minimum thickness of the nitride film is 300 nm (for a 500 nm polysilicon film).

Steps 15-18 Step 15 requires double-side alignment. Two ways have been used. The first method relies on the automatic loading accuracy of the GCA 4800 stepper. Usually a well maintained GCA 4800 has less than 50 μm loading error. This is tolerable in my case; the design of the back holes allow for 100 μm alignment error. The second method, using a specially designed double-side alignment kit, has a much better accuracy, 5 μm in most cases. Fig. 4.9 shows the working principals of the double-side alignment kit. The first method was used in the fabrication of the first generation microflow system. The misalignment of the back holes can be seen in Fig. 4.3. The second method is used in the fabrication of the second generation microflow system (Fig. 4.6). After photolithography, the silicon nitride is etched using a plasma etcher with SF_6 gas. At this step, the accumulated film thickness deposited on the backside is more than 2.0 μm (including both silicon nitride and polysilicon). To etch through, the etching time can be as long as 20 minutes. A very thick photoresist (at least 3.0 μm) layer has to be used. During the plasma etching, the wafer has to be rotated several times in the plasma chamber to maintain a relatively uniform etching across the whole wafer. After finishing, the wafer is put into a preferential silicon etchant to etch through the wafer (for the gas inlet/outlet holes). EDP (ethylene diamine, pyrocatechol, and water)[8] is used in most cases. TMAH is a very good replacement of EDP. After the EDP etching, the wafer should be carefully cleaned.

Steps 19-22 Step 19 is to pattern etching holes for the next sacrificial layer etching to form the microchannels and chambers. Since the silicon nitride layer is almost 2 μm thick and the underlying PSG is only 0.25$\sim$0.3 μm , the etching process (SF_6 plasma) should be conducted very carefully to avoid over etch. If the bottom silicon substrate (under the PSG layer) is being etched, the etch hole sealing process becomes difficult. Since the selectivity of plasma etching is very low, one can only use time to control the etching stop. Thus the

etching rate of low-stress silicon nitride and non-uniformity should be determined with test wafers before the real etch process.

After patterning the etching holes, the photoresist mask is ashed with oxygen plasma. Then the wafer is put into a specially designed beaker which contains highly concentrated HF solution (49 wt.%) to etch the PSG/SiO_2 composite sacrificial layer. The quality of the silicon nitride coverage in step 14 will show up in this step. If the coverage is bad, one will see small pieces of silicon nitride (yellowish) floating on the surface of the etchant, because once a small crack forms, the nitride intrinsic stress will immediately cause the film around the crack to peel off from the interface between the second nitride and the polysilicon or the first nitride layer. To solve this problem, one should improve the process quality (from the first nitride layer, step 10, to second nitride layer, step 14) and increase the thickness of the second nitride layer (however, this will compromise the sensitivity of the pressure sensors). The number of etching holes should be made such that the PSG/SiO_2 sacrificial layer etching time is no longer than 35 minutes. If longer than 35 minutes, the yield will be very low. The etching time of the first generation microflow system is 25 minutes; the second generation chip takes 30 minutes. Since the silicon nitride will be etched in concentrated HF (49 wt.%) at a rate of 40-50 Å/min, more than 100 nm silicon nitride will be etched during this sacrificial layer etching.

Since the HF goes as deep as several hundreds micrometers into the microchannels and chambers, the rinse time should be at least as long as the etching time in order to clean the microchannel inside[9]. The wafer drying process is carried out in a vacuum spin dryer. The high speed vacuum spin dryer helps to remove water from the microchannels and chambers. The intrinsic stress in the diaphragm will help it standing free after the water is removed[10]. To ensure a good sealing at the next step, the wafer should be baked at high temperature. If the next sealing process is carried out in a LTO furnace, wafer baking is automatically done during the nitrogen purge step of LTO deposition. The purpose of baking the wafer is to totally remove the moisture absorbed inside the microchannel and chambers.

The sealing deposition can be performed in many ways. The first generation microflow system uses PECVD oxynitride as the sealing material. For a 300 nm high etching

channel, at least 1 μm oxynitride is needed in order to seal all the microchannels and chambers. However, if LTO is used (low-temperature oxide) as the sealing material, 900 nm will be enough. As being mentioned before (Chapter 3), a sealed chamber of an isolated pressure sensor will show newton interference rings. This observation is used to check the yield of the sealing process.

Steps 23-28 Once finished with the sealing deposition, the microchannels and pressure sensors are closed with only two common openings at the backside of the wafer, the gas inlet/outlet holes. If any liquid gets into the channel or chamber, it will be extremely difficult, though not impossible, the remove them from the system. Even if the liquid is removed, some dirt marks will still be left on the silicon nitride film. So before any wet process, the wafer backside should be properly covered to prevent liquid from getting into the system through the back-holes. A plastic film which is normally used in wafer dicing to hole a wafer is used here. The plastic film can stand BHF for a very long time; but acetone and piranha (H_2SO_4:H_2O_2=5:1) can attack the film. Thus the wafer can only be dry cleaned. Fortunately, there is only one metal deposition left in the following steps and no problems have been found to be related with the wafer cleaning problem. However, the film can not stand high temperature. It should be removed before baking photoresist. The sealing layer, either oxynitride or LTO, are etched with buffered HF. A very thick photoresist should be used to protect the wafer in the BHF etching. For example, a 3.0 μm thick KTI 100CS photoresist spin at 2 krpm is used in the fabrication. The hard bake should be avoided since some micro cracks may form during the hard bake which lead to protection failure in BHF etching. The purpose of patterning the sealing layer is to reduce the total thickness of the diaphragm and to reduce the film thickness above the polysilicon contact area. The second purpose is very important to ensure good connection without depositing a very thick metal layer. (The metal deposited using evaporation technique has a very bad step coverage. So if the step is too high, it needs a very thick metal layer to ensure all wire connections are good.) The silicon nitride above the contact windows are etched in CF_4 plasma which has a better selectivity of etching nitride over heavily doped polysilicon. Since the highest step on the wafer is 1.0 μm (the sealing layer), the minimum

thickness of metal layer should be at least 1.0 μm. Finally, after the aluminum is sintered, the wafer is diced with a photoresist protection layer. The photoresist ashing finishes the whole fabrication process.

4.3 The Second Generation Microflow System

4.3.1 Design of Thirteen Sensors Microflow System

With the four sensors microflow measurement system (Fig. 4.3), some interesting results have been observed during the flow experiments[4]. However, there are also several interesting problems that can not be studied with this system; first, because three microchannels share one pair of inlet/outlet holes, individual flow rate measurements for each microchannel is impossible; second, there are only four pressure sensors in each system, and none on the inlet and outlet so that the pressure drops from the external pressure transducers to the inlet is unknown; third, there are no temperature sensors for measuring the temperature distribution, another very important physical parameter for studying microflow. These problems are all addressed in the following 13 sensors microflow system.

Fig. 4.6 shows a photograph of the second generation microflow system. There are a total of 13 pressure sensors in the system. Two are directly placed on top of the inlet and outlet (utilizing the cover of the inlet/outlet as the diaphragm of the sensor). Eleven pressure sensors are distributed along a 4.5 mm long and 40×1.2 μm^2in cross section microchannel. Eleven temperature sensors (polysilicon thermistors) are placed at those positions where the pressure sensors attach to the microchannel (see the magnified photograph in Fig. 4.6). Furthermore, there is only one microchannel connected to the inlet/outlet holes.

The pressure sensors are the same as those in the first generation microflow system. The width of bridging channel is increased at the sensors end for reducing the sensor responding time. The interval between sensors is the minimum achievable with the 250×250 μm^2pressure sensors. Another ten isolated pressure sensors are also placed near to the microchannel for the purpose of sealing check during the fabrication.

The temperature sensor is made with lightly doped polysilicon. The measured sheet resistance and temperature coefficient as a function of boron doping concentration is shown

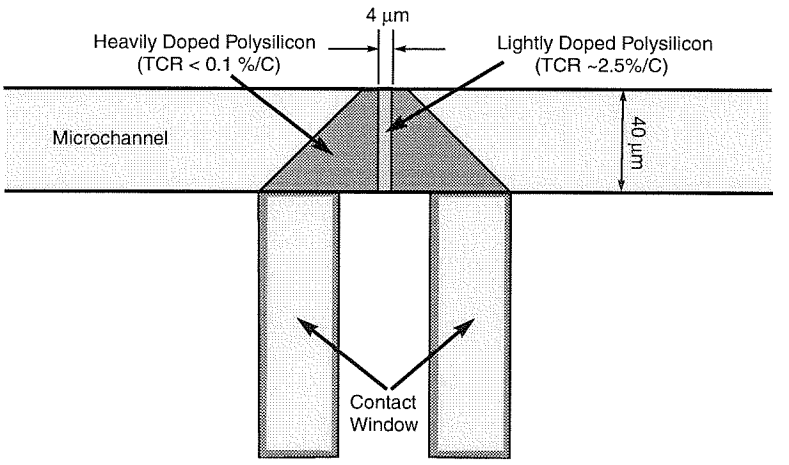

Figure 4.5: Design schematics of a temperature sensor.

in Fig. 3.18. As one can see, if the dose in polysilicon is about 10^{15} cm^{-2}, the TCR of the polysilicon can be as large as 2-3%/°C. However, since the resistivity of the lightly doped polysilicon is very large (Fig. 3.18), the number of squares of the lightly doped polysilicon resistor has to be made very small (0.1 □ here), so that the resistance of the temperature sensor is in an adequate range for electrical measurement (several KΩ to hundreds of KΩ). In order for the temperature sensor to be sensitive to the temperature changes along the microchannel, the thermal capacity of the sensing part should be as small as possible. In the final design, the temperature sensors are patterned directly on top of the microchannel. The design schematic of the temperature sensor is shown in Fig. 4.5.

Obviously, there are many ways to integrate the temperature sensors in the microflow system. The first consideration of our approach is not to make the fabrication too complicated. Thus, the same polysilicon is used for both strain gauges and temperature sensors (with different doping concentration). Doing that, only one extra mask is added to the original fabrication process (the one used in the fabrication of the first generation microflow system). Other changes to the process are trivial. Details of the fabrication are discussed in the next section.

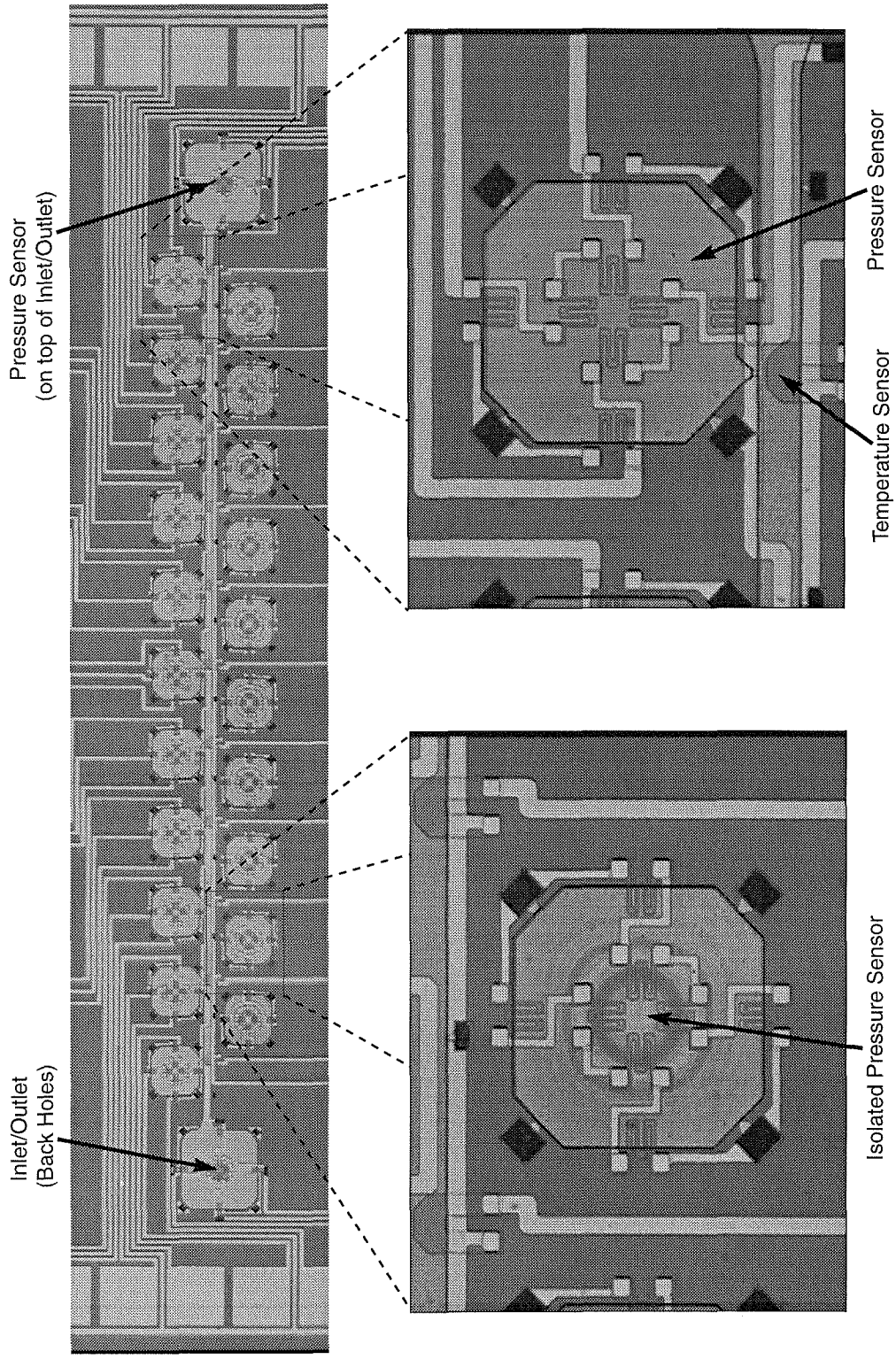

Figure 4.6: Photograph of the second generation microflow system.

4.3.2 Design of A Width-Varying Microchannel/Pressure Sensors System

There are two major purposes of designing a width-varying microchannel/pressure sensors system. One of the purposes is to study the geometry effect. An interesting question is how the microflow is affected by changing the cross-sectional area of the channel. The other purpose is to explore possible engineering applications of a non-uniform microchannel; in other words, to find the possibility of using a non-uniform microchannel for extremely small flow rate measurements ($\sim$ 1 μl/min); such a device in macro scale is called a *Venturi* flowmeter.

The design of the width-varying microchannels is similar to the conventional venturi tube[11]. Fig. 4.8 shows the proportionally scaled layout including the gas inlet and outlet. Different from the conventional venturi tube, however, the cross section of the micro venturi meter is a rectangle with high aspect ratio (width/height$\gg$10). With surface micromachining technology, the width of the channel is a design variable while the height is fixed throughout the channel. Here, the height of the microchannels and the pressure sensors is chosen to be 1.2 μm, which is determined by the thickness of the PSG/SiO_2 sacrificial layer we used during fabrication. As seen in Fig. 4.8, there are three different transition designs in each channel and each transition has its own widths at the entrance/throat/exit ($w_1/w_0/w_2$) and angles of entrance/exit (θ_1/θ_2) as defined in Fig. 4.7.

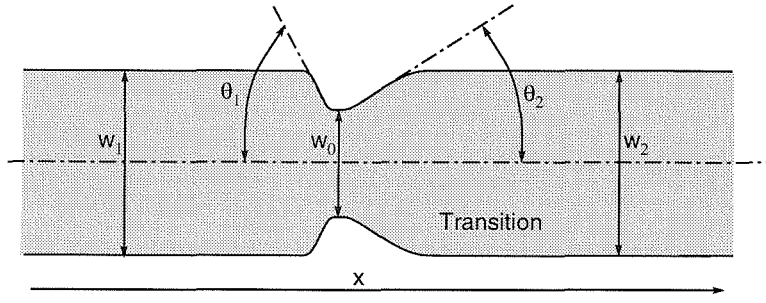

Figure 4.7: Design parameters for micro transition.

Note that each channel has only two gas inlet/outlet holes, so the three transitions will have the same flow rate during steady-state flow experiments. Also shown in Fig. 4.8 are the 14 pressure sensors that are integrated along the microchannel with predetermined

positions. The size of the pressure sensor is 250×250 μm^2. To monitor the pressure distribution inside the channel with minimum flow interference, each sensor is connected to the channel through a small bridging channel with the cross section of only 2×0.3 μm^2 at the junction. This is the same design that has been used in the first generation microflow system[4].

4.3.3 Fabrications of The Second Generation Microflow System

A flowchart for the fabrication of a 13 sensors system is shown in Table 4.2. The fabrication of the 13 sensors microflow system is mostly the same as that of the four sensors system. The differences are related with the patterning and doping of the temperature sensors.

The first change noticed in the Table 4.2 is, instead of depositing polysilicon, α-silicon is deposited in step 12. This α silicon is converted to polysilicon later by a high temperature annealing process (at 950 °C). It is found that this process can increase the polysilicon grain size, thereby increasing the gauge factors for pressure sensors by as much as 25%. Further more, the repetition of the polysilicon parameters such as resistivity, TCR and gauge factor is much better than those of the polysilicon deposited directly at 620 °C.

Since the temperature sensor requires very lightly doped polysilicon, a two-step ion implantation process is used; first, the whole α-silicon film is lightly doped with a dose of 5×10^{15} cm^{-2}; then a 2.5 μm thick photoresist is coated and patterned with temperature sensors (the photoresist is used as the ion implantation mask); the second ion implantation follows to heavily dope the α-silicon film. After that, the wafer is put into an annealing furnace at 950 °C for 30 minutes. As a result, the α-silicon is converted to polysilicon and the dopants are activated at the same time. The strain gauges for pressure sensors and resistors for temperature sensors are both patterned in step 16 with mask #4.

The second change is the step of patterning the PSG etching holes is moved to right after the step of patterning the back inlet/outlet holes. Since EDP etches PSG very slowly, this change would not affect the PSG etching, but it reduces one step of handling the EDP etched wafer (After EDP etching, the wafer has a lot back holes, and is very fragile).

The third change is in step 26: low temperature thermal oxide (LTO) deposited in LPCVD system is used as the sealing layer (in comparison with PECVD oxynitride, LTO

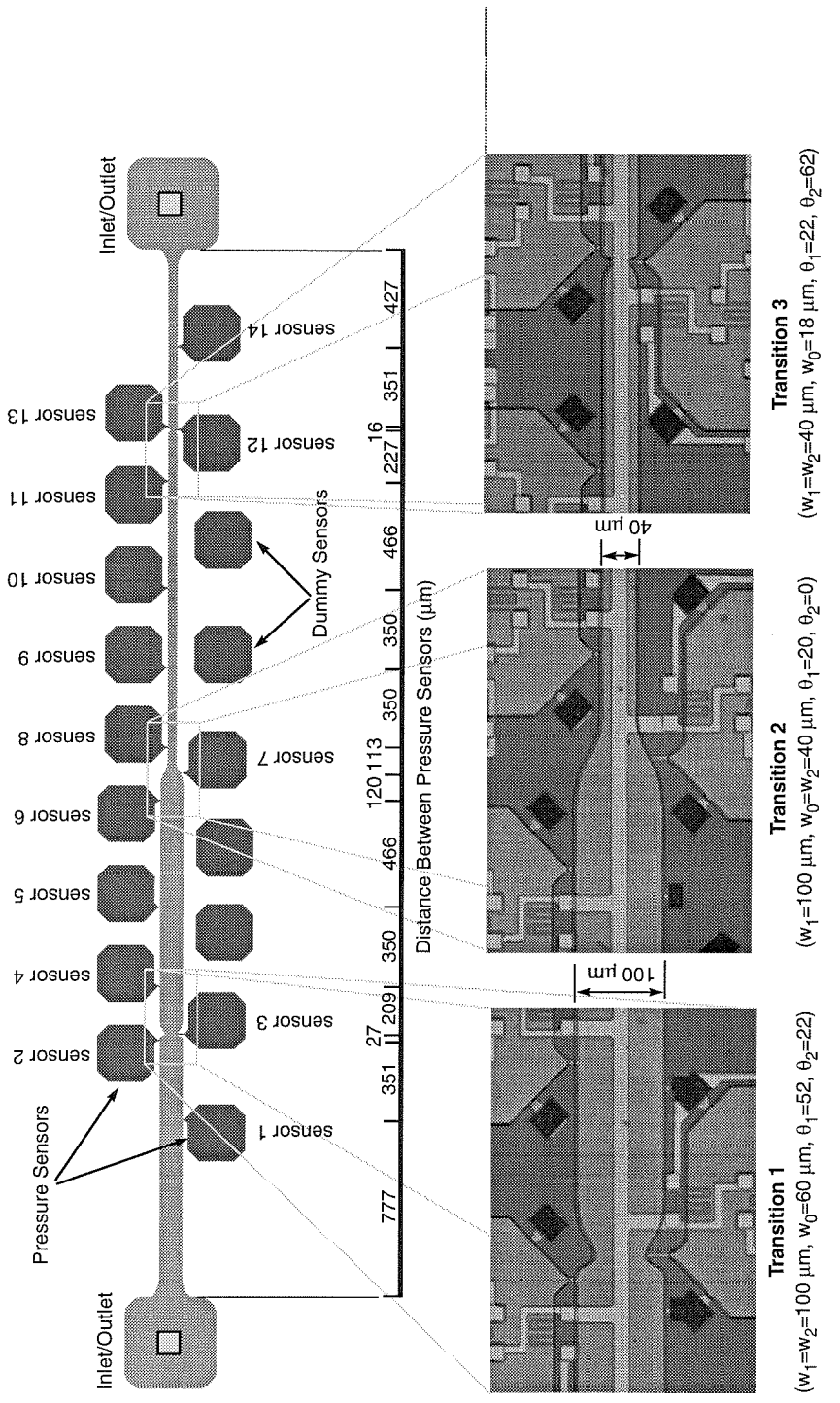

Figure 4.8: Design schematics and photograph of the micro transition channel system.

Table 4.2: Flowchart for Fabrication of the 1st Generation Microsystem

1	Clean wafer	
2	Deposit LPCVD low-stress silicon nitride	(150 nm)
3	Do photolithography and pattern the nitride film	mask #1
4	Etch silicon substrate	(600 nm down)
5	Perform wet oxidation	(1.0 μm)
6	Remove silicon nitride film	
7	Deposit LPCVD PSG film	(250-300 nm)
8	Perform PSG densification	
9	Do photolithography and pattern PSG	mask #2
10	Perform PSG reflow	
11	Deposit LPCVD low-stress silicon nitride	(1.2-1.3 μm)
12	Deposit LPCVD α-silicon	(550 nm)
13	Boron ion implantation	(10^{16} cm^{-2})
14	Perform photolithography	mask # 3
15	Boron ion implantation	(10^{20} cm^{-2})
16	Anneal α-silicon, convert to polysilicon	(950 °C)
17	Do photolithography and pattern the polysilicon	mask #4
18	Deposit LPCVD low-stress silicon nitride	(400-500 nm)
19	Perform photolithography on the back of the wafer	mask #5
20	Pattern the back inlet/outlet holes	
21	Pattern the front etching holes	mask #6
22	Etch through silicon substrate to form the inlet/outlet	
23	Clean the wafer	
24	Perform photolithography to pattern contact holes	mask #7
25	Etch PSG/SiO_2 sacrificial layer	
26	Rinse and dry in-and-out	
27	Deposit LPCVD LTO to seal the etching holes	
28	Perform photography and pattern PSG	mask #8
29	Perform metal evaporation	(1.0 μm Aluminum)
30	Protect wafer backside and pattern metal	mask #9
31	Sinter the contact	
32	Dice the wafer	

has better uniformity across the wafer and fewer pin holes). It is found that a 300 nm high etching channel can be totally sealed with 900 nm thick LTO. Since, however, the LTO will be deposited on both sides of the wafer, the backside of the wafer should be protected to prevent LTO from sealing the back inlet/outlet holes. This can done by putting another dummy wafer on the back and sliding both wafers into one slot (the slot should be wide enough to hold two wafers) on the LTO boat.

4.4 Fabrication Related Problems

4.4.1 Double Side Alignment

In the fabrication of the second generation microflow measurement system, a special kit is used to do the double-side alignment. The procedure and the kit is described below.

The double-side alignment kit consists of two glass plates (made from the chrome masks) and a plate holder. On both plates, there are several alignment marks; some are to be copied to the wafer; some are used to align these two plates to each other (Fig. 4.9). On the bottom plate, there is a horizontal and a vertical metal strip (a little thinner than the wafer) which are used to align the wafer to the plate.

The crucial step is to make alignment marks on both sides of the wafer. To do that, one first spin coats photoresist on both sides of the wafer and then does soft bake. When ready, the wafer is placed on the bottom plate of the kit (Fig. 4.9(a)) and pushed against the alignment stopper. Then the top plate of the kit is placed on top of the wafer and aligned to the bottom plate (Fig. 4.9(b)). The two plates with the wafer sandwiched in between are then carefully clamped together (Fig. 4.9(c)). Finally, both sides of the wafer are exposed using a UV-light source. After developing and hard baking, the alignment marks are patterned to the wafer. These alignment marks are used as the reference for all other photolithography steps. If the operation is performed very carefully, the alignment inaccuracy of this method is less than five micrometers.

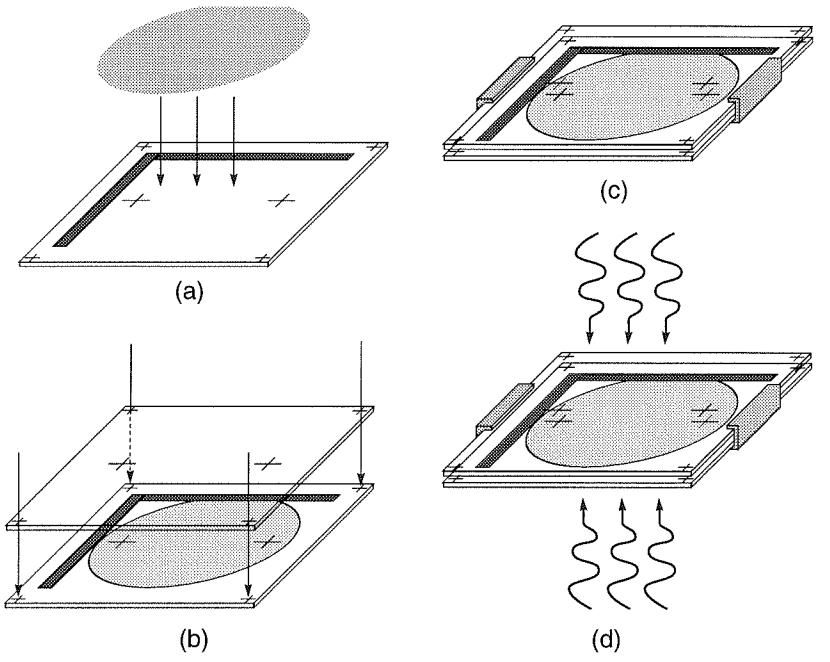

Figure 4.9: Schematic procedures of making alignment marks on both sides of a wafer.

4.4.2 Intrinsic Stress

To measure the intrinsic stress in films, two methods have been used in the fabrication. One is to deposit films on test wafers and then measure the bending of the wafer; the other is to use on chip test patterns (specially designed for intrinsic stress tests). More details about these two methods will be discussed below.

Wafer Curvature Measurement

The procedure for wafer curvature measurement is first clean a test wafer and measure its curvature; second, deposit a thin film layer; finally, measure the wafer curvature again. If the film is deposited in the LPCVD system, the film on one side of the wafer needs to be removed before performing the curvature measurement. The curvature of the wafer is measured with a profilometer. Fig. 4.10 shows the schematics of this method. The stress

in the film can then be calculated using Stoney's formula which is

$$\sigma_f = \frac{4\delta E_s d_s^2}{3D^2(1-\nu_s)d_f} \tag{4.1}$$

where d_f, d_s are the film and substrate thickness, δ is the change in the total wafer deflection resulting from the application of the film measured at the center of the wafer, D is the diameter of the substrate, and E_s, ν_s are the Young's modulus and Poisson's ratio of the substrate. Some precautions should be taken in order to make the deflection measurement accurate[12]. This method has be widely used in industry for measuring the film stress.

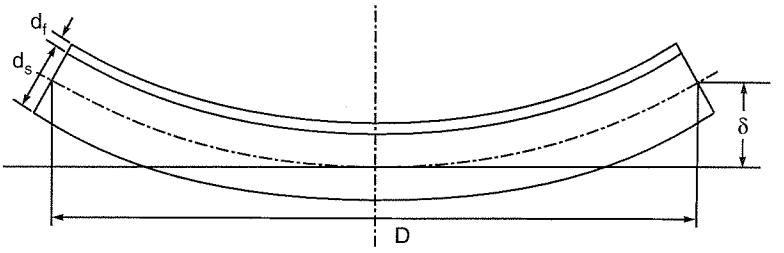

Figure 4.10: Schematics of the wafer curvature method for thin film stress measurement.

On-Chip Test Structure Methods

Using on-chip test patterns to decide the film intrinsic stress is proposed by H. Guckel[13]. He designed free-standing beams and other structures fabricated from films to estimate the strain level in the film. Both compressive and tensile stress can be calculated from the deformation of the structures. This method has been adopted by many people[14, 15]. Fig. 4.11 shows an on-chip stress test pattern used in the fabrication of the microflow system. Using this structure, the strain is converted into a rotation of a beam. The larger the tensile stress, the larger the rotation angle. The strain in the film can be estimated by the following formula:

$$\epsilon = \frac{l}{2L} tan(\theta) \tag{4.2}$$

Since this model does not include the resistance of structure deformation, Eq. 4.2 needs to include a correction factor[15] if more accurate strain values are required.

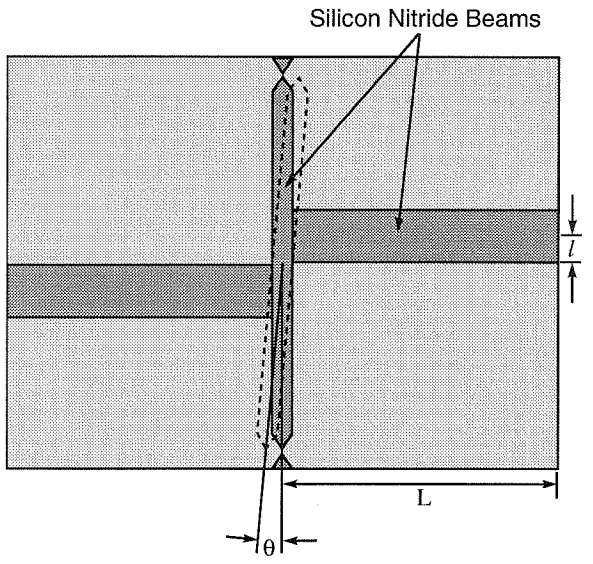

Figure 4.11: Schematics of an on-chip intrinsic stress test pattern for silicon nitride film. The structure is free-standing on top of the silicon substrate after the underneath PSG layer is removed.

4.5 Summary

Integrated microflow systems have been designed and successfully fabricated. The first generation microflow system has three microchannels and total eight pressure sensors. The second generation chip has two microflow system, one is a constant area microchannel with total thirteen pressure sensors, the other is a width-varying microchannel with three venturi-meter-like transitions. To fabricate such microflow systems, many technical problems have been solved i.e., silicon nitride stress, sacrificial PSG etching, chamber dry and double side alignment etc. A detail description of the fabrication of the microflow system is presented.

Bibliography

[1] J. Pfahler, J. Harley, and H. Bau, "Gas and liquid flow in small channels," in *Micromechanical Sensors, Actuators, and Systems*, vol. 32, pp. 49–60, ASME, 1991.

[2] S. B. Choi, R. F. Barron, and R. O. Warrington, "Fluid flow and heat transfer in microtubes," in *Micromechanical Sensors, Actuators, and Systems*, vol. 32, pp. 123–134, ASME, 1991.

[3] E. B. Arkilic, K. S. Breuer, and M. A. Schmidt, "Gaseous flow in microchannels," in *Application of Microfabrication to Fluid Mechanics 1994, International Mechanical Engineering Congress and Exposition* (P. R. Bandyopadhyay, K. S. Breuer, and C. J. Blechinger, eds.), vol. 197, (Chicago, Illinois), pp. 57–66, Academic Press, November 1994.

[4] J. Liu, Y.-C. Tai, K.-C. Pong, and C.-M. Ho, "Micromachined channel/pressure sensor systems for microflow studies," in *The 7th International Conference on Solid-State Sensors and Actuators, Transducers' 93*, (Yokohama, Japan), pp. 995–997, June 1993.

[5] A. Beskok and G. E. Karniadakis, "Simulation of heat and momentum transfer in complex microgeometries," *J. of Thermophysics and Heat Transfer*, vol. 8, pp. 647–755, Oct.-Dec. 1994.

[6] A. Bohg, "Ethylene diamine-pyrocatechol-water mixture shows etching anomaly in boron-doped silicon," *J. Electrochem. Soc.*, vol. 118, p. 401, 1971.

[7] J. C. Greenwood, "Ethylene diamine-catechol-water mixture shows preferential etching of p-n junctions," *J. Electrochem. Soc.*, vol. 116, p. 1325, 1969.

[8] R. M. Finne and D. L. Klein, "A water-amine-complexing agent system for etching silicon," *J. Electrochem. Soc.*, vol. 114, p. 965, 1967.

[9] D. J. Monk, *Controlled Structure Release for Silicon Surface Micromachining.* PhD thesis, University of California at Berkeley, Chemical Engineering, Graduate Division, 1993.

[10] C. H. Mastrangelo and C. H. Hsu, "Mechanical stability and adhesion of microstructures under capillary forces," *Journal of Microelectromechanical Systems*, vol. 2, no. 1, pp. 33–55, 1993.

[11] R. W. Miller, *Flow Measurement Engineering Handbook*, ch. 9, pp. 9–1. McGraw-Hill, New York, 1989.

[12] N. A. Winfree, Y.-C. Tai, W. H. Hsieh, and R. Wu, "The effects of boundary conditions on implementing the stoney formula for stress measurements," in *The 7th International Conference on Solid-State Sensors and Actuators, Transducers' 93*, (Yokohama, Japan), pp. 179–182, June 7-10 1993.

[13] H. Guckel, T. Randazzo, and D. W. Burns, "A simple technique for the determination of mechanical strain in thin films with applications to polysilicon," *J. Appl. Phys.*, vol. 57, pp. 1671–1675, March 1985.

[14] L. Lin, R. T. Howe, and A. P. Pisano, "A passive, *in-situ* micro strain gauge," in *Proceedings of IEEE Micro Electro Mechanical Systems*, (Fort Lauderdale, Florida), pp. 201–206, IEEE, February 7-10 1993.

[15] B. P. van Drieenhuizen, J. F. L. Goosen, P. J. French, and R. F. Wolffenbuttel, "Comparison of techniques for measuring both compressive and tensile stress in thin films," *Sensors and Actuators*, vol. 37-38, no. A, pp. 756–765, 1993.

Chapter 5

Gaseous Flow Experiments and Modeling

5.1 Introduction

Gaseous flow experiments in channels ranging from several microns to a hundred microns have been conducted by Pfahler et al.[1] (using micromachined channels) and Choi et al.[2] (conventional capillary tubes). Their results show a smaller friction factor than predicted with continuum flow theory (*Navier-Stokes equation*). It is then suggested that this phenomenon may be attributed to a non-continuum effect. A recent experimental study of microchannel flow conducted by Arkilic et al.[3] confirms that a continuum flow theory (N-S equation plus continuum boundary conditions) can not model the momentum transferred from the fluid to the channel wall and therefore underestimates the mass flow rate for given inlet and outlet pressures. However, if using a slip-flow boundary condition at the channel wall, solutions of the Navier-Stokes equation can fit nicely to the results of gas flow experiments.

These efforts are targeted to several fundamental questions; first, at what size scales do the continuum assumptions break down; second, what is the model which can describe the microflow; third, what are the microflow specific phenomenons. Experiments conducted by Pfahler et al.[1, 2, 3] represents a typical method used by many people who study microflow

experimentally. However, as said before, this method is limited to the two-point pressure and flow rate measurements. These experiments are enough to show the fail of continuum theory in modeling microflow, but may not be enough to prove which model is correct.

The experimental results shown in this chapter are primitive. However, it proves that the design and fabrication of the integrated microflow system are very successful. Using the microflow system, pressure distribution along microchannels with uniform cross-sectional area and venturi-meter-like transitions are measured. The experimental results reveal some very interesting and even unexpected phenomenons never observed before. In addition, a simplified flow model with slip boundary conditions is developed to help analyzing the experimental data. In the following sections, the experimental setup and methods for gaseous flow measurements and data processing are described at the first. Then the measured data and a flow model are discussed. Finally, a brief summary and description of a new integrated microflow system are presented.

5.2 Experimental Setup

5.2.1 Chip Packaging

Since the microflow system chip includes both a fluid system and an electrical system, a new chip package needed to be developed. After the chip is fabricated, it is diced into a 1×1 cm^2 or a 1×0.5 cm^2 with two back holes for gas connections. On each chip there are often more than 30 wire bonding pads for connecting sensors to voltage source, voltmeters or data acquisition system. Fig. 5.1 shows the method developed with a 128-pin PGA package (donated by Xerox Ltd. Co.). The package has 1.1×1.1 cm^2 square cavity with metal substrate (copper coated with gold).

First, two holes are drilled on the bottom of the PGA package. The distance between the two holes are equal to that on the chip. The diameters of the holes on the package are bigger than that of the tubing which is a flexible Tygone tube (R3603). Second, the tube is glued directly to the back-holes of the chip using super glue (Loctite 404) (Fig. 5.1). A special kit is used during the procedure to hold the tube firmly against the chip. The operation should be carried out very carefully to avoid the liquid glue getting into the back

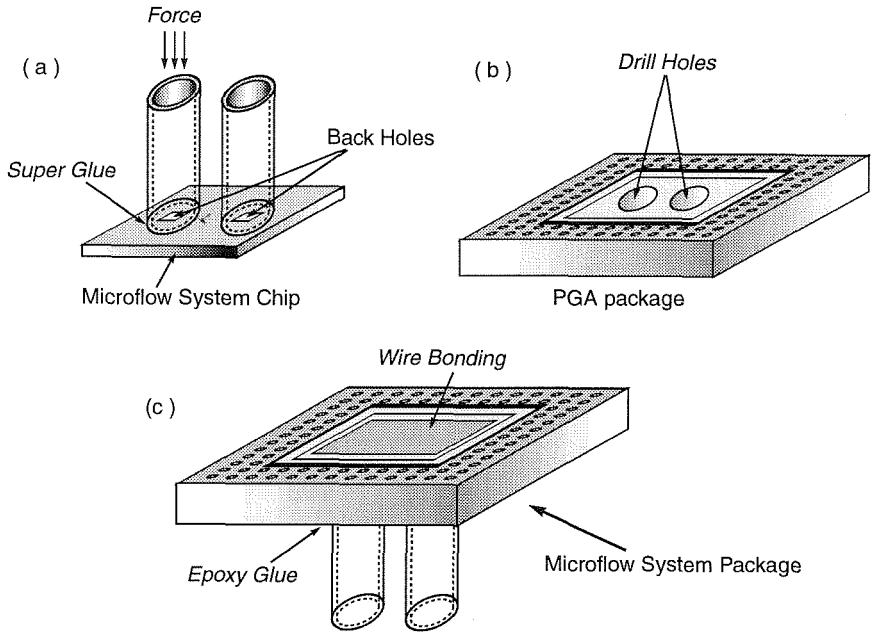

Figure 5.1: Schematics of the packaging procedure for microflow system chip.

holes. Once the glue is dried, the chip with tubes is inserted into the package and glued with 5 minutes epoxy glue. The epoxy is also used to fill the gap between the tubing and the back-holes of the package. Finally, wire bonding is performed to connect all the bonding pads from the chip to the package. Pressure test shows this kind of package can stand up to 70 psig without burst. A leak test in water is always performed for checking the quality of the package. Fig. 5.1 shows a photograph of the package.

5.2.2 Fluid System Setup

The gas supply system is shown in Fig. 5.2. The gas system consists of a gas cylinder, a low pressure reservoir, a 0.1 μm and a 0.01 μm particle filter, a commercial pressure transducer and several control valves as shown in Fig. 5.2. These components are connected with stainless steel tubing (1/4 in.) and leak-tight valves. A photograph of the finally assembled gas system is shown in Fig. 5.3.

During microflow experiments, the reservoir is charged by the high pressure gas cylinder to a pressure the microflow chip can stand with. The inlet and outlet valves are

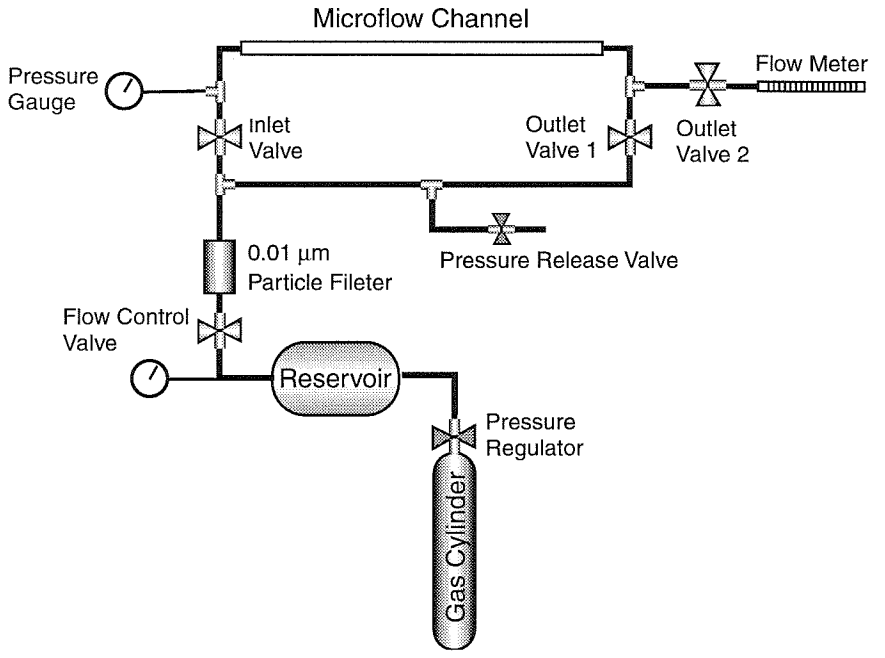

Figure 5.2: The schematics of the gas supply and control system for microflow experiments.

both opened during pressure sensors calibration; the flow control valve is used to set the pressure level applied to the chip (in the section from the control valve to the chip). The vent valve is used to quickly release the system pressure. During the gas flow measurements, the outlet valve is closed (the inlet valve open; the vent valve is always closed unless for releasing the pressure); the flow control valve is fully open. The reservoir is used to supply and maintain a constant pressure on the inlet of the microflow chip. It is found that the reservoir, once pressurized to a desired value, provides a very stable flow to the microchannel under continuous operation for up to several hours. In addition, it also prevents pressure surges or fluctuation that can burst the inlet/outlet diaphragms. The 0.01 μm filter is to prevent fluctuations and channel blockage caused by trapped particles in the gas system. Before using, the system is first purged with N_2 to remove particles in the system.

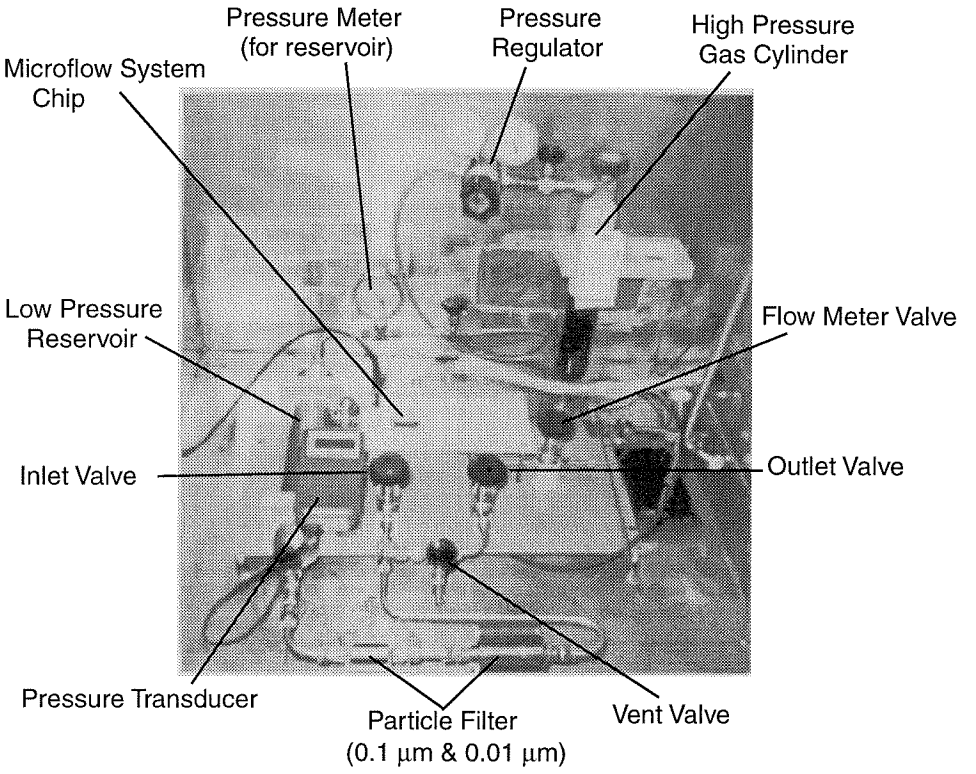

Figure 5.3: Photograph of the gas system setup for microflow experiments.

5.2.3 Data Acquisition System

System Setup

To speed up the microflow experiments, an automatic data acquisition system has been set up for simultaneous measurement of all the pressure sensors on a microflow system chip. Fig. 5.4 shows the schematics of the data acquisition system.

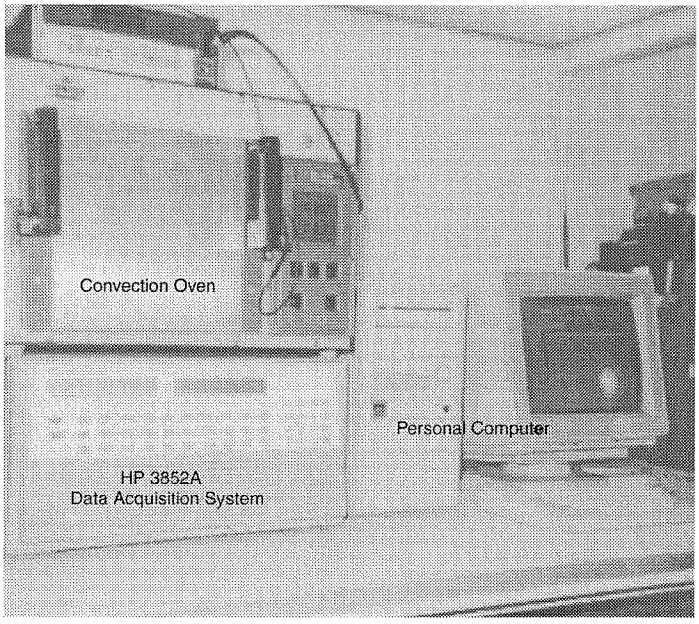

Figure 5.4: The photograph of the data acquisition system.

The data acquisition system consists of a programmable DC power supply (Keithley 230), and a HP3852A programmable data acquisition unit connected to a personal computer using HP-IB protocol. The HP3852A has a 24 channel (analog, differential) multiplexer and a 100 kHz 16-bit digital multimeter. The keithley 230 is used to provide the DC voltage source for all the pressure sensors. The output from the pressure sensors and temperature sensors are directly connected to the input of the HP3852A multiplexer through a shielded cable. Using this system, we are able to do time average of sampled data to significantly improve the signal-to-noise (S/N) ratio. The computer for controlling the data acquisition system is included in Appendix B.2.

Since the output of the pressure sensors are the differential voltage signal from their unbalanced Wheatstone bridges, the system is vulnerable to pick up noise from its environment. It is thus very important to carefully ground the instruments and cables. Multi-point grounding should be avoided as much as possible. All the cables for the differential signals should be shielded and grounded adequately.

5.3 Microflow Experiments

Data Collection and Processing

During studying the pressure sensors, it is found that one major error source in the measurement is sensor noise. Without applying any noise reduction technique, the equivalent noise level can be larger than ± 1 psi. If using the AC drive technique (ch. 3), that error can be reduced to less than ± 0.05 psi. It would be sufficiently accurate for microflow experiments. However, to use the AC drive method in multi-channel microflow measurement, the system setup has to be rearranged. One way is to insert an analog multiplexer in between the chip output and the lock-in amplifier (LIA), and put the digital multimeter at the output of the LIA. However, since the DC offset of sensors varies from 50 mV to 0.5 V, the signal has to be preconditioned before input to the LIA. This significantly complicates the experimental setup. Not only that, since the HP data acquisition system is an integrated system, it will take a lot of effort to configure it the way described above.

The route taken here is to use the data acquisition system to collect a large amount of data and do computer data processing. In a microflow measurement, the data acquisition system scans every sensor and the sampled data is transferred to a PC. To increase the signal-to-noise ratio, 256 such scans are performed in less than one minute; the averaged data for each sensor are stored in the computer. To further reduce the low-frequency noise, more than 30 averaged data are collected for each inlet pressure setting. In other words, the total integration time for each pressure measurement is about 30 minutes (for all sensors). If necessary, longer integration time is used. With this method, the differential voltages from pressure sensors can be accurately measured (in most cases $< \pm 0.3$).

The voltage measurements of the pressure sensors are converted to pressure values

using the sensitivity measured in a separate calibration procedure. Inaccurately measured sensitivity is another important error source of the microflow measurement. To reduce that error, multi calibrations are performed before, between and after gas flow measurements. An averaged value of all the measured sensitivities for each sensor are finally used to translate the voltage into pressure.

5.3.1 Pressure Sensor Calibration and Gas Flow Measurement

The microflow experiments start first with the calibration of all pressure sensors. The operation procedure is listed below:

1. Open the pressure regulator on the high pressure gas cylinder and charge the low pressure reservoir to about 30 psi (Fig. 5.2).
2. Close the vent valve and flow meter valve, and open both inlet/outlet valve.
3. Use the needle valve (flow control valve) on the reservoir to set the pressure applied on the microflow system chip (its inlet/outlet) to a desired value, i.e., 2.0 psig.
4. After waiting for at least one minute to let the system stabilize, take a measurement with the data acquisition system.
5. Repeat step 3 to 4 with different pressure settings until the desired pressure range is covered.

As an example, Fig. 5.5 shows calibrations of the pressure sensors in a non-uniform microchannel system. To find the sensitivities, a linear function is used to fit each calibration curve using least-square fitting method[4]. The slope and the offset of the linear function represent the sensitivity and zero pressure DC offset of the pressure sensor. Such calibrations are performed many times for each microflow experiment.

After calibration, the low pressure reservoir is first charged to the desired pressure. Then the outlet valve is closed, the inlet and flow meter valves are opened. Finally the flow control valve is gradually opened and the pressure is then applied to the inlet of the microchannel system and gas flow starts. After waiting for several minutes to let the flow stabilize, the electrical measurements start.

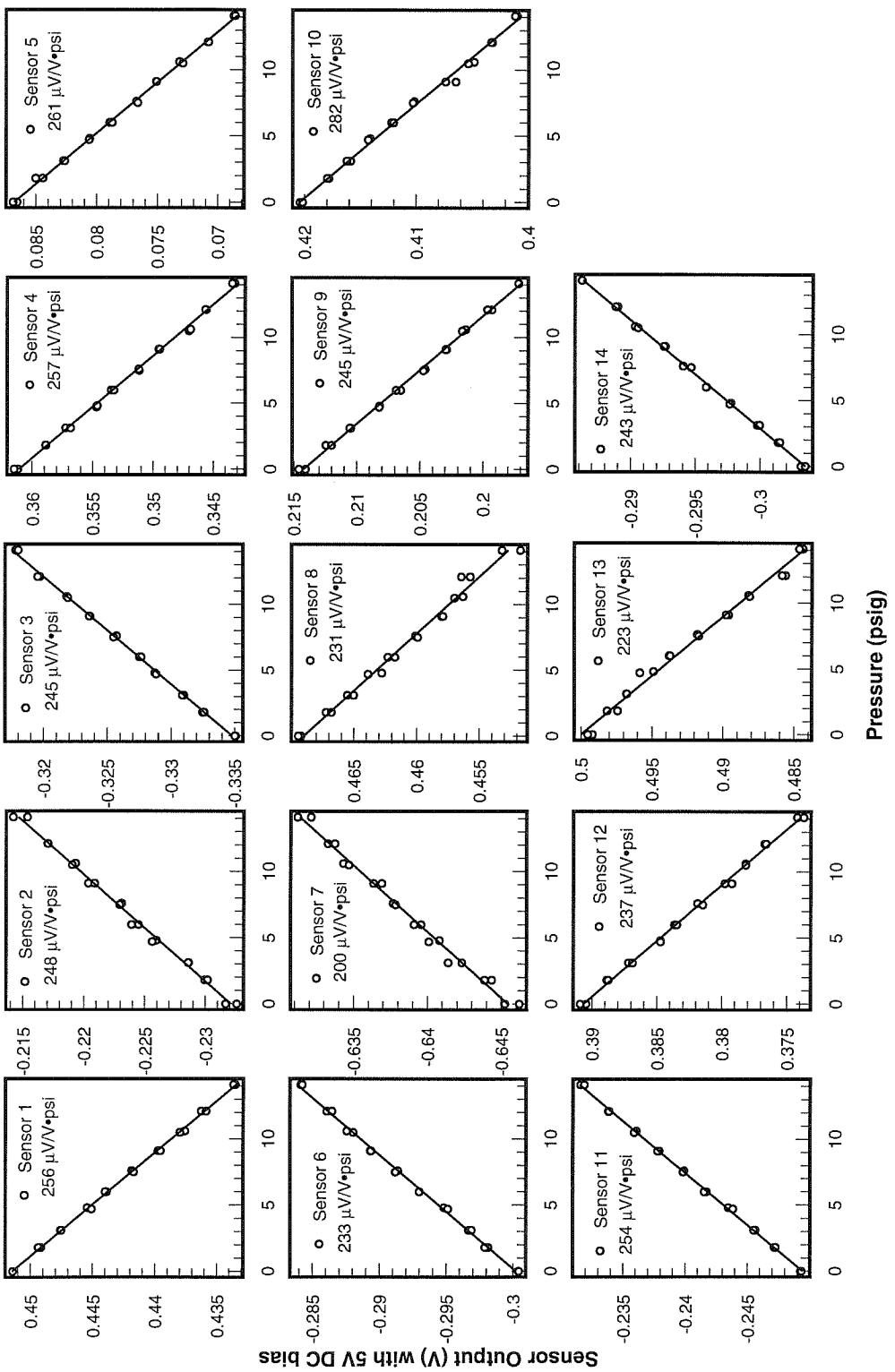

Figure 5.5: Calibrations of 14 pressure sensors in a non-uniform microchannel system.

5.3.2 Flow Rate Measurements

Since the flow rate of the microchannel is extremely small, it has to be measured using the accumulation method. Fig. 5.6 shows the measurement setup. In the setup, a serological pipette (Fig. 5.6) is used as the volume meter. One end of the pipette is connected directly to the outlet of the microflow system chip; the other end is open to atmosphere. During the measurement, a liquid droplet is first sucked into the pipette as the marker. When gas start to flow, the 'marker' also start to move. The gas volume flowing through the microchannel is monitored by the position of the 'marker'.

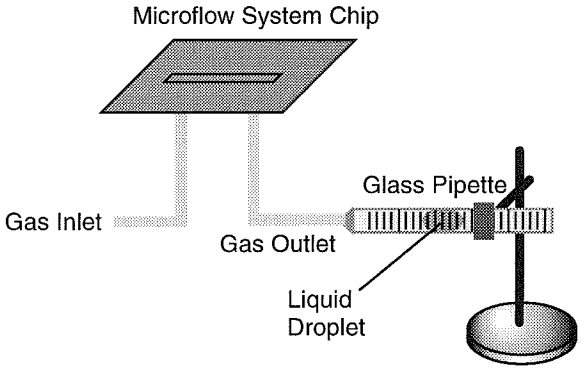

Figure 5.6: Schematics of the setup for the flow rate measurement.

Two factors which might have serious effects on the measurement are the gravitational force acted on the water droplet and surface tension between water and wall of the pipette. To avoid gravity effect on the measurements, the pipette has been carefully adjusted and maintained to stay in horizontal position during experiments. To study the surface tension effect, two different types of liquid droplets have been used in the pipettes. Fig. 5.7 shows the experimental results measured with water and (diffusion pump) oil as the 'mark'. The measurements are conducted with different pressure applied on the inlet of a microchannel system. To reduce the reading errors, two pipettes, one is 1 ml (10 μl/div with total 100 divisions) and the other is 0.1 ml (1 μl/div), are used. Results (Fig. 5.7) show the discrepancy is trivial when the inlet pressure is larger than about 15 psig, but significant (as much as 20%) when the inlet pressure is lower than 10 psig. Since the absolute

accuracy of the flow rate measurements is not the main subject here (a relationship between the pressure and flow rate is more of our interests), water droplets have been exclusively used in our measurement to keep the results consistent.

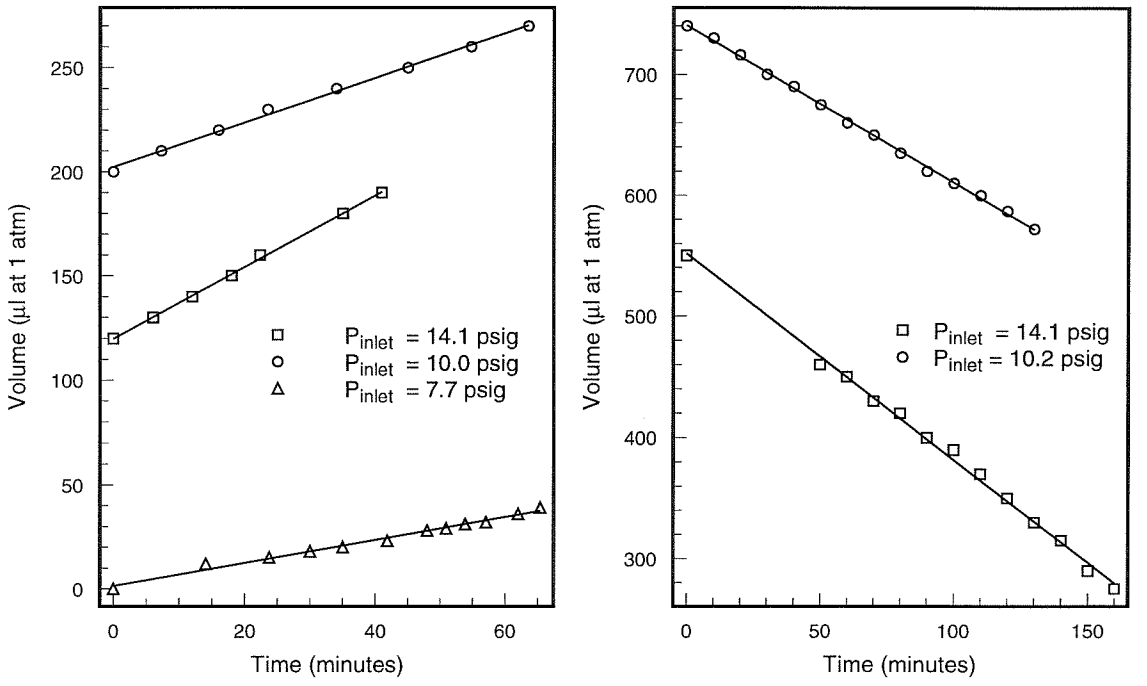

Figure 5.7: (a) Flow rate measured with water as the 'mark'. (b) Flow rate measured with diffusion pump oil as the 'mark'.

5.4 Results of Microflow Measurements

5.4.1 Uniform Microchannel with Four Pressure Sensors

Fig. 5.8 shows the pressure distribution measured with the first generation microchannel system chip (Fig. 4.3)[5]. In the plots, the dished lines are a direct link between the inlet pressure and the outlet pressure. Theoretically, they represent the model of an incompressible, laminar viscous flow with small Reynold numbers. The solid lines are a second order polynomial function fit to the experimental data. Obviously, the pressure distribution inside the microchannel is non-linear. As the inlet pressure increases, the deviation becomes more

pronounced. Another interesting phenomenon is the pressure distribution is very different for different gaseous flow. Fig. 5.8(b) shows the pressure distribution for nitrogen and helium gaseous flow. Since the Knudsen number for these two gases are very different (one is about 0.4, the other is about 0.04 at one atmosphere pressure), the difference might be attributed to the Kundsen number effect.

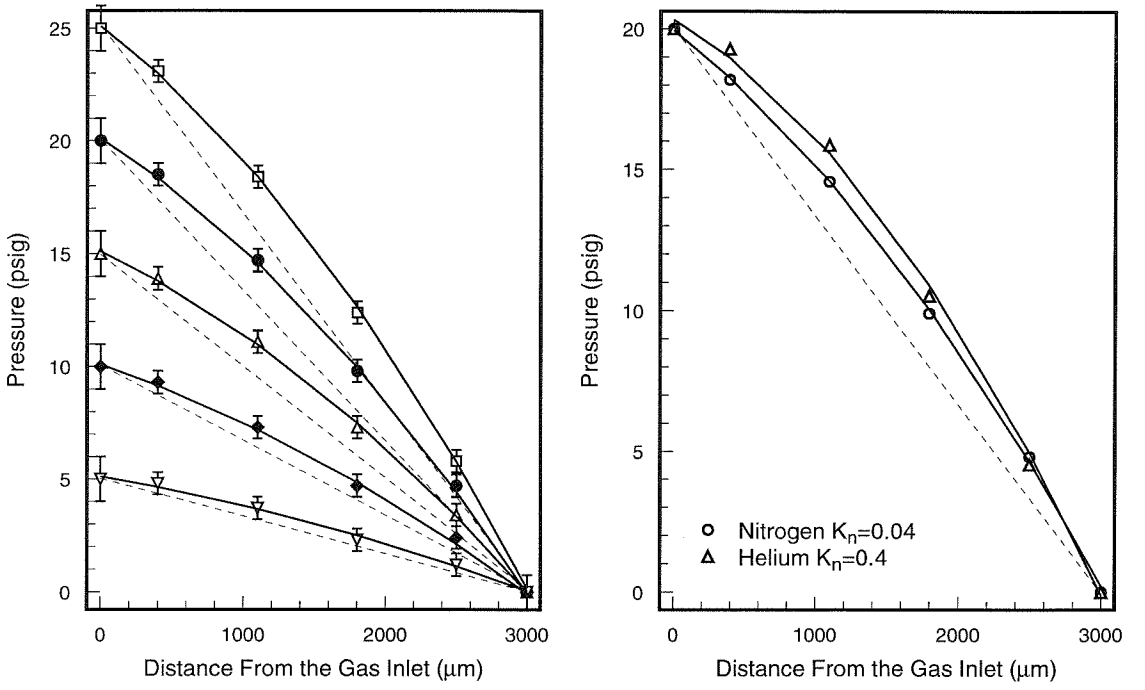

Figure 5.8: (a) Pressure distribution in a microchannel measured with the first generation microflow system. (b) Pressure distribution of different gas flow in a microchannel.

5.4.2 Uniform Microchannel with 13 Pressure Sensors

The nonlinear pressure distributions inside a uniform microchannel are also measured with the 13 sensors microchannel system. The design and layout of the second generation microflow system are presented in Chapter 4. Fig. 5.9 and 5.10 show two measurements of the pressure distribution inside a microchannel with 40×1.2 μm^2 of cross-section and 4.6 mm of length. The solid lines are a third order polynomial function modeling of the experimental data.

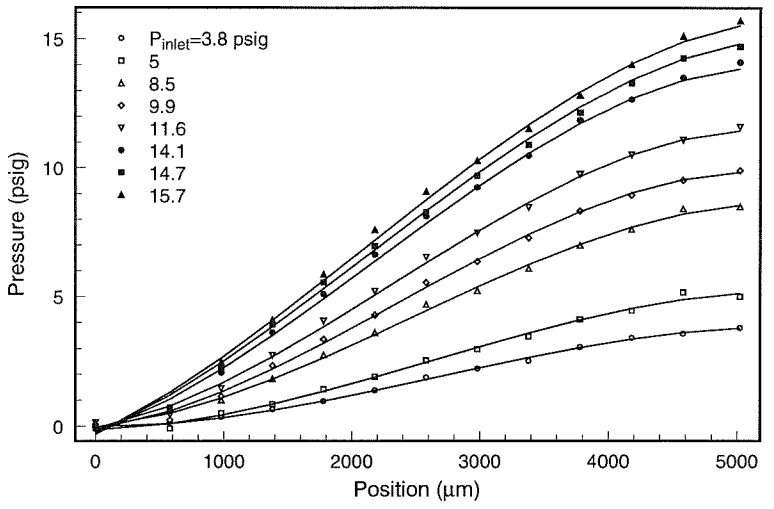

Figure 5.9: Microchannel pressure distribution measured with the second generation microflow system. The gas flows from right to left.

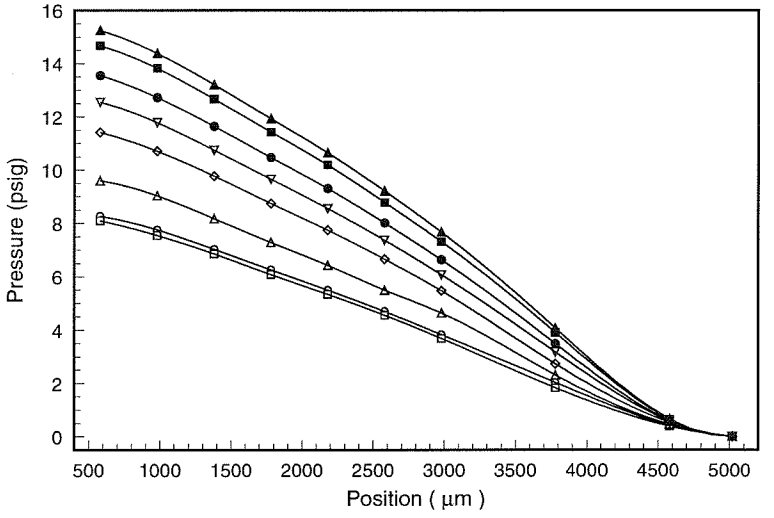

Figure 5.10: Microchannel pressure distribution measured with the second generation microflow system. The gas flows from left to right.

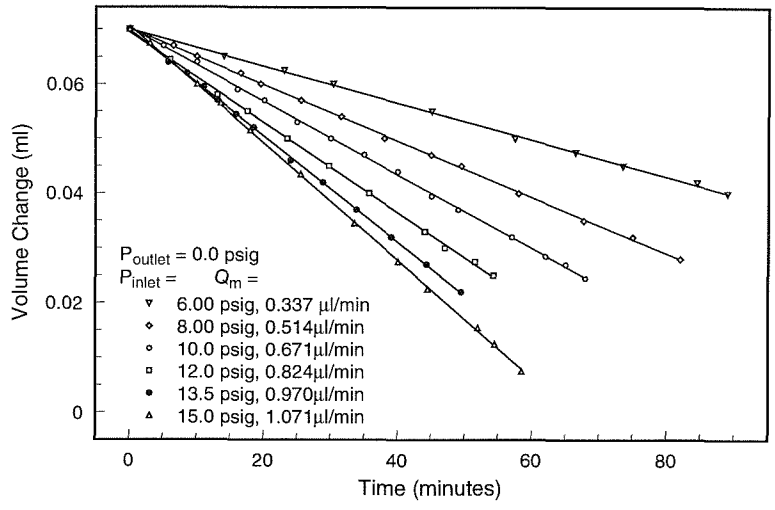

Figure 5.11: The flow rate as function of time for several different inlet pressures.

One interesting phenomenon was the pressure gradient at the entrance and the exit of the microchannel are smaller than that at the middle part. Interestingly, no simple theoretical model can explain this phenomenon.

5.4.3 Non-uniform Cross-Sectional Microchannel System

The design and layout of the non-uniform microchannel system is shown in Fig. 4.8. Measurement results are presented in Fig. 5.12 and 5.13. In terms of the measurement, the differences between the two figures are the total integration time for each are different. The first plot is an average of results measured in several days. The second plot is an average of results measured in one day. The reason for doing a long time average is to achieve maximum measurement accuracy since the pressure changes at the transitions (Fig. 5.12) are very small ($< 0.5psi$).

Two interesting phenomena are revealed from these results. First, there is clearly a non-trivial pressure drop across the first type micro-transition (transition 1 in Fig. 4.8). When the chip inlet pressure is about 20 psig, the drop is around 0.5 psig. This phenomenon can also be seen in Transition 3 when the flow is reversed. However, a quantitative relationship between the flow rate and the pressure drop is unable to be found since the noisy

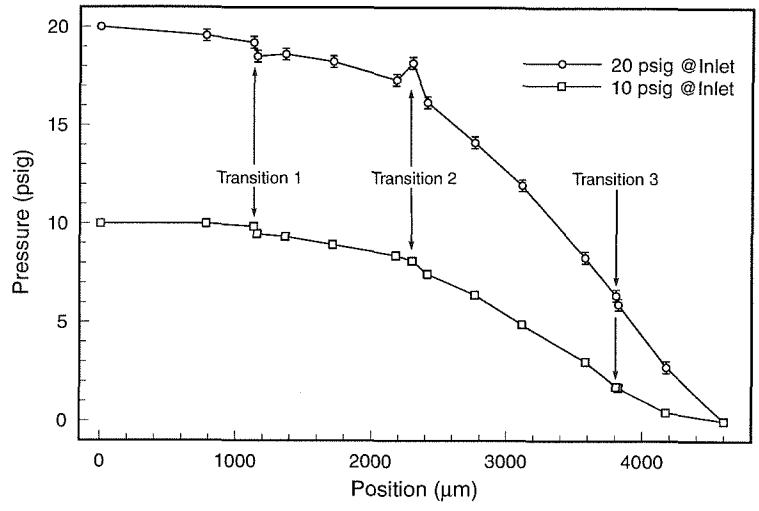

Figure 5.12: Pressure distribution along a non-uniform microchannel system. The data is averaged over several measurements spanning several days.

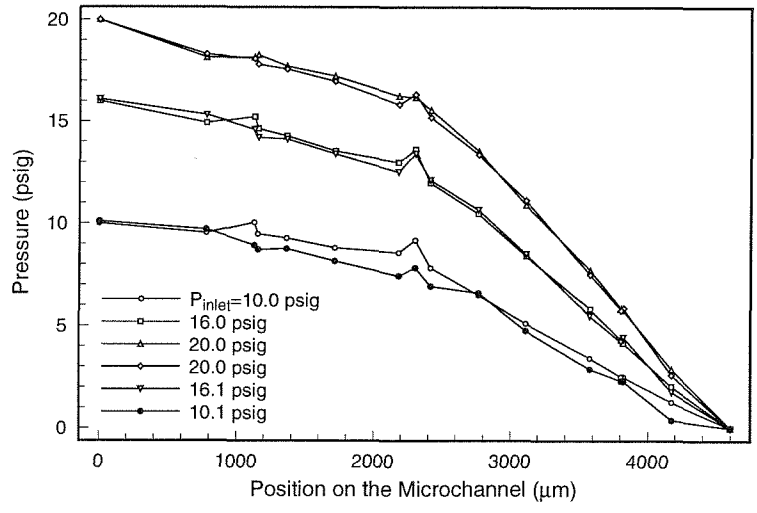

Figure 5.13: Pressure distribution in a non-uniform microchannel system.

measurements. Second, there is a definite pressure increase at the transition 2 when gas is flowing from left to right (from wide channel to narrow channel). The increases can be as big as 1 psig at least. If the flow direction is reversed, a pressure drop happens at the same position. These phenomena have never been observed experimentally before. Another interesting phenomenon is that the measured pressure fluctuations at the throat of the transition 1-3 are unusually larger than at the other places. This may not be attributed to defective sensors since this phenomenon is repeated on several chips. Because of this, a quantitative function between flow rate and the pressure change is hard to find.

5.5 Microchannel Flow Modeling

5.5.1 A Simple Model for Microchannel Flow

The Navier-Stokes equation can be written as

$$\frac{\partial \vec{\mathbf{v}}}{\partial t} + \vec{\mathbf{v}} \cdot \nabla \vec{\mathbf{v}} = -\frac{1}{\rho}\nabla p + \nu \nabla^2 \vec{\mathbf{v}} \tag{5.1}$$

For a steady viscous flow with small Reynold's number, the above equation can be further simplified as

$$\nabla p = \mu \nabla^2 \vec{\mathbf{v}} \tag{5.2}$$

The continuity equation and state equation for ideal gas can be written as

$$\nabla \cdot (\rho \mathbf{v}) = 0 \tag{5.3}$$

$$p = \rho k T \tag{5.4}$$

Eqs. (5.2), (5.3) and (5.4) are complete and can be solved if boundary conditions are given. To solve the problem, the Navier-Stokes equation can be rewritten in a cartesian coordinate system as

$$\begin{aligned} \frac{\partial p}{\partial x} &= \mu\Big(\frac{\partial^2 u}{\partial x^2} + \frac{\partial^2 u}{\partial y^2} + \frac{\partial^2 u}{\partial z^2}\Big) \\ \frac{\partial p}{\partial y} &= \mu\Big(\frac{\partial^2 v}{\partial x^2} + \frac{\partial^2 v}{\partial y^2} + \frac{\partial^2 v}{\partial z^2}\Big) \\ \frac{\partial p}{\partial z} &= \mu\Big(\frac{\partial^2 w}{\partial x^2} + \frac{\partial^2 w}{\partial y^2} + \frac{\partial^2 w}{\partial z^2}\Big) \end{aligned} \tag{5.5}$$

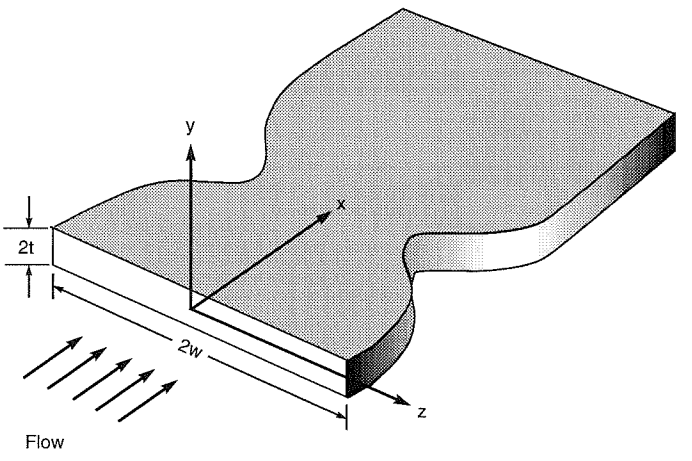

Figure 5.14: Coordinates used in our formula.

The coordinate system, as can be seen in Fig. 5.14, is arranged such that the x-axis is directed to the flow direction, the y-axis is directed upward relative to the surface. Since the height of the microchannel is much smaller than its width, the following relations exist:

$$\frac{\partial^2}{\partial y^2} \gg \frac{\partial^2}{\partial x^2}, \frac{\partial^2}{\partial z^2} \qquad \text{because} \qquad L_y \ll L_x, L_z \tag{5.6}$$

where L_x, L_y and L_z are characteristic sizes of the microchannel along three axes, respectively. Furthermore, assuming $v = 0$, the Navier-Stokes equation (Eq. (5.5)) become,

$$\begin{aligned} \frac{\partial p}{\partial x} &= \mu \frac{\partial^2 u}{\partial y^2} \\ \frac{\partial p}{\partial y} &= 0 \\ \frac{\partial p}{\partial z} &= \mu \frac{\partial^2 w}{\partial y^2} \end{aligned} \tag{5.7}$$

Eq. (5.7) leads to

$$p = p(x, z) \qquad \text{therefore} \qquad \rho = \rho(x, z) \tag{5.8}$$

From Eq. (5.7) and (5.3), it can be found that

$$\frac{\partial}{\partial x}\left(p\frac{\partial p}{\partial x}\right) + \frac{\partial}{\partial z}\left(p\frac{\partial p}{\partial z}\right) = 0 \tag{5.9}$$

Equation Eq. (5.9) may be solved using numerical methods if supplied with adequate boundary conditions. However, instead of finding the complete solution of Eq. (5.9), here the effort

will be concentrated on the pressure distribution along x-axis which can be found under certain circumstance without solving Eq. (5.9).

Since the pressure and density of the gas is only a function of x and z, Eq. (5.7) can be integrated along y axes; the results are

$$u = \frac{1}{2\mu}\left(\frac{\partial p}{\partial x}\right)y^2 + b_1 y + C_1 \tag{5.10}$$

$$w = \frac{1}{2\mu}\left(\frac{\partial p}{\partial z}\right)y^2 + b_2 y + C_2 \tag{5.11}$$

The velocity profile inside the microchannel has to be symmetrical around x-axis in y and z directions; that means $u(y) = u(-y)$ and $w(y) = w(-y)$; therefore, the constants b_1 and b_2 both must be zero.

The general expressions for slip boundary conditions are[6]

$$u(0) = \frac{2-\sigma}{\sigma}\bar{l}\left(\frac{\partial u}{\partial y}\right)_0 + \frac{3}{4}\frac{\mu}{\rho T}\left(\frac{\partial T}{\partial x}\right)_0 \tag{5.12}$$

$$T(0) - T_w = \frac{2-\alpha}{\alpha}\frac{2\gamma}{\gamma+1}\frac{\bar{l}}{P_r}\left(\frac{\partial T}{\partial y}\right)_0 \tag{5.13}$$

where $\bar{l}$ is the mean-free-path of the gas molecules, σ is the fraction of diffusely reflected molecules (whose average tangential velocity is thus zero) and $1-\sigma$ is the fraction of secularly reflected molecules (whose average tangential velocity is the same as that of the molecules incident from the layer a distance $\bar{l}$ above the wall). α is accommodation coefficient defined as

$$\alpha = \frac{dE_i - dE_r}{dE_i - dE_w}, \tag{5.14}$$

where dE_i and dE_r are respectively the energy fluxes incident on and re-emitted from a differential surface element per unit time. dE_w is the energy flux that would be carried away if all incident molecules were re-emitted with a Maxwellian distribution corresponding to the surface temperature T_w. The term α is thus a measure of the degree to which the molecules have their mean energy "accommodated" to what it would be if the returning molecules were issuing with energy dE_w.

In the following analysis, it is assumed that the whole flow system (including the fluid and the channel wall) is in thermal equilibrium, thus the temperature jump at the interface of the fluid and the channel wall is neglected. Therefore, in a local coordinate

system, the slip boundary condition for the velocity is expressed as

$$u(0) = \frac{2-\sigma}{\sigma}\,\bar{l}\,\frac{\partial u}{\partial y}\bigg|_{y=0} \tag{5.15}$$

where the y-axis is normal to the wall and directed to the fluid. In the global coordinate system (Fig. 5.14), the corresponding slip boundary conditions should be written as

$$u(-t) = \tfrac{2-\sigma}{\sigma}\,\bar{l}\,\tfrac{\partial u}{\partial y}\Big|_{y=-t} \tag{5.16}$$

$$u(t) = -\tfrac{2-\sigma}{\sigma}\,\bar{l}\,\tfrac{\partial u}{\partial y}\Big|_{y=t} \tag{5.17}$$

After applying boundary conditions (Eq. 5.17) to Eq. (5.11), the final solutions for a slip flow are

$$u = \frac{1}{2\mu}\Big(\frac{\partial p}{\partial x}\Big)(y^2 - C\,t^2) \tag{5.18}$$

$$w = \frac{1}{2\mu}\Big(\frac{\partial p}{\partial z}\Big)(y^2 - C\,t^2) \tag{5.19}$$

in which

$$C = 1 + 2K_n\frac{2-\sigma}{\sigma} \tag{5.20}$$

where $K_n = \frac{\bar{l}}{t}$ is the Knudsen number. In the continuous flow regime where $K_n \ll 1$, the correction constant is $C = 1$ which represents the non-slip boundary condition with zero velocity on the wall. In general, the correction coefficient C is not a constant. Since the mean-free-path of the gas depends upon its density, the Knudsen inside the microchannel is not a constant. Especially when the pressure difference between two ends of the microchannel is large, the Knudsen number changes significantly from the inlet to outlet of the microchannel.

The pressure distribution along the microchannel can be solved using the integral form of the continuity equation which can be written as

$$\iint \rho\mathbf{v}\cdot d\mathbf{S} = Q_m. \tag{5.21}$$

Let $d\mathbf{S}$ direct to the x-axis direction; the above equation is then written as

$$\int_{-a(x)}^{a(x)} dz \int_{-t}^{t} \rho(x,z)u(x,y,z)\,dy = Q_m \tag{5.22}$$

where $2t$ is height of the microchannel (Fig. 5.14), and $2a(x)$ is the width of the channel. Insert Eq. (5.18) into Eq. (5.22) and integrate along y-axis; the result is

$$\frac{1}{2\mu RT}\int_{-a(x)}^{a(x)}\left(\frac{2}{3}t^3 - 2C\,t^3\right)p\left(\frac{\partial p}{\partial x}\right)dz = Q_m \tag{5.23}$$

or

$$\int_{-a(x)}^{a(x)} p\left(\frac{\partial p}{\partial x}\right)\left(\frac{1}{3} - C\right)dz = \frac{\mu RTQ_m}{t^3} \tag{5.24}$$

5.5.2 Microchannels with Uniform Cross-Sectional Area

For a straight uniform cross-sectional microchannel where a is a constant, it is reasonable to assume the gas density, ρ, is only a function of x. Therefore, from Eq. (5.4), the pressure is only a function of x too, $p = p(x)$. The pressure distribution along the channel can be written as (from Eq. (5.24))

$$p\frac{dp(x)}{dx}\left(\frac{1}{3} - C\right) = \frac{\mu RTQ_m}{2at^3} \tag{5.25}$$

This equation can not be integrated directly because the mean-free-path is a function of the gas pressure,

$$\bar{l} \propto \frac{1}{\rho} \propto \frac{1}{p} \tag{5.26}$$

The Knudsen number can be written as

$$K_n(x) = K_{no}\frac{p_o}{p(x)} \tag{5.27}$$

where K_{no} is the Knudsen number at the outlet of the microchannel, p_o is the outlet pressure. Using Eq. (5.20) and (5.27), one finally gets

$$p\frac{dp}{dx}\left(\frac{1}{3} + K_{no}\frac{2-\sigma}{\sigma}\frac{p_o}{p}\right) = -\frac{\mu RTQ_m}{4at^3} \tag{5.28}$$

A solution of pressure distribution can be found by integrating both sides of the above equation. The result is

$$p = p_o\left[(C_1+1)^2 + C_2(1-x)\right]^{1/2} - C_1 p_o \tag{5.29}$$

where

$$C_1 = 3K_{no}\frac{2-\sigma}{\sigma} \tag{5.30}$$

$$C_2 = \frac{3\mu RTLQ_m}{2at^3p_o^2} \tag{5.31}$$

For a continuous flow in which K_{no} is very small, C_1 is very small, and the pressure will be proportional to $\sqrt{1 + C_2(1-x)}$. Let the pressure at the inlet of the microchannel be p_i, then the mass flow rate of the microchannel can be derived from the above equation. The result is

$$Q_m = \frac{2at^3 p_o^2}{3\mu RTL}\left[\left(\frac{p_i}{p_o}\right)^2 - 1 + 6K_{no}\frac{2-\sigma}{\sigma}\left(\frac{p_i}{p_o} - 1\right)\right] \tag{5.32}$$

These formula have also been derived by Arkilic et al.[3] with a different approach. Fig. 5.15 shows the normalized pressure distribution along a microchannel calculated from Eq. (5.29) for several different specular reflection coefficients. As σ decreases (less molecules are diffusely reflected from the wall), the curve becomes more linear. Similar curves with different Knudsen numbers are shown in Fig. 5.16. Fig. 5.17 shows the normalized mass flow rate for gases with different Knudsen numbers. As one can see, the flow rate increases as the Knudsen number increases. For large Knudsen numbers, the gas flow rate can be significantly larger than that of a non-slip gas flow.

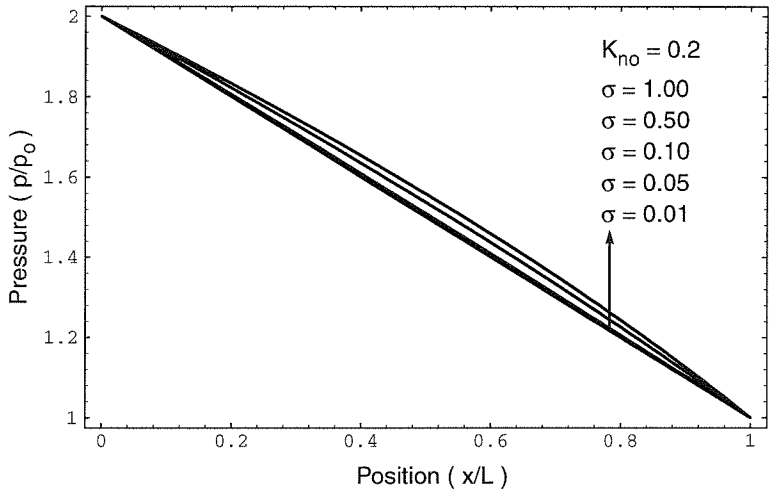

Figure 5.15: The pressure distribution $(p(x)/p_o)$ along a microchannel for various σ values.

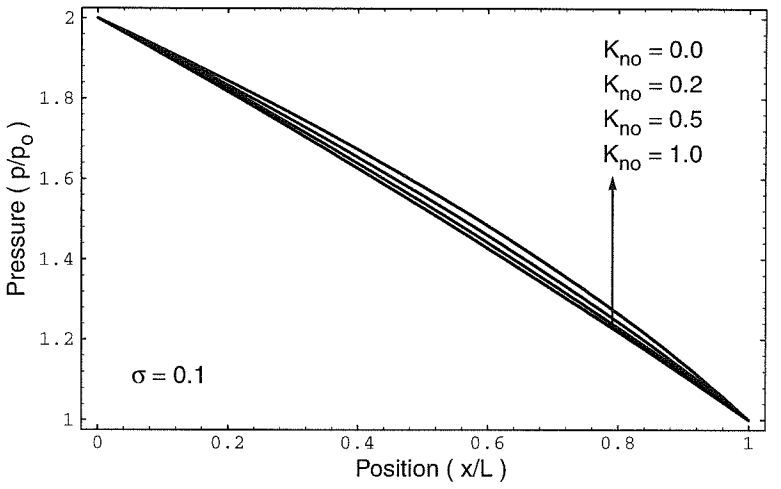

Figure 5.16: The pressure distribution $(p(x)/p_o)$ along a microchannel for various K_{no} values.

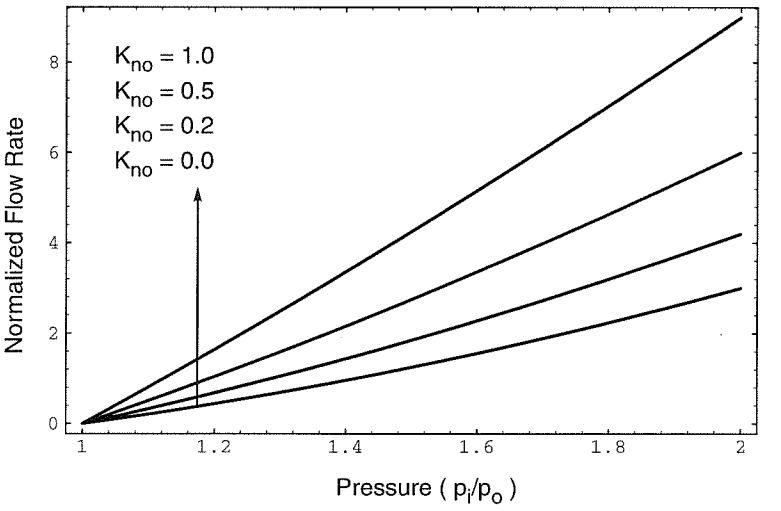

Figure 5.17: The normalized mass flow rate, $Q_m/\left(\frac{4at^3p_o}{3\nu L}\right)$, as a function of inlet/outlet pressure ratio.

5.6 Discussion of Modeling Experimental Results

5.6.1 Uniform Cross-Sectional Microchannels

Flow Rate

The measured flow rate as a function of the ratio of inlet-to-outlet pressure is shown in Fig. 5.18 along with a fit with the theoretical model, Eq. (5.32). As shown, the experimental results can fit nicely with the theoretical model if the following parameters are used:

$$C_1 = 3K_{no}\frac{2-\sigma}{\sigma} = 0.318 \tag{5.33}$$

$$C_2 = \frac{3\mu RTLQ_m}{2at^3p_o^2} = Q_m/0.292 \tag{5.34}$$

If σ=1, then the Knudsen number K_{no}=0.106 which is lower than that used by Arkilic et al.[3].

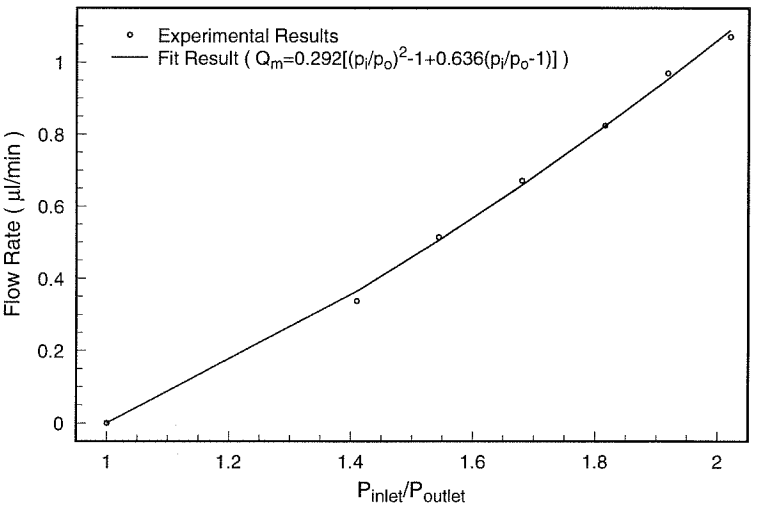

Figure 5.18: The measured flow rate for the second generation microflow system and a fit with the theoretical model (Eq. (5.32)).

Pressure Distribution

The measured pressure distribution along a microchannel in the second generation microflow system shows some interesting patterns. First, the gradient at the entrance is smaller than

that at the middle section. Second, the gradient at the exit is also smaller as at the entrance. However, such a 'tail' (the small gradient near the exit of the microchannel) can not be seen in the measurements with the first generation microflow system (Fig. 5.8). The difference of the measured pressure distribution between the first and the second generation microflow systems may be an artificial effect due to the spline function fitting of the data (Fig. 5.8) and lack of points along the microchannel. To compare with the theoretical model, it is necessary to exclude any of these 'end' effects. Indeed, if we ignore the first and the last point in Fig. 5.9, the pressure distribution measured with the second generation microflow system can actually be modeled nicely with the Eq. (5.29). The results is shown in Fig. 5.19.

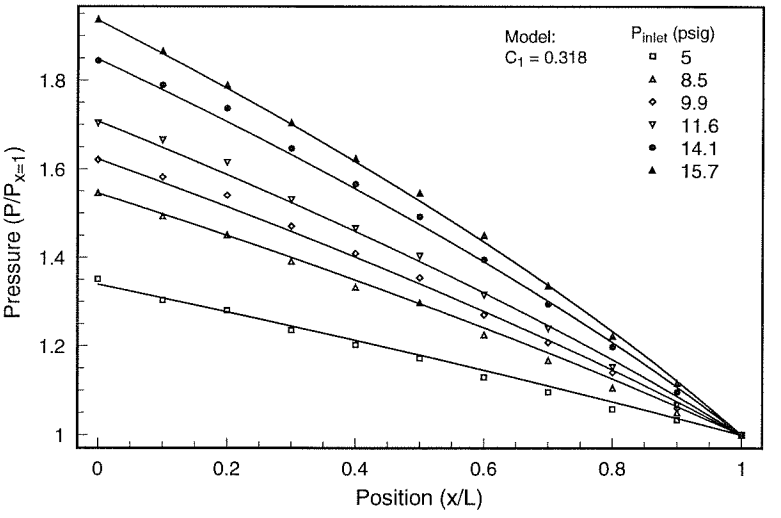

Figure 5.19: Experimental results (marks) with theoretical modeling (solid lines) for the second generation microflow system (uniform cross-section microchannel).

The parameter of C_1 used in the model is from the fit results of gas flow rate measurements, namely 0.318 for C_1. To compare with the model, the experimental results is normalized. The origin of the x axis is at the position of the first pressure on the microchannel (not the sensor on the inlet diaphragm). The last point (x=1) is at the position of the last sensor on the microchannel (the 11th sensor). The length of the channel is 4 mm (between the first and the last pressure sensors on the channel). Therefore, the entrance and exit of the microchannel is excluded from the modeling. The pressure is

normalized to that at the last point. The ratio of the pressure, p_i/p_o, is calculated from the ratio of $p_{x=0}/p_{x=1}$. Using the C_1 (=0.318) and the $p_{x=0}/p_{x=1}$, curves of theoretical model can be calculated according to Eq. (5.29). The results in Fig. 5.19 show the theoretical model fit nicely the experimental data. The small deviation between the model and the experimental data may be attributed to experimental errors.

An interesting phenomenon can be found by comparing Fig. 5.15 and 5.16 with Fig. 5.8. The pressure distribution in Fig. 5.8 shows more nonlinearity for the helium gas flow than for the nitrogen. According to the model, the smaller C_1 is, the larger nonlinearity the curve shows. Therefore, the helium gas should have a smaller C_1 value than nitrogen. However, since the Knudsen number of helium gas is almost one order of magnitude larger than that of nitrogen gas, the specular reflection coefficient for the two gases must be very different. Or in other words, the nitrogen should have smaller σ. Physically it means the nitrogen molecules are more secularly reflected from the channel wall.

5.7 Summary

A complete microflow experimental setup has been installed. This system includes the microchannel system chip, gas supply and flow control system and a data acquisition system. Preliminarily gas flow experiments have been carried out. For the first time, it is experimentally found that the pressure distribution inside a uniform cross-section microchannel is nonlinear. Furthermore, the pressure gradient in the middle of the channel is larger than those at the entrance and the exit. The nonlinearity of the pressure distribution is different for different gases (with different viscosity and Knudsen numbers). For channels with varying widths, there is a non-trivial pressure change across a Venturi-meter-like microchannel. The pressure at the throat is lower than the pressure at the entrance and the exit for the transition 1 and 3. An appreciable pressure increase can be seen in a long contraction microchannel (transition 2). Pressure measured at these transitions show larger fluctuations than at the section of the microchannel with uniform cross-sectional area. The pressure distribution along a microchannel with uniform cross-sectional area has been modeled with an isothermal, viscous flow model with slip-flow boundary conditions. According to this model, the specular reflection coefficient of helium is different from that of nitrogen.

model, the specular reflection coefficient of helium is different from that of nitrogen.

Bibliography

[1] J. Pfahler, J. Harley, and H. Bau, "Gas and liquid flow in small channels," in *Micromechanical Sensors, Actuators, and Systems*, vol. 32, pp. 49–60, ASME, 1991.

[2] S. B. Choi, R. F. Barron, and R. O. Warrington, "Fluid flow and heat transfer in microtubes," in *Micromechanical Sensors, Actuators, and Systems*, vol. 32, pp. 123–134, ASME, 1991.

[3] E. B. Arkilic, K. S. Breuer, and M. A. Schmidt, "Gaseous flow in microchannels," in *Application of Microfabrication to Fluid Mechanics 1994, International Mechanical Engineering Congress and Exposition* (P. R. Bandyopadhyay, K. S. Breuer, and C. J. Blechinger, eds.), vol. 197, (Chicago, Illinois), pp. 57–66, Academic Press, November 1994.

[4] W. H. Press, B. P. Flannery, S. A. Teukoisky, and W. T. Vetterling, *Numerical Recipes, The Art of Scientific Computing [FORTRAN Version]*, ch. 14, p. 521. Cambridge, 1989.

[5] J. Liu, Y.-C. Tai, K.-C. Pong, and C.-M. Ho, "Micromachined channel/pressure sensor systems for microflow studies," in *The 7th International Conference on Solid-State Sensors and Actuators, Transducers' 93*, (Yokohama, Japan), pp. 995–997, June 1993.

[6] E. H. Kennard, *Kinetic Theory of Gases.* McGraw-Hill, 1938.

Appendix A

Fabrication Process for Micro Devices

Standard Wafer Cleaning Process

1. Wafer pre-cleaning with Aceton, alcohol and water if there is photoresist on the wafer.
2. Heat Piranha (H_2SO_4:H_2O_2=5:1) to 120 °C.
3. Put the wafer into piranha tank for 10 minutes.
4. Rinse the wafer with DI water until the water resistant is less than 10 MΩ.
5. Spin dry the wafer.

Standard Photolithograph Process

1. Standard wafer clean.
2. HMDS vapor priming for 2 minutes.
3. Spin coat photoresist (the spin speed and photoresist depend upon the device fabrication requirements).
4. Soft bake photoresist in a convection oven at 90 °C for 10 minutes.

5. Expose the mask with GCA 4800 stepper (10×reduction) (exposure time depends upon the thickness of photoresist).

6. Develop photoresist for 2 minutes.

7. Spin dry the wafer.

8. Hard bake the wafer for 30 minutes at 120 °C (in the same convection oven).

A.1 Microchannel Fabrication

1. Wafer Cleaning

   Perform standard wafer cleaning process.

   Dip wafer in diluted HF (5 wt.%) for 1 minute to remove native oxide.

2. PSG Deposition

   Deposit PSG 1.0 μm (the standard LPCVD PSG recipe).

3. PSG Annealing

   Anneal the PSG film at 1000 °C for 40 minutes in N_2 ambient.

4. PSG Patterning

   Perform standard photolithograph procedure with mask No. 1 (KTI 100CS, 2.0 krpm, exposure time 0.7 seconds).

   Etch PSG in Buffered HF solution.

   Rinse in DI water and spin dry.

5. Wafer Cleaning

   Perform standard wafer cleaning procedure.

   Dip wafer in diluted HF (5 wt.%) no longer than 5 seconds.

   Rinse wafer and spin dry.

6. LPCVD Silicon Nitride Deposition

   Perform standard low-stress silicon nitride deposition (1.5 μm).

7. Pattern Etching Holes

   Perform standard photolithograph procedure (KTI 100CS, spin speed 2.5 krpm, photoresist 3.0 μm, exposure time 0.7 seconds).

   Use SF_6 plasma (in PE IIA) to etching silicon nitride down to PSG layer.

   Perform standard wafer cleaning procedure.

8. Etching Sacrificial PSG Layer

   Etch sacrificial PSG through the etching holes (use 49 wt.% HF). Time is dependent on the etching length.

9. Rinse and Dry

   Rinse in water for 40-60 minutes and spin dry in a vacuum spin dryer.

A.2 The 1st Generation Microflow Measurements System

1. Wafer Cleaning

   Perform standard wafer cleaning procedure.

   Dip wafer in diluted HF solution (5 wt.%) to remove the native oxide.

   Spin dry the wafer.

2. Low Stress Nitride Deposition

   Perform standard low-stress silicon nitride deposition.

   (Deposition time is 18 minutes and target thickness 100-150 nm.)

3. Photolithography With Mask #1

   Clean the wafer using the standard procedure.

   Perform standard photolithograph procedure.

   (KTI 100CS, spin 2.5 μm photoresist at speed 3.0 krpm; exposure time 0.6 sec)

4. Descum

   Use O_2 plasma to clean the wafer.

   (Plasma Etcher II, 50 W, chamber pressure 250 mtorr, etch 5 minutes.)

5. Nitride and Silicon Etching

   Use Plasma Etcher IIA to etch silicon nitride.

   (400 W power, SF_6 gas, 180 mtorr chamber pressure.)

   Time control: etch 30 seconds, rotate wafer 180 degree, etch 30 seconds, and rotate 180 degree until silicon nitride is etched through, and silicon is also etched down 600 nm.

6. Photoresist Remove

   Use O_2 plasma to etch photoresist.

   (PE IIA, 350 W, O_2 pressure in chamber is 300 mtorr.)

7. Wet Oxidation

   Perform standard wafer cleaning.

   Dip wafer in diluted HF (5 wt.%) for 1 minutes.

   Perform wet oxidation (1050 °C) for about 3.5 hours. Target thickness is 1 μm .

8. Nitride Stripe

   Remove silicon nitride with H_3PO_4 (160-180 °C)

   (about 100 A/min etching silicon nitride. $\tilde{1}0$ Å/min etching oxide).

   Rinse in DI water (30 minutes).

9. LPCVD PSG Deposition

   Perform standard wafer cleaning followed by 5% HF dip.

   Deposit standard LPCVD PSG (6wt.%) 300 nm (18 minutes).

10. PSG Annealing

    Anneal the PSG film at 1050 °C for 40 minutes.

    (N_2 environment, using the annealing furnace.)

11. Photolithography With Mask #2

    Perform standard photolithograph procedure.

    (KTI 27CS, spin coat 1 micron, exposure time 0.2-0.3 seconds.)

12. PSG Patterning

    Etch PSG with buffered HF (5:1).

13. Photoresist Remove

    Clean wafer with aceton, alcohol and water spray.

    Perform standard wafer cleaning in piranha tank.

14. PSG Reflow

    Reflow the PSG film in an N_2 environment.

    (1050 °C, 40 minutes.)

15. Low Stress Nitride Deposition

    Perform 5 wt.% HF dip to remove thin oxide (<3 seconds).

    Deposit low-stress silicon nitride 1.2-1.4 μm.

    (Setting/flow rate is 219/42.0 for DCS, 120/120 for NH_3; temperature is set to 835 °C; deposition time is 180 minutes.)

16. LPCVD Poly-silicon Deposition

    Deposit standard LPCVD polysilicon 300 nm.

17. Boron Diffusion

    Do 5% HF dip before putting into furnace. Diffuse boron into polysilicon (performed in boron furnace at 950 °C for 30 minutes).

18. Photolithography with Mask #3

    Perform standard photolithography procedure.

    (KTI100cs, spin speed 3.0 krpm, photoresist 3.0 μm .)

19. Poly-silicon Etching

    Perform descum first.

    Etch polysilicon with PE IIA (400W, 180 mtorr SF_6 gas).

20. Photoresist Remove

    Do plasma ashing.

    Perform standard piranha cleaning (right tank).

21. Boron Oxide Striping

    Dip wafer in 5 wt.% HF (diluted from 49 wt.% HF) for 5 minutes.

    Perform standard piranha cleaning.

22. Low Stress Nitride Deposition

    Deposit low-stress silicon nitride 0.4-0.5 μm (50 minutes).

23. Photolithography with Mask #4

    Do standard wafer cleaning.

    Perform standard photolithography on the backside of the wafer with mask #4.

    (KTI 100CS, spin coat 4.0 μm photoresist at 2.0 krpm.)

24. Back Side Nitride Etching

    Etch silicon nitride with SF_6 plasma in PE IIA.

    (400 W, 180 mtorr chamber pressure.)

25. Photoresist Remove

    Do plasma ashing followed by standard piranha cleaning.

26. Silicon Substrate Etching

    Etch silicon in EDP (8-12 hours) until the wafer is etched through.

    (95 °C, 250 rpm stir in a reflux system.)

    Rinse wafer in boiled water.

    Rinse wafer in DI water (10 minutes).

    Perform standard piranha cleaning.

27. Photolithography with Mask #5

    Perform standard photolithography procedure with mask #5.

    (KTI 100CS, spin speed 3.0 krpm, photoresist 3.5 μm. Use special chuck to hole wafer during photoresist spin coat.)

28. Nitride Etching

    Etch silicon nitride down 300 nm.

    (PE IIA, 400 W, 180 mtorr).

Etch silicon nitride down to polysilicon.

(PE II, CF_4 gas, 200 W, 200 mtorr).

29. Photoresist Remove

    Perform the standard photoresist remove procedure.

30. Photolithography with Mask #6

    Perform standard photolithography procedure.

    (KTI 100CS, 2.0 krpm, photoresist thickness 4.0 μm .)

31. Nitride Etching

    Etch silicon nitride down to PSG film.

    (PE IIA, 400 W, 180 mtorr SF_6.)

32. Photoresist Remove

    Do wafer clean with acetone, alcohol and DI water.

    Ash photoresist in O_2 plasma.

33. PSG Etching in HF

    Use 49 wt.% HF to etch sacrificial PSG layer (25 minutes).

    Rinse in DI water and spin dry.

    Check under microscope if channel and sensor chamber are etched through.

    (If not, etch another 10 minutes.)

    DI water rinse no less than 60 minutes.

    Spin dry in a vacuum spin dryer and bake wafer in annealing furnace.

    (600 °C for 30 minutes.)

34. PECVD Oxynitride Deposition

    Use PECVD system to deposit oxynitride 1.2 μm.

    (Standard oxynitride recipe, deposition time 60 minutes.)

    Check sealing.

    (If pressure sensor chambers are not sealed, deposit another 30 minutes.)

35. Photolithography with Mask #7

    Perform standard photolithography procedure with mask #7.

    (KTI 100CS, speed 3.5 krpm, photoresist 3.0 μm).

    (Protect back side of wafer with blue tape before developing photoresist; stripe blue tape before hard bake.)

36. Oxynitride Pattern

    Do descum first and then protect back side of wafer with blue tape.

    Use buffered HF to etch oxynitride.

    (10% over etch to ensure oxynitride is etching away anywhere on the wafer.)

37. Photoresist Remove

    Clean with acetone, alcohol and DI water and spin dry.

    Peel off the blue tape carefully.

    Perform plasma ashing.

    Protect the backside with blue tape.

    Dip in diluted (5%) HF for 2 minutes (remove native oxide).

    DI water rinse till water resistivity >12 MW and spin dry.

    Peel off the blue tape.

38. Aluminum Evaporation

    Evaporate 1.0 μm aluminum (E-beam or thermal evaporator).

39. Photolithography with Mask #8

    Perform standard photolithograph procedure with mask #8.

    (KTI 27CS, 3.5 krpm, 1.2 μm.)

    (Protect the backside of the wafer with blue tape before developing and peel it off before hard bake.)

40. Aluminum Etching

    Perform descum first and protect backside with blue tape.

    Etch aluminum with aluminum etchant (50 °C, 2 minutes).

    Peel off the blue tape and do plasma ashing to remove photoresist.

41. Aluminum Sintering

    Sinter aluminum in metal annealing furnace.

    (450 °C for 45 minutes, N_2 ambient.)

42. Wafer Dicing

    Spin on photoresist (KTI 100CS, 2.0 krpm, 4 μm) and do hard bake 30 minutes at 120 °C.

    Dice wafer (1×1 cm^2, cut depth 350 μm (150 μm left)).

    After stripping blue tape, do plasma ashing to finally clean wafer.

A.3 The 2nd Generation Microflow Measurements System

1. Wafer Cleaning

   Perform standard wafer cleaning procedure.

   Dip wafer in diluted HF solution (5 wt.%) to remove the native oxide.

   Spin dry the wafer.

2. Low Stress Nitride Deposition

   Perform standard low-stress silicon nitride deposition. (Deposition time is 18 minutes and target thickness, 100-150 nm.)

3. Photolithography With Mask #1

   Clean the wafer using the standard procedure.

   Perform standard photolithograph procedure.

   (KTI 100CS, spin 2.5 μm photoresist at speed 3.0 krpm; exposure time 0.6 sec.)

4. Descum

   Use O_2 plasma to clean the wafer.

   (Plasma Etcher II, 50 W, chamber pressure 250 mtorr, etch 5 minutes.)

5. Nitride and Silicon Etching

   Use Plasma Etcher IIA to etch silicon nitride.

   (400 W power, SF_6 gas, 180 mtorr chamber pressure.)

Time control: etch 30 seconds, rotate wafer 180 degree, etch 30 seconds, and rotate 180 degree until silicon nitride is etched through and silicon is also etched down 600 nm.)

6. Photoresist Remove

   Use O_2 plasma to etch photoresist.

   (PE IIA, 350 W, O_2 pressure in chamber is 300 mtorr.)

7. Wet Oxidation

   Perform standard wafer cleaning.

   Dip wafer in diluted HF (5 wt.%) for 1 minute.

   Perform wet oxidation (1050 °C) for about 3.5 hours. Target thickness is 1 μm.

8. Nitride Stripe

   Remove silicon nitride with H_3PO_4 (160-180 °C) (about 100 A/min etching silicon nitride, 10 Å/min etching oxide).

   Rinse in DI water (30 minutes).

9. LPCVD PSG Deposition

   Perform standard wafer cleaning followed by 5% HF dip.

   Deposit standard LPCVD PSG (6wt.%) 300 nm (18 minutes).

10. PSG Annealing

    Anneal the PSG film at 1050 °C for 40 minutes.

    (N_2 environment, using the annealing furnace.)

11. Photolithography With Mask #2

    Perform standard photolithograph procedure.

    (KTI 27CS, spin coat 1 micron, exposure time 0.2-0.3 seconds.)

12. PSG Patterning

    Etch PSG with buffered HF (5:1).

13. Photoresist Remove

    Clean wafer with aceton, alcohol and water spray.

Perform standard wafer cleaning in piranha tank.

14. PSG Reflow

    Reflow the PSG film in a N_2 environment.

    (1050 °C, 40 minutes).

15. Low Stress Nitride Deposition

    Perform 5 wt.% HF dip to remove thin oxide (<3 seconds).

    Deposit low-stress silicon nitride 1.2-1.4 μm (setting/flow rate is 219/42.0 for DCS, 120/120 for NH_3; temperature is set to 835 °C; deposition time is 180 minutes).

16. LPCVD α-silicon Deposition

    Deposit LPCVD α-silicon 300 nm.

    (Standard procedure but set temperature to 580 °C.)

17. Boron Ion Implantation

    Dope polysilicon with ion implantation.

    (Dose 5×10^{16} cm^{-2}.)

18. Photolithography with Mask #3

    Perform standard photolithography procedure.

    (KTI100cs, spin speed 3.0 krpm, photoresist 3.0 μm.)

19. Boron Ion Implantation

    Dope polysilicon with ion implantation method.

    (Dose 10^{20} cm^{-2}. Run water cooling on the wafer substrate during ion implantation.)

20. Photoresist Remove

    Do O_2 plasma ashing.

    Perform standard wafer clean procedure (piranha cleaning).

21. α-silicon Annealing and Dopant Activation

    Anneal α-silicon and convert it to polysilicon.

    (950 °C for 30 minutes in annealing furnace.)

22. Photolithography with Mask #4

    Perform standard photolithography process with mask #4.

    (KTI 100CS, spin speed 3.0 krpm, photoresist 3.0 μm.)

23. Poly-silicon Etching

    Perform wafer descum.

    Etch polysilicon with PE IIA (400W, 180 mtorr SF_6 gas).

24. Photoresist Remove

    Do plasma ashing.

    Perform standard piranha cleaning (right tank).

25. Low Stress Nitride Deposition

    Dip wafer in 5 wt.% HF (diluted from 49 wt.% HF) for 5 minutes.

    Deposit low-stress silicon nitride 0.4-0.5 μm (50 minutes).

26. Photolithography with Mask #5

    Do standard wafer cleaning.

    Perform standard photolithography on the backside of the wafer with mask #5.

    (KTI 100CS, spin coat 4.0 μm photoresist at 2.0 krpm.)

27. Back Side Nitride Etching

    Etch silicon nitride with SF_6 plasma in PE IIA.

    (400 W, 180 mtorr chamber pressure.)

28. Photoresist Remove

    Do plasma ashing followed by standard piranha cleaning.

29. Photolithography with Mask #6

    Perform standard photolithography procedure to pattern front etching holes.

    (KTI 100CS, 2.0 krpm, photoresist thickness 4.0 μm)

30. Nitride Etching

    Etch silicon nitride down to PSG film.

    (PE IIA, 400 W, 180 mtorr SF_6.)

31. Photoresist Remove

    Do wafer cleaning with acetone, alcohol and DI water.

    Ash photoresist in O_2 plasma.

32. Silicon Substrate Etching

    Etch silicon in EDP (8-12 hours) until the wafer is etched through.

    (95 °C, 250 rpm stir in a reflux system.)

    Rinse wafer in boiled water.

    Rinse wafer in DI water (10 minutes).

    Perform standard piranha cleaning.

33. Photolithography with Mask #7

    Perform standard photolithography procedure to pattern contact windows.

    (KTI 100CS, spin speed 3.0 krpm, photoresist 3.5 μm. Use special chuck to hole wafer during photoresist spin coat.)

34. Nitride Etching

    Etch silicon nitride down 300 nm.

    (PE IIA, 400 W, 180 mtorr).

    Etch silicon nitride down to polysilicon.

    (PE II, CF_4 gas, 200 W, 200 mtorr.)

35. Photoresist Remove

    Perform the standard photoresist remove procedure.

36. PSG Etching in HF

    Use 49 wt.% HF to etch sacrificial PSG layer (25 minutes).

    Rinse in DI water and spin dry.

    Check under microscope if channel and sensor chamber are etched through.

    (If not, etch another 10 minutes.)

    DI water rinse no less than 60 minutes.

    Spin dry in a vacuum spin dryer and bake wafer in annealing furnace.

    (600 °C for 30 minutes.)

37. LPCVD LTO Deposition

Use LPCVD to deposit 1.0 μm LTO to seal the etching holes.

(Standard oxynitride recipe, deposition time 60 minutes.)

Check sealing.

(If pressure sensor chambers are not sealed, deposit another 20 minute.)

38. Photolithography with Mask #8

Perform standard photolithography procedure with mask #8.

(KTI 100CS, speed 2.0 krpm, photoresist 3.5 μm.)

(Protect back side of wafer with blue tape before developing photoresist; strip blue tape before hard bake.)

39. LTO Pattern

Do descum first and then protect back side of wafer with blue tape.

Use buffered HF to etch LTO.

(10% over etch to ensure LTO is etching away anywhere on the wafer.)

40. Photoresist Remove

Clean with acetone, alcohol and DI water and spin dry.

Peel off the blue tape carefully.

Perform plasma ashing.

Protect the backside with blue tape.

Dip in diluted (5%) HF for 2 minutes (remove native oxide).

DI water rinse till water resistivity >12 MW and spin dry.

Peel off the blue tape.

41. Aluminum Evaporation

Evaporate 1.0 μm aluminum (E-beam or thermal evaporator).

42. Photolithography with Mask #9

Perform standard photolithograph procedure with mask #9.

(KTI 27CS, 3.5 krpm, 1.2 μm)

(Protect the backside of the wafer with blue tape before developing and peel it off before hard bake.)

43. Aluminum Etching

    Perform descum first and protect backside with blue tape.

    Etch aluminum with aluminum etchant (50 °C, 2 minutes).

    Peel off the blue tape and do plasma ashing to remove photoresist.

44. Aluminum Sintering

    Sinter aluminum in metal annealing furnace.

    (450 °C for 45 minutes, N_2 ambient.)

45. Wafer Dicing

    Spin on photoresist (KTI 100CS, 2.0 krpm, 4 μm) and do hard bake 30 minutes at 120 °C.

    Dice wafer (1×1 cm^2, cut depth 350 μm (150 μm left)).

    After stripping blue tape, do plasma ashing to finally clean wafer.

A.4 Masks For the Microflow System

A.4.1 Masks for the First Generation Microflow System

A.4.2 Masks for the Second Generation Microflow System

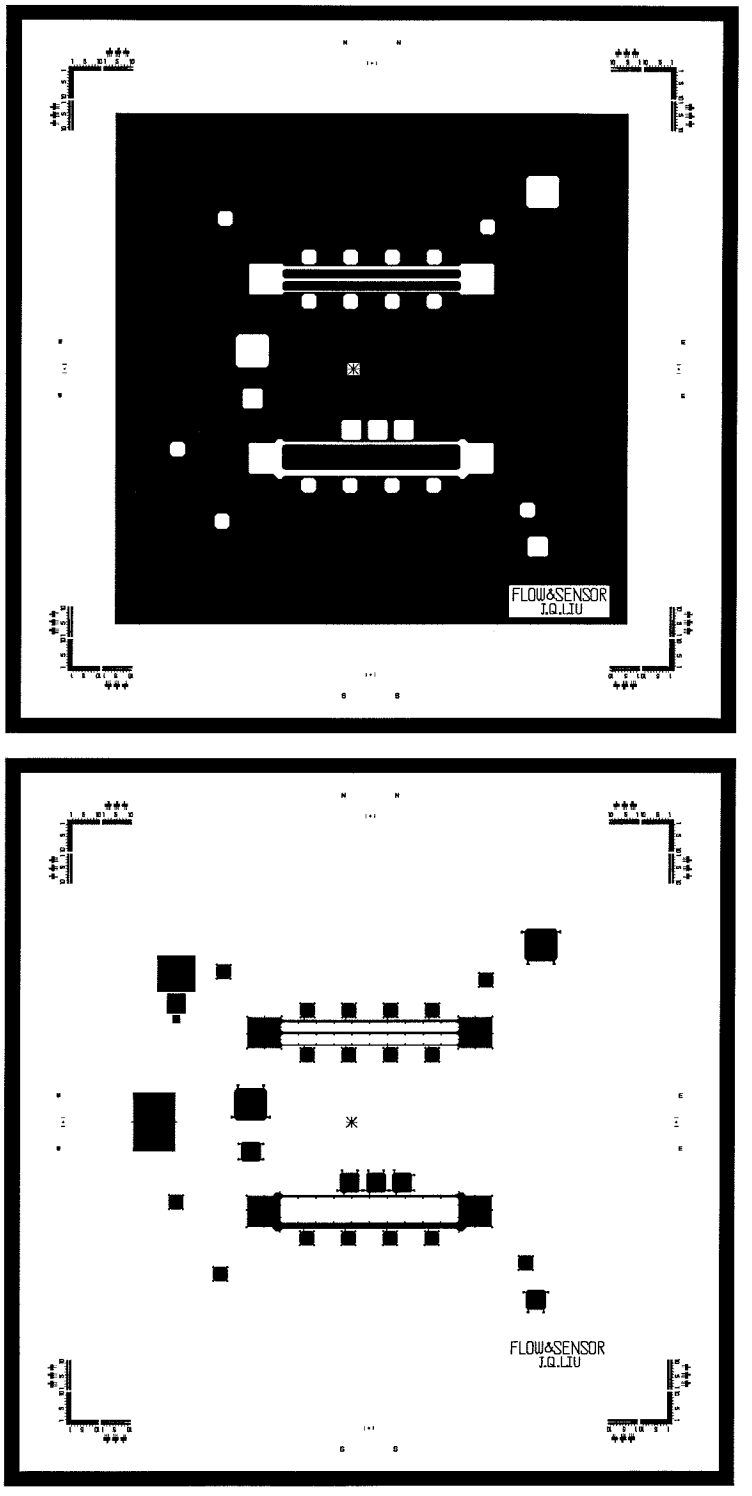

Figure A.1: Mask No. 1 and No. 2 for microflow system fabrication.

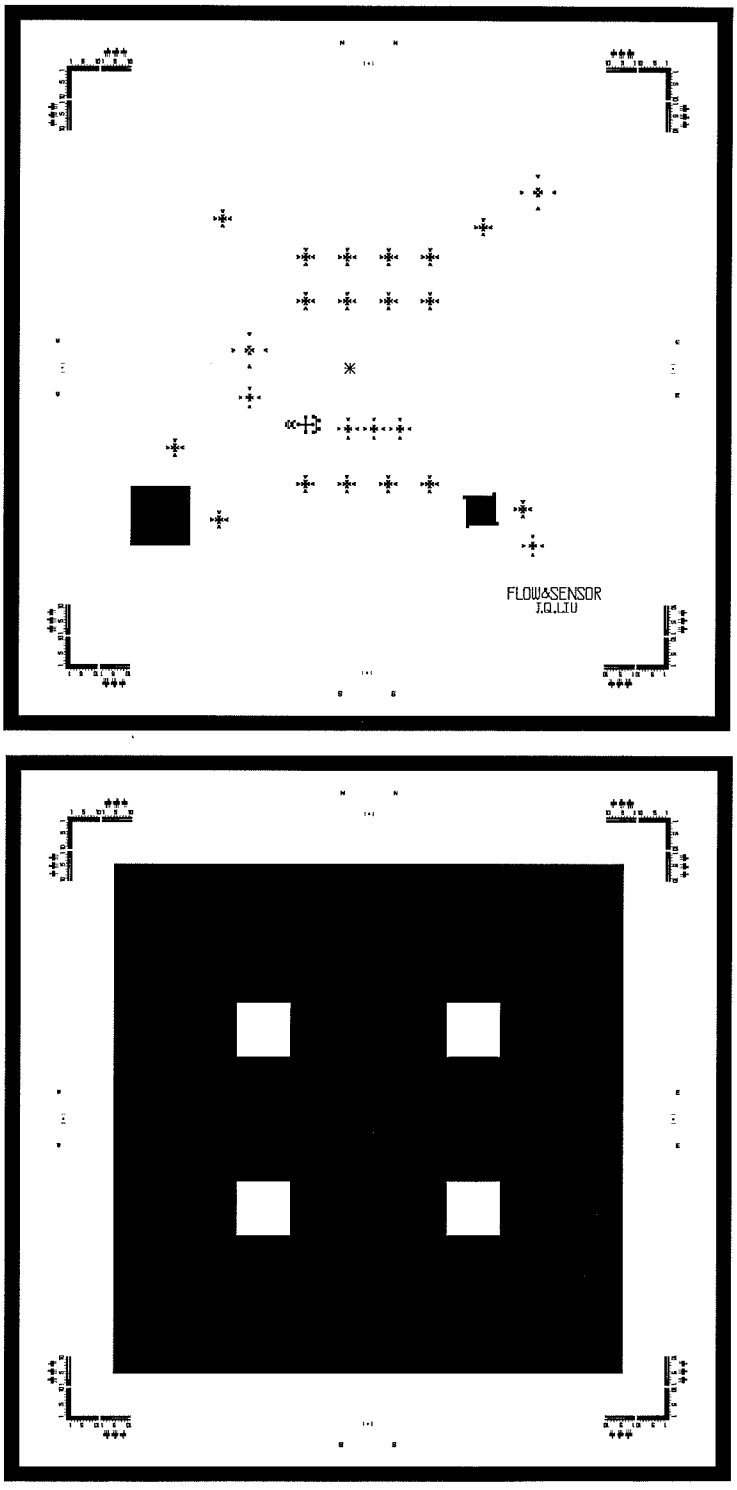

Figure A.2: Mask No. 3 and No. 4 for microflow system fabrication.

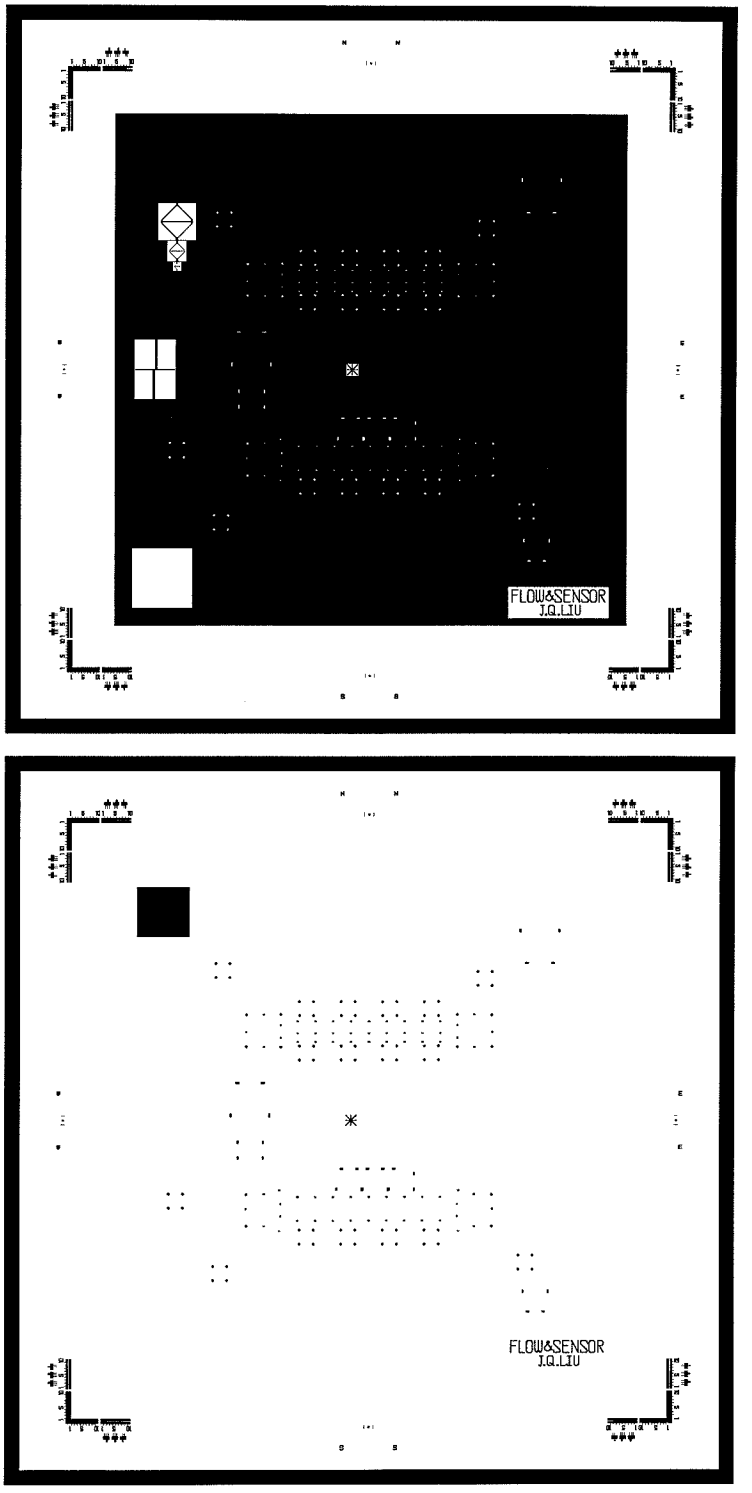

Figure A.3: Mask No. 5 and No. 6 for microflow system fabrication.

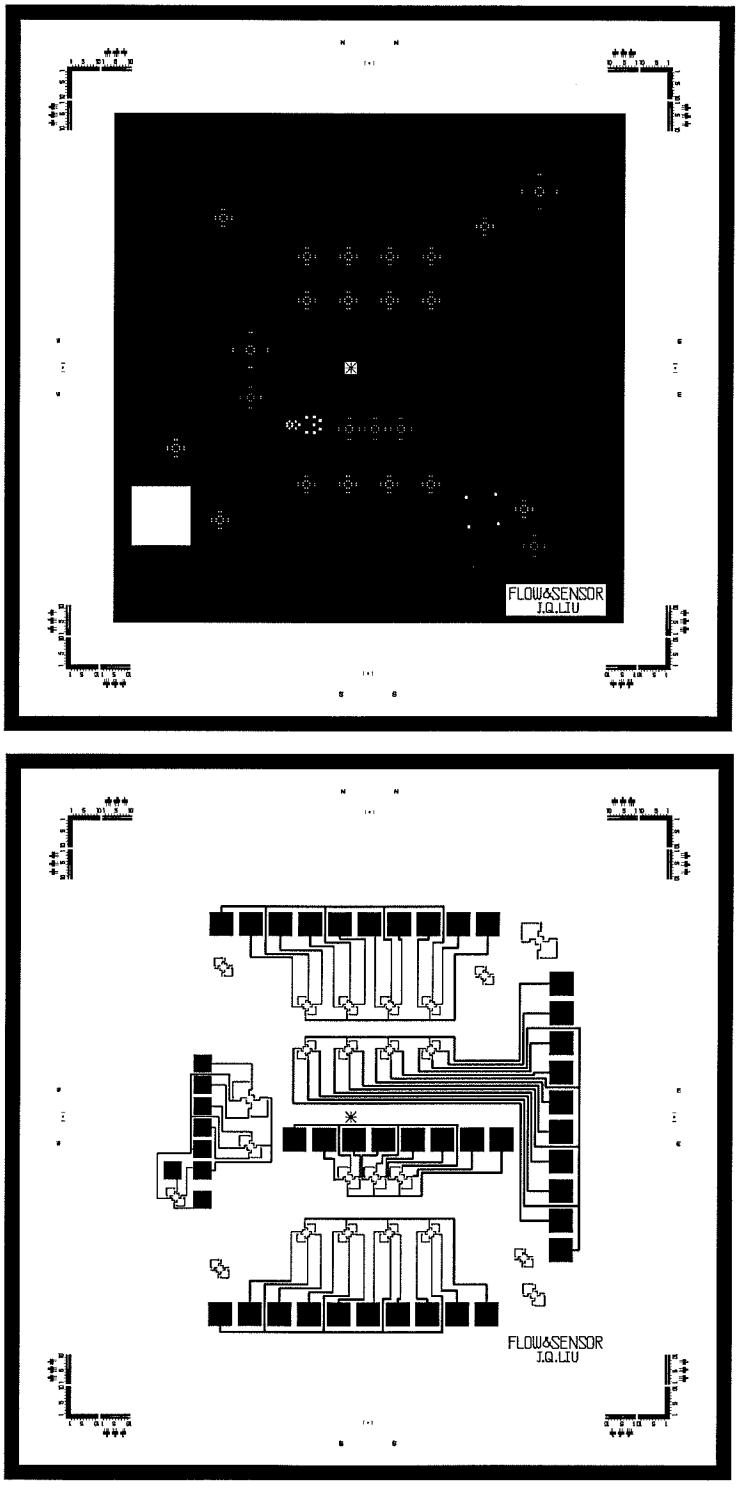

Figure A.4: Mask No. 7 and No. 8 for microflow system fabrication.

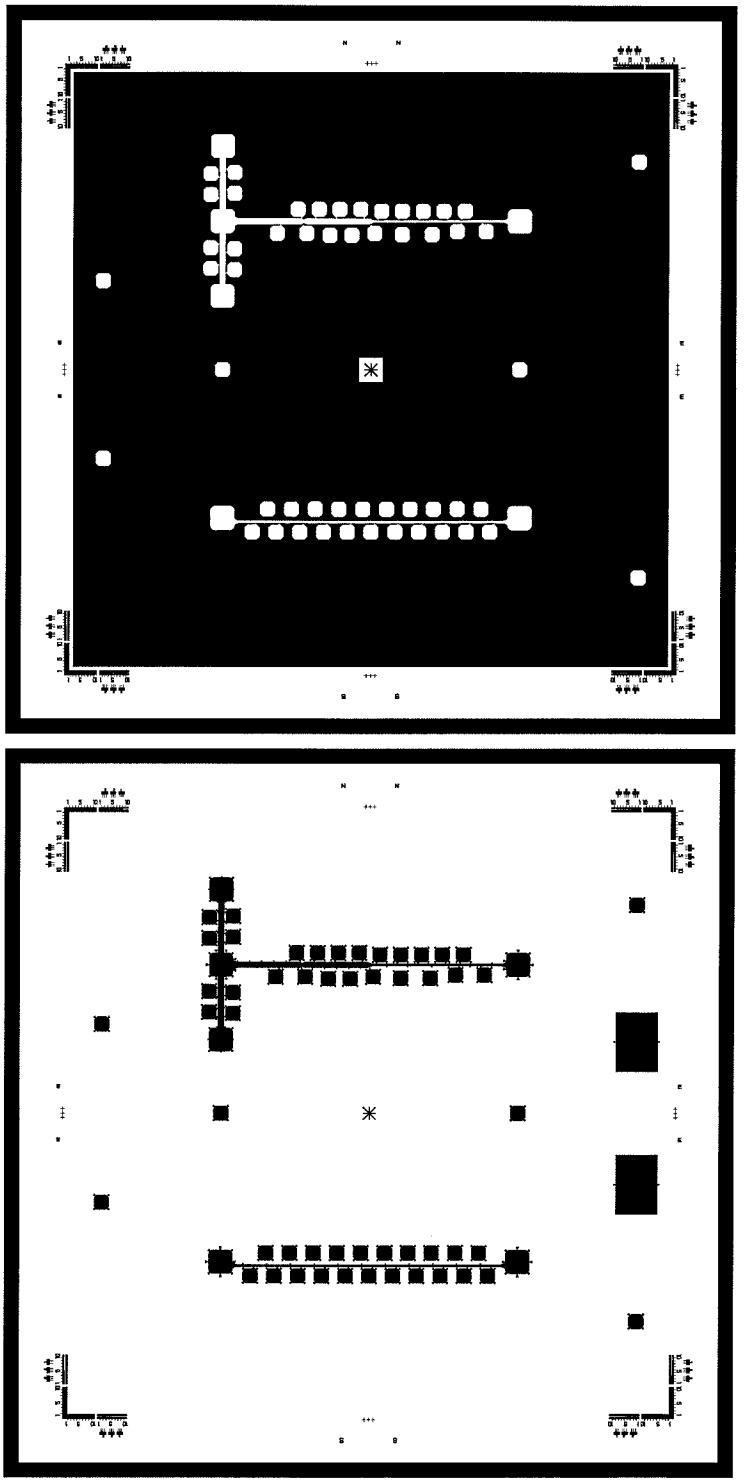

Figure A.5: Mask No. 1 and No. 2 for microflow system fabrication.

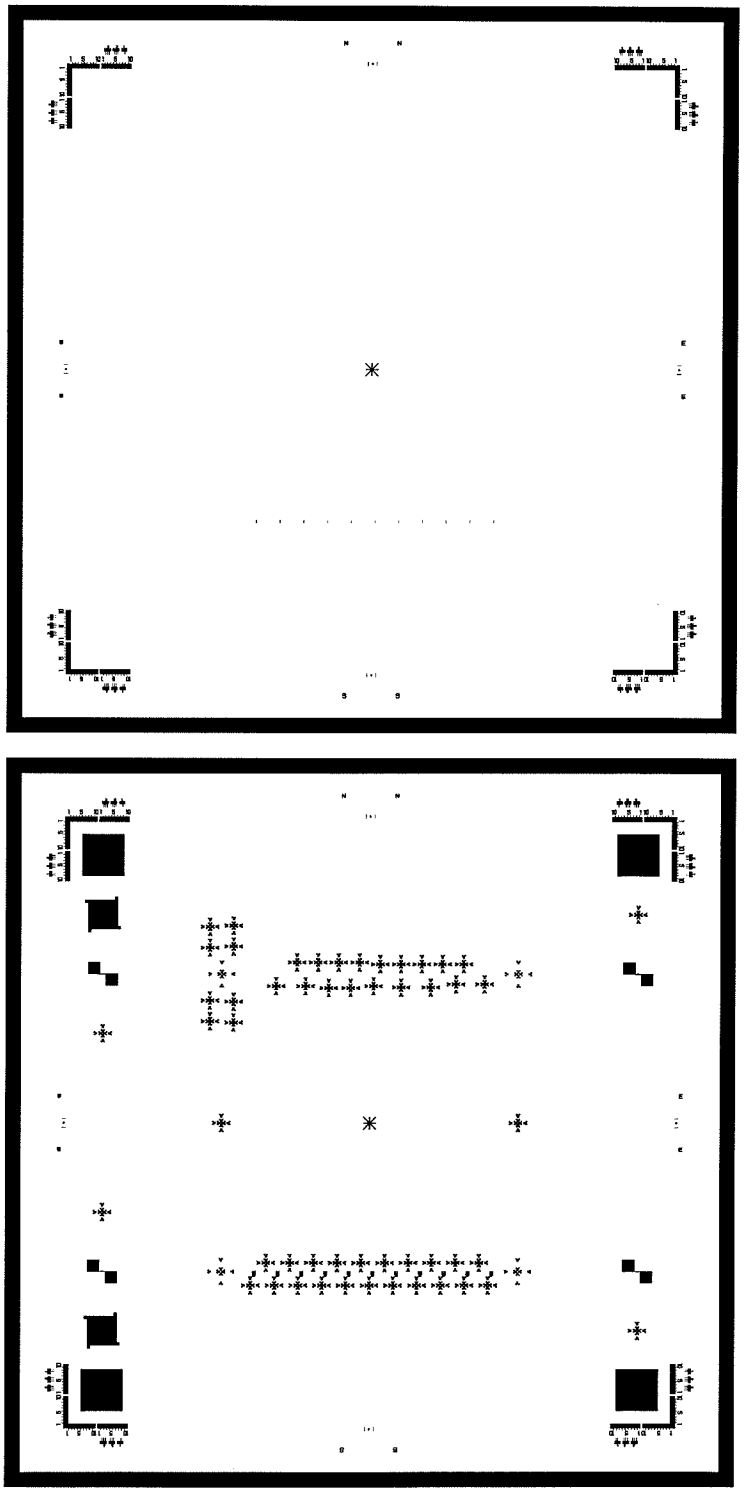

Figure A.6: Mask No. 3 and No. 4 for microflow system fabrication.

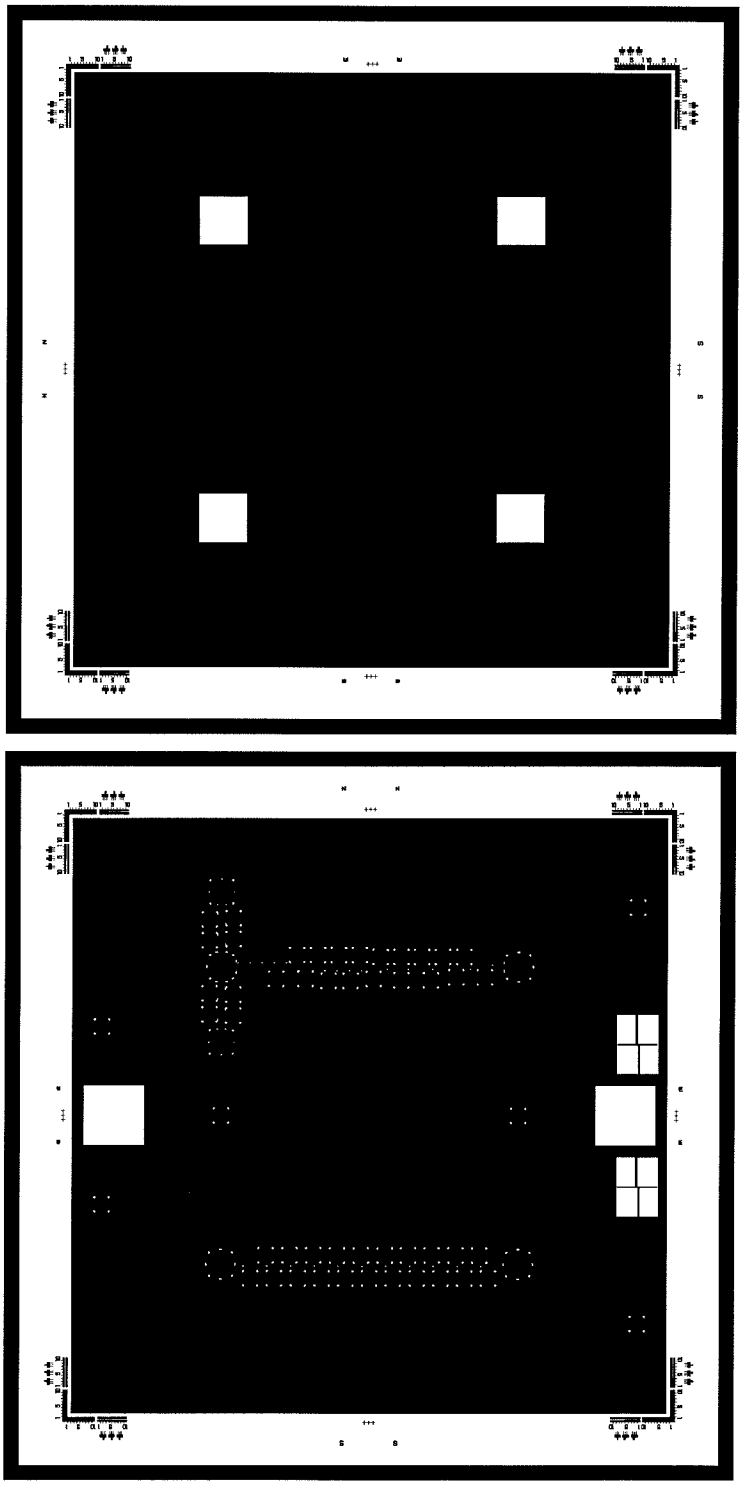

Figure A.7: Mask No. 5 and No. 6 for microflow system fabrication.

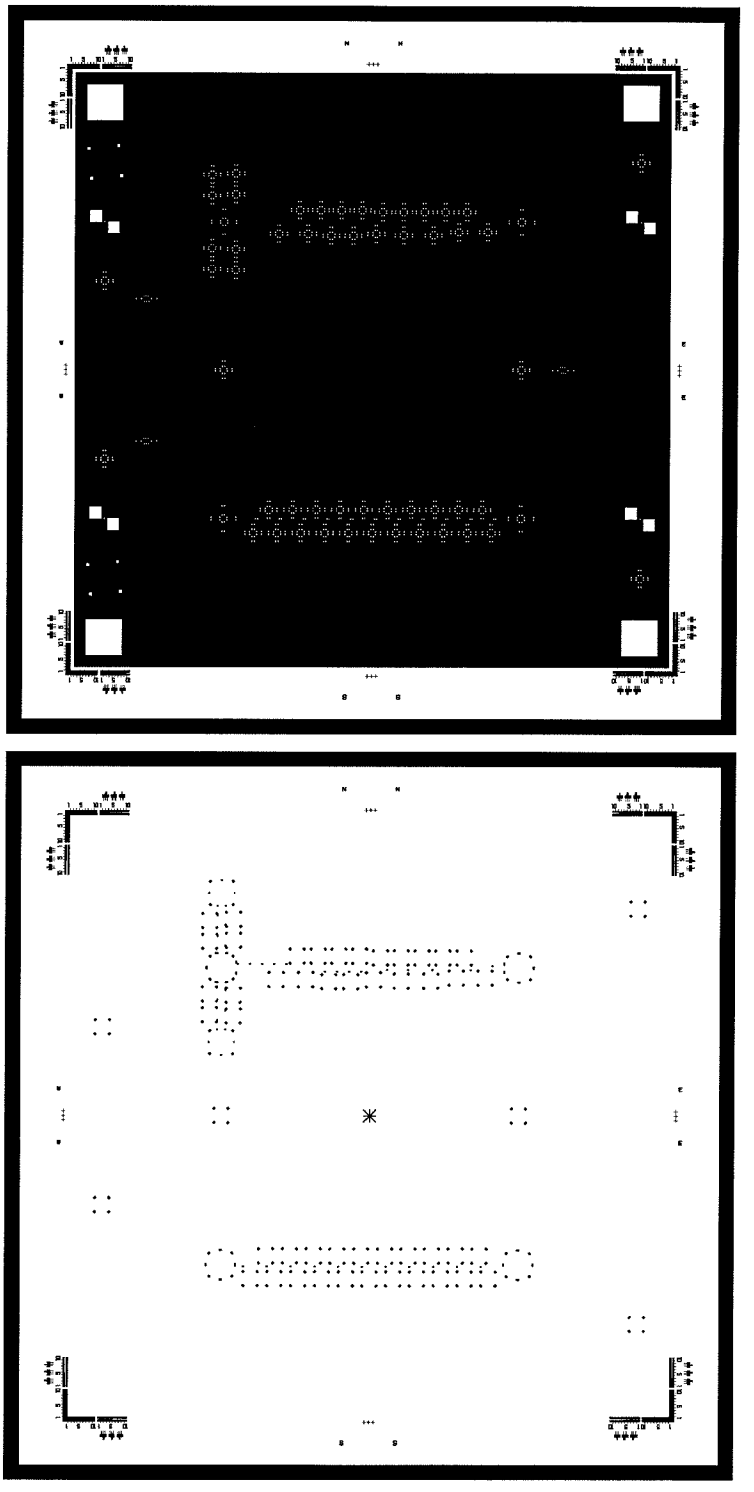

Figure A.8: Mask No. 7 and No. 8 for microflow system fabrication.

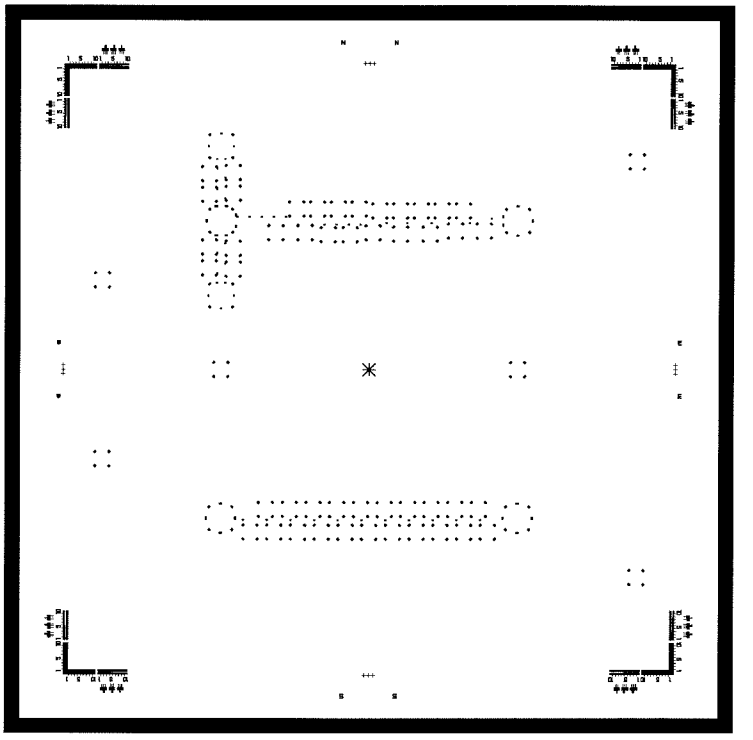

Figure A.9: Mask No. 9 for microflow system fabrication.

Appendix B

Computer Code

B.1 FORTRAN Program For PSG Etch Modeling

```
C
C     Nonlinear Fit Program (for 1st & 2nd order model data)
C
      PROGRAM MIAN
      IMPLICIT REAL*8 (a-h,o-z,A-H,O-Z)
      CHARACTER CONTROL,FILENAME*20
      DIMENSION X(100),Y(100),SIG(100),A(3),COVAR(10,10)
      DIMENSION LISTA(3),ALPHA(10,10)
C
      EXTERNAL FUNCS
C
      COMMON Ca,A0
C
      WRITE(6,*) ' Give me Ca, and data file name, '
      READ(5,*)Ca,FILENAME
      Wsio2=60.08
      Rsio2=2.1
```

```
      A0=Wsio2/Rsio2/6.0
      NDATA=60
      LISTA(1) = 1
      LISTA(2) = 2
      LISTA(3) = 3
      MA=3
      NCA=10
      MFIT = 3
      ALAMDA = -1.0
      OPEN(7,FILE= FILENAME)
      READ(7, *) (Y(I),X(I),I=1,NDATA)
C     WRITE(6,99) (X(I),Y(I),I=1,NDATA)
      DO I=1,NDATA
        Y(I)=Y(I)*60.0
        X(I)=X(I)/1.e4
      END DO
      write(6,*) 'Start iteration'
C initial guess for k1, k2 and D:
      A(1)=6.53e-4
      A(2)=-0.0216
      A(3)=5.57e-6
      DO I=1, NDATA
        SIG(I)=60.0
      END DO

10    CALL MRQMIN(X,Y,SIG,NDATA,A,MA,LISTA,MFIT,COVAR,ALPHA,NCA,
     * CHISQ,FUNCS,ALAMDA)
      WRITE(*,*) 'Alamde= ',ALAMDA, 'CHISQ= ',CHISQ
C
      WRITE(*,*) 'Iteration again ?'
```

```
      READ(*,11) CONTROL
11    FORMAT(A10)
      IF( CONTROL.EQ.'Y'.OR.CONTROL.EQ.'y') GO TO 10
      ALAMDA = 0.0
      CALL MRQMIN(X,Y,SIG,NDATA,A,MA,LISTA,MFIT,COVAR,ALPHA,NCA,
     * CHISQ,FUNCS,ALAMDA)
      WRITE(6,*) 'CHISQ = ',CHISQ
      WRITE(6,*) 'k1= ',A(1),'k2= ',A(2),'D= ',A(3)
      CLOSE(7)
99    FORMAT(F12.4,F12.4)
      STOP
      END


      SUBROUTINE FUNCS(z,A,T,DTDA,NA)
C
      IMPLICIT REAL*8(A-H,O-Z,a-h,o-z)
      INTEGER NA
      DIMENSION A(NA),DTDA(NA)
      COMMON Ca,A0
C
C      WRITE(6,*) 'Ca= ',Ca, 'A0= ',A0
      R0=DSQRT((A(3)**2+2*A(3)*A(1)*z+4*Ca*A(3)*A(2)*z+A(1)**2*z**2)/
     - A(3)**2)
      RL1=DLOG(A(1)+2*Ca*A(2)+A(1)**2*z/A(3)+A(1)*R0)
      RL2=DLOG(2*(A(1)+Ca*A(2)))
C
      T=A(3)*A(2)*(-(A(1)+2*Ca*A(2))/(8*Ca*A(1)**2*A(2)*(A(1)+Ca*
     - A(2)))+z/(4*Ca*A(3)*A(1)*A(2)+4*Ca**2*A(3)*A(2)**2)+
     - (A(1)+2*Ca*A(2))*z**2/(8*Ca*A(3)**2*A(2)*(A(1)+Ca*A(2)))+
```

```
     - (A(3)*A(1)+2*Ca*A(3)*A(2)+A(1)**2*z)*R0/
     - (8*Ca*A(3)*A(1)**2*A(2)*(A(1)+Ca*A(2)))+RL2/(2*A(1)**3)-
     - RL1/(2*A(1)**3))/A0
      WRITE(6,*) T/60.0, 1.e4*z
C
      DTDA(1)=(-2*A(3)*A(1)**2-9*Ca*A(3)*A(1)*A(2)-6*Ca**2*
     - A(3)*A(2)**2+Ca*A(1)**2*A(2)*z)*R0/(8*A0*Ca*A(1)**3*(A(1)+
     - Ca*A(2))**2)+(2*A(3)**2*A(1)**3+9*Ca*A(3)**2*A(1)**2*A(2)+
     - 6*Ca**2*A(3)**2*A(1)*A(2)**2-2*A(3)*A(1)**4*z-Ca*A(1)**4*
     - A(2)*z**2-12*Ca*A(3)**2*A(1)**2*A(2)*RL2-24*Ca**2*A(3)**2*
     - A(1)*A(2)**2*RL2-12*Ca**3*A(3)**2*A(2)**3*RL2+12*Ca*A(3)**2*
     - A(1)**2*A(2)*RL1+24*Ca**2*A(3)**2*A(1)*A(2)**2*RL1+12*Ca**3*
     - A(3)**2*A(2)**3*RL1)/(8*A0*Ca*A(3)*A(1)**4*(A(1)+Ca*A(2))**2)
C
      DTDA(2)=(3*A(3)*A(1)+2*Ca*A(3)*A(2)-A(1)**2*z)*R0/
     - (8*A0*A(1)**2*(A(1)+Ca*A(2))**2)+(-3*A(3)**2*
     - A(1)**2-2*Ca*A(3)**2*A(1)*A(2)-2*A(3)*A(1)**3*z+A(1)**4*z**2+
     - 4*A(3)**2*A(1)**2*RL2+8*Ca*A(3)**2*A(1)*A(2)*RL2+4*Ca**2*
     - A(3)**2*A(2)**2*RL2-4*A(3)**2*A(1)**2*RL1-8*Ca*A(3)**2*
     - A(1)*A(2)*RL1-4*Ca**2*A(3)**2*A(2)**2*RL1)/(8*A0*A(3)*
     - A(1)**3*(A(1)+Ca*A(2))**2)
C
      DTDA(3)=(A(3)*A(1)+2*Ca*A(3)*A(2)-A(1)**2*z)*R0/
     - (8*A0*Ca*A(3)*A(1)**2*(A(1)+Ca*A(2)))+(-(A(3)**2*A(1)**2)-
     - 2*Ca*A(3)**2*A(1)*A(2)-A(1)**4*z**2-2*Ca*A(1)**3*A(2)*z**2+
     - 4*Ca*A(3)**2*A(1)*A(2)*RL2+4*Ca**2*A(3)**2*A(2)**2*RL2-
     - 4*Ca*A(3)**2*A(1)*A(2)*RL1-4*Ca**2*A(3)**2*A(2)**2*RL1)/
     - (8*A0*Ca*A(3)**2*A(1)**3*(A(1)+Ca*A(2)))
C
      RETURN
```

```
      END


C
C  Program MRQMIN, MRQCOF, GAUSSJ, COVSRT are from "Numerical Recipe"
C
      SUBROUTINE MRQMIN(X,Y,SIG,NDATA,A,MA,LISTA,MFIT,
     *    COVAR,ALPHA,NCA,CHISQ,FUNCS,ALAMDA)

      SUBROUTINE MRQCOF(X,Y,SIG,NDATA,A,MA,LISTA,MFIT,ALPHA,BETA,NALP,
     *CHISQ,FUNCS)

      SUBROUTINE GAUSSJ(A,N,NP,B,M,MP)

      SUBROUTINE COVSRT(COVAR,NCVM,MA,LISTA,MFIT)
```

B.2 C Code for HP Data Acquisition System Control

```
#include <stdlib.h>
#include <string.h>
#include <stdio.h>
#include <dos.h>
#include <math.h>
#include <time.h>
#include <c:\qcwin\include\conio.h>
#include "c:\hpib\cfunc.h"
#include "c:\hpib\chpib.h"
```

```
int Initialize(void);
int Setup(void);
int DoSRQ(void);
int GetData(void);
int CheckSRQ(void);
int Cleanup(void);
void SendCommand(char *);
int ErrorHandle(int, char *);

#define Points_of_EachScan 1
#define Total_Points     256
#define First_Channel 500
#define Last_Channel 512
#define Total_Sensors     Last_Channel-First_Channel+1

long    isc;
long    HP3852A, Keithley230;
char    Command[200], FileName[30];
int     length, error;
float   readings[Total_Sensors], sensor[Total_Sensors];
float Pressure;

main()

{
char c, loop_control='y';
time_t TimeStart, TimeEnd;
int control, error, DT, no, Num_of_Measurements, counter=0;
FILE *fp, *fopen();
    printf(" Uniform microchannel/13 sensors flow measurements!\n");
```

```
printf("\n Initializing ... !");
error=Initialize();
error=Setup();
printf("\n Name for data file : ");
scanf("%s",FileName);
printf("\n Enter file description : ( type in '~' to finish )\n");
if ( (fp = fopen(FileName, "a")) != NULL )
{
fputs("\n# File description ...  \n", fp);
while ( (c=getche()) != '~')
{
fputc(c,fp);
if( c == '\r')
{
printf("\n");
fputc("\n",fp);
}
}
fputs("\n# End of description.\n", fp);
fclose (fp);
}
while ( loop_control == 'y' || loop_control =='Y') {
printf("\n\n Setting PRESSURE : ");
scanf("%f",&Pressure);
printf("\n HOW MANY measurements for this pressure
setting?  ");
scanf("%d",&Num_of_Measurements);
time(&TimeStart);
time(&TimeEnd);
printf("\n Waiting for flow stabilized :
```

```
seconds\b\b\b\b\b\b\b\b");
while ( (DT=difftime(TimeEnd, TimeStart)) <= 60.0 )
{
printf("\b\b\b\b%4d",DT);
          time(&TimeEnd);
        }
    printf("\n");
no = 0;
while( no++ < Num_of_Measurements )
{
printf(" at the %dth measurement :",no);
if(CheckSRQ() == 1)
error=DoSRQ();
error=GetData();
}
loop_control='n';
printf("\n Do you have more to measure ?
(type in 'y' to measure more)  ");
loop_control = getche();
}
Cleanup();
return(0);
}

int Initialize()
{
isc = 7L;
HP3852A = isc*100L + 9L;
Keithley230 = isc*100L+13L;
ErrorHandle(IORESET(isc), "IORESET");
```

```
ErrorHandle(IOTIMEOUT(isc, 10.0), "IOTIMEOUT");
ErrorHandle(IOCLEAR(HP3852A), "IOCLEAR #2");
ErrorHandle(IOCLEAR(Keithley230),"IOCLEAR #3");
ErrorHandle(IOFASTOUT(isc, 1), "IOFASTOUT");
ErrorHandle(IOEOL(isc,"", 0), "IOEOL");
return(0);
}

int Setup()
{
/* Keithley230 Setup */
ErrorHandle(IOOUTPUTS(Keithley230,"D1I1X",strlen("D1I1X")),
"IOOUTPUTS");
ErrorHandle(IOOUTPUTS(Keithley230,"R3M1X",strlen("R3M1X")),
"IOOUTPUTS");
ErrorHandle(IOOUTPUTS(Keithley230,"D0V5X",strlen("D0V5X")),
"IOOUTPUTS");
ErrorHandle(IOOUTPUTS(Keithley230,"P1F1X",strlen("P1F1X")),
"IOOUTPUTS");
/* HP3852A Setup  */
ErrorHandle(IODMA(isc, 40, 3), "IODMA #1");
SendCommand("RST 600");
SendCommand("USE 600");
SendCommand("RANGE 10");
SendCommand("RESOL 16");
SendCommand("NRDGS 5");
SendCommand("CONF DCV");
SendCommand("RANGE 0.6");
ErrorHandle(IODMA(isc, 0, 3), "IODMA #2");
return(0);
```

```
}


int DoSRQ()
{
int     response;

ErrorHandle(IOSTATUS(isc, 1, &response), "IOSTATUS #2");

if(response == 1)
{
printf("SRQ locked high\n");
Cleanup();
exit(1);
}
return(0);
}

int GetData()
{
int     i,j,control, StartChannel;
char    filename[40],channel[5],points[5],command[200];
float average, standard_deviation, pressure;

time_t TimeStart, TimeEnd;

FILE *fp, *fopen();

    printf("        th cycles\b\b\b\b\b\b\b\b\b");
strcpy(command,"MEAS DCV,");
```

```
itoa(First_Channel,channel,10);
strcat(command,channel);
strcat(command,"-");
itoa(Last_Channel,channel,10);
strcat(command,channel);
strcat(command,", NSCAN ");
itoa(Points_of_EachScan,points,10);
strcat(command,points);
length = Total_Sensors;
    for (j=0; j<Total_Sensors; j++)
     sensor[j] = 0.0;
    time(&TimeStart);
for (i=0; i<Total_Points; i++)
  {
    printf("\b\b\b\b\b%5d",i+1);
    SendCommand(command);
    IOENTERA(HP3852A, readings, &length);
    for (j=0; j<Total_Sensors; j++)
      sensor[j] += readings[j];
  }
time(&TimeEnd);
printf(". Total takes : %6.1f seconds\n",difftime(TimeEnd,
TimeStart));
  for (j=0; j<Total_Sensors; j++)
   sensor[j]=sensor[j]/Total_Points;
  fp = fopen(FileName, "a");
  fprintf(fp,"%lf",Pressure);
  for( j = 0; j < Total_Sensors; j ++ )
    fprintf(fp,"  %lf", sensor[j]);
  fprintf(fp,"\n");
```

```
  fclose(fp);

return(0);
}

int Cleanup()
{
ErrorHandle(IOCLEAR(HP3852A), "IOCLEAR #4");
SendCommand("RST");
return(0);
}

int CheckSRQ()
{
int     response;

ErrorHandle(IOSTATUS(isc, 1, &response), "IOSTATUS #1");
return(response);
}

int ErrorHandle(int error, char *routine)
{
if(error != NOERR)
{
ErrorHandle(IOABORT(isc), "IOABORT");
Cleanup();
printf("\nHP-IB error in call to [%s], No. %d, %s\n",
                        routine, error, errstr(error));
exit(1);
}
```

```
return(0);
}

void SendCommand(char *command)
{
ErrorHandle(IOOUTPUTS(HP3852A, command, strlen(command)),
"IOOUTPUTS");
}
```